2010

# High Heat Flux Spray Cooling With Ammonia On Enhanced Surfaces

Huseyin Bostanci
*University of Central Florida*

## STARS Citation

Bostanci, Huseyin, "High Heat Flux Spray Cooling With Ammonia On Enhanced Surfaces" (2010). *Electronic Theses and Dissertations, 2004-2019*. 4266.
https://stars.library.ucf.edu/etd/4266

# HIGH HEAT FLUX SPRAY COOLING WITH AMMONIA ON ENHANCED SURFACES

by

HUSEYIN BOSTANCI
B.S. Istanbul Technical University, 1998
M.S. University of New Mexico, 2001

A dissertation submitted in partial fulfillment of the requirements
for the degree of Doctor of Philosophy
in the Department of Mechanical, Materials and Aerospace Engineering
in the College of Engineering and Computer Science
at the University of Central Florida
Orlando, Florida

Summer Term
2010

Major Professor: Louis C. Chow

# ABSTRACT

Many critical applications today, in electronics, optics and aerospace fields, among others, demand advanced thermal management solutions for the acquisition of high heat loads they generate in order to operate reliably and efficiently. Current competing technologies for this challenging task include several single and two phase cooling options. When these cooling schemes are compared based on the high heat flux removal (100-1000 W/cm$^2$) and isothermal operation (within several $^o$C across the cooled device) aspects, as well as system mass, volume and power consumption, spray cooling appears to be the best choice.

The current study focused on high heat flux spray cooling with ammonia on enhanced surfaces. Compared to some other commonly used coolants, ammonia possesses important advantages such as low saturation temperature, and high heat absorbing capability. Moreover, enhanced surfaces offer potential to greatly improve heat transfer performance. The main objectives of the study were to investigate the effect of surface enhancement on spray cooling performance, and contribute to the current understanding of spray cooling heat transfer mechanisms.

These objectives were pursued through a two stage experimental study. While the first stage investigated enhanced surfaces for the highest heat transfer coefficient at heat fluxes of up to 500 W/cm$^2$, the second stage investigated the optimized enhanced surfaces for critical heat flux (CHF). Surface modification techniques were utilized to obtain micro scale indentations and protrusions, and macro (mm) scale pyramidal, triangular, rectangular, and square pin fins. A third group, multi-scale structured surfaces, combined macro and micro scale structures.

Experimental results indicated that micro- and macrostructured surfaces can provide heat transfer coefficients of up to 534,000 and 426,000 $W/m^{2o}C$ at 500 $W/cm^2$, respectively. Multi-scale structured surfaces offered even a better performance, with heat transfer coefficients of up to 772,000 $W/m^{2o}C$ at 500 $W/cm^2$, corresponding to a 161% increase over the reference smooth surface. In CHF tests, the optimized multi-scale structured surface helped increase maximum heat flux limit by 18%, to 910 $W/cm^2$ at nominal liquid flow rate. During the additional CHF testing at higher flow rates, most heaters experienced failures before reaching CHF at heat fluxes above 950 $W/cm^2$. However, the effect of flow rate was still characterized, suggesting that enhanced surfaces can achieve CHF values of up to ≈1,100 $W/cm^2$ with ≈67% spray cooling efficiency.

The results also helped shed some light on the current understanding of the spray cooling heat transfer mechanisms. Data clearly proved that in addition to fairly well established mechanisms of forced convection in the single phase regime, and free surface evaporation and boiling through secondary nucleation in the two phase regime, enhanced surfaces can substantially improve boiling through surface nucleation, which can also be supported by the concept of three phase contact lines, the regions where solid, liquid and vapor phases meet. Furthermore, enhanced surfaces are capable of retaining more liquid compared to a smooth surface, and efficiently spread the liquid film via capillary force within the structures. This unique advantage delays the occurrence of dry patches at high heat fluxes, and leads to higher CHF.

# ACKNOWLEDGMENTS

I must express my sincere appreciation to my advisor Dr. Louis Chow for his inspiration, encouragement, and outstanding mentorship throughout the graduate program. He always made time for many long meetings and discussions. I have been very fortunate for finding the opportunity to do research under his guidance. I would like to thank Dr. Ruey-Hung Chen, Dr. Jay Kapat, and Dr. Kalpathy Sundaram for serving as my committee members and for their valuable comments.

I am grateful to Dr. Dan Rini of RINI Technologies. Besides making the experimental facility available, his continued interest and suggestions in this work were invaluable.

Several former and current graduate students shared their expertise, and contributed to the fabrication and characterization of test pieces. I thank Arun Vijayakumar, Weixing Xu and Virendra Signh.

I reserve very special thanks to my dear wife, Ozgul, for her support, understanding and patience that made this work possible, and my cute little son, Ediz, for giving me additional motivation and sense of urgency to complete. I thank to my parents and in-laws for their moral support.

Finally, I acknowledge Air Force Research Laboratory (AFRL) Propulsion Directorate and Universal Technology Corporation for their financial support through a joint project of North Carolina A&T State University and University of Central Florida, led by Dr. John P. Kizito.

# TABLE OF CONTENTS

# LIST OF FIGURES

# LIST OF TABLES

# LIST OF ACRONYMS/ABBREVIATIONS

| | |
|---|---|
| $A$ | area, cm$^2$ |
| CHF | Critical Heat Flux, W/cm$^2$ |
| $c_p$ | liquid specific heat, J/kg$^o$C |
| $EF_A$ | area enhancement factor |
| $EF_h$ | performance enhancement factor |
| $EF_{CHF}$ | CHF enhancement factor |
| $h$ | heat transfer coefficient, W/m$^{2o}$C |
| $h_{fg}$ | latent heat of vaporization, kJ/kg |
| $I$ | current, A |
| $k$ | heater wall thermal conductivity, W/m$^o$C |
| $k_l$ | liquid thermal conductivity, W/m$^o$C |
| $P_{sat}$ | saturation pressure, kPa |
| $q''$ | heat flux, W/cm$^2$ |
| $T_{bottom}$ | bottom surface temperature, $^o$C |
| $T_l$ | liquid temperature, $^o$C |
| $T_{res}$ | resistor temperature, $^o$C |
| $T_{sat}$ | saturation temperature, $^o$C |
| $T_{surf}$ | surface temperature, $^o$C |
| $TC_{avg}$ | average thermocouple reading, $^o$C |
| $r_{c,max}$ | maximum cavity mouth radius, µm |

| | |
|---|---|
| $r_{c,min}$ | minimum cavity mouth radius, μm |
| $R_a$ | average surface roughness, μm |
| $V$ | voltage, V |
| $\dot{V}$ | liquid flow rate of spray nozzle, $mL/cm^2$-s |
| $x$ | TC to spray surface distance in heater wall, m |
| $\mu_l$ | liquid dynamic viscosity, kg/m.s |
| $\rho_l$ | liquid density, $kg/m^3$ |
| $\rho_v$ | vapor density, $kg/m^3$ |
| $\delta t$ | thermal boundary layer thickness, m |
| $\eta$ | spray cooling efficiency |
| $\sigma$ | surface tension, N/m |

# CHAPTER 1: INTRODUCTION

The present work is an experimentally oriented spray cooling study that investigated the means of performance improvement through the use of various surface modification techniques on the heat transfer surfaces. This chapter starts with the motivation of the research, states the objectives, and describes the technical approach to achieve these objectives.

## 1.1 Motivation

Many of today's electronics, optics and aerospace applications demand acquisition of high heat loads they generate for efficient and reliable operation. Devices and systems such as computer chips, IGBT's, solid state lasers, directed energy weapons, phased-array radar sensors, signal processing systems, hypersonic flight structures and high Mach engines, therefore, require implementation of a thermal management system that is capable of removing high heat fluxes in the range of 100 to 1000 W/cm$^2$. Moreover, maintaining an isothermal operation within a few $^{o}$C temperature range is critical to ensure proper functionality of some of the mentioned systems.

Current competing technologies for this challenging task include several single and two phase cooling options. Microchannel cooling, liquid jet impingement cooling and spray cooling are the three leading candidates that can tackle the task. When these three cooling schemes are compared based on high heat flux removal capability and isothermality as well as system mass, volume and power consumption, however, spray cooling appears to be the best choice. Spray cooling has been demonstrated to remove high heat fluxes, over 1000 W/cm$^2$ using water, and provide uniform device temperatures at lower flow rates and pressure drops compared to other two cooling options. With these advantages, spray cooling enables design of compact, lightweight and efficient thermal management systems.

In some cases, low device temperature might be another requirement in the design and selection of cooling systems. Laser systems for instance, desire device temperatures ≤60 °C for highly efficient operation. Considering thermal resistance imposed by the system packaging, this requirement translates into the usage of coolant temperatures at ≤10 °C. In other circumstances, low device temperatures might be preferred to protect the assets against thermal image detection. Such needs can be satisfied by using a proper fluid that has low saturation point at reasonable pressure range, and still possesses high latent heat of vaporization to handle high heat transfer rates. Ammonia, the working fluid in the present study, then becomes a very attractive choice, with -33 °C saturation temperature at atmospheric pressure, and the second highest latent heat of vaporization among commonly used refrigerants.

Due to its appealing characteristics, spray cooling has been receiving an increasing attention over the last decade. Many spray cooling related research investigated nozzle types and spray parameters. Other studies explored heat transfer mechanisms and effects of non-condensable gas, spray inclination and gravity. Some recent efforts included mechanistic modeling of spray cooling. Studies focusing on spray cooling of enhanced surfaces are yet, fairly limited. Further experimental work in this area would be very helpful in order to expand heat transfer performance and application areas of spray cooling technology. The scope of this research was therefore defined as investigation of spray cooling with ammonia on enhanced surfaces. The outcome of the research would be a timely contribution to the literature with broad practical applications.

## 1.2 Objectives

Based on the defined scope, primary objective of the current research was to investigate the effect of surface enhancement on spray cooling performance. Experimental efforts addressed spray cooling performance in terms of heat transfer coefficient and critical heat flux (CHF).

Secondary goal of this study was to contribute to the current understanding of spray cooling heat transfer mechanisms. Experimental findings were examined and discussed in order to shed some light on the very complex heat transfer mechanisms.

## 1.3 Technical Approach

In the current research, objectives were attempted to meet through a two stage technical approach. The first stage determined the optimum surfaces that provided highest heat transfer coefficient at heat fluxes up to 500 W/cm$^2$ based on selected constant flow rates. Thus, the results addressed enhanced surfaces that were optimized for the majority of high heat flux applications at a flow rate level allowing efficient operation of the cooling system. In order to conduct the experimental study, various surface modification techniques were employed to fabricate test surfaces with resulting morphological changes that spanned the range of scales from micro (~1 μm) to macro (~1 mm). By combining micro and macro scale structures, a third group of surfaces, multi-scale structured surfaces, were also fabricated in an attempt to utilize the enhancement mechanisms of both micro- and macrostructured surfaces. All these test surfaces were compared to the reference smooth surface to obtain a quantitative measure of enhancement.

The second stage started with the short list of optimum enhanced surfaces, and determined the CHF limits on these surfaces at various flow rate levels. Thus, second stage evaluated the ultimate heat flux removal limits that enhanced surfaces can safely offer depending on cooling system efficiency. An overall step-by-step technical approach to the present study can be summarized as follows:

- Investigate optimum surfaces that provide highest heat transfer coefficient at heat fluxes up to 500 W/cm$^2$ at constant flow rates (1.6 mL/cm$^2$-s liquid, 13.8 mL/cm$^2$-s vapor).
  - Establish baseline performance with reference smooth surface.
  - Determine optimum microstructured surface.
    - Vary structure geometry (indentation, protrusion).
    - Vary structure size (fine, medium, coarse).
  - Explain heat transfer enhancement mechanism with microstructured surface.
  - Determine optimum macrostructured surface.
    - Vary structure geometry (pyramidal, triangular, rectangular and square pin fin).
    - Vary structure size (0.25 mm, 0.50 mm, 0.75 mm).
  - Explain heat transfer enhancement mechanism with macrostructured surface.
  - Determine optimum multi-scale structured surface.
    - Combine optimum micro- and macrostructured surfaces.
  - Explain heat transfer enhancement mechanism with multi-scale structured surface.
- Investigate CHF limits on optimum surfaces at various flow rates.
  - Establish baseline performance with reference smooth surface.

- Determine CHF limits on optimum micro-, macro- and multi-scale structured surfaces at nominal flow rates (1.6 mL/cm$^2$-s liquid, 13.8 mL/cm$^2$-s vapor).
- Explain CHF enhancement mechanism with optimum micro-, macro- and multi-scale structured surfaces.
- Determine CHF limits on optimum micro-, macro- and multi-scale structured surfaces at various (nominal/low, medium, high) flow rates.

Vary flow rates (1.6 to 2.1 mL/cm$^2$-s liquid, 13.8 to 17.7 mL/cm$^2$-s vapor).

# CHAPTER 2: LITERATURE REVIEW

This chapter starts with a brief overview of spray cooling, and then summarizes the relevant published spray cooling studies that experimentally explored enhanced surfaces with micro and macro scale structures.

## 2.1 Spray Cooling: An Overview

Spray cooling finds itself many different applications including the industrial, agricultural, electronics, optics, HVAC, and medical fields. This overview will consider spray cooling applications used for removing heat typically from a surface that is maintained at temperatures below the Leidenfrost point of the coolant.

Spray cooling process starts with forcing a liquid stream through a small orifice which leads shattering it into a dispersion of fine droplets. These droplets then impact a heated surface, form thin discs, and interact with each other giving rise to a thin liquid film (or evaporate in the case of a dilute spray). The sprayed liquid flows radially outwards in the liquid film on the surface, and absorbs large amounts of heat as it moves, with the help of several simultaneously occurring heat transfer mechanisms [1, 2].

Sprays can be generated using various atomization methods. The most widely used method is the pressure atomization, where high pressure liquid is given a swirling motion by the nozzle features, and then injected into a low pressure environment. Other common method is the gas-assisted atomization, where a liquid stream is introduced into a high velocity gas stream. The shear forces created by the gas stream atomize the liquid into fine droplets that are ejected from the nozzle orifice [1]. When these two atomization methods are compared, both have their advantages and disadvantages. Pressure atomizers have a simpler design but require a certain minimum pressure to achieve an acceptable spray. Gas-assisted atomizers come with a more complex design, but offer several advantages, such as finer droplet size, thinner liquid film, and lower vapor partial pressure above the liquid film due to the gas jet, eventually enhancing evaporation. Moreover, a number of other atomization techniques, such as ultrasonic and electrostatic, have been developed for some applications.

Spray cooling data are generally presented in the form of surface temperature (or, surface superheat, the difference between surface and saturation temperatures, if saturated liquid is used) vs. heat flux. The resulting spray cooling curve reflects three distinct heat transfer regimes. Figure 2-1 includes a typical spray cooling curve obtained using an air atomized water spray, and is helpful for the explanation of the three regimes as follows:

- I. Single phase forced convection region where heat transfer coefficient is low.
- II. Two phase boiling/evaporation region where heat transfer coefficient is much higher due to the activation of additional heat transfer mechanisms at higher superheats.
- III. Two phase-to-CHF transition region where heat transfer coefficient starts to decrease with the inception of heater dryout [1].

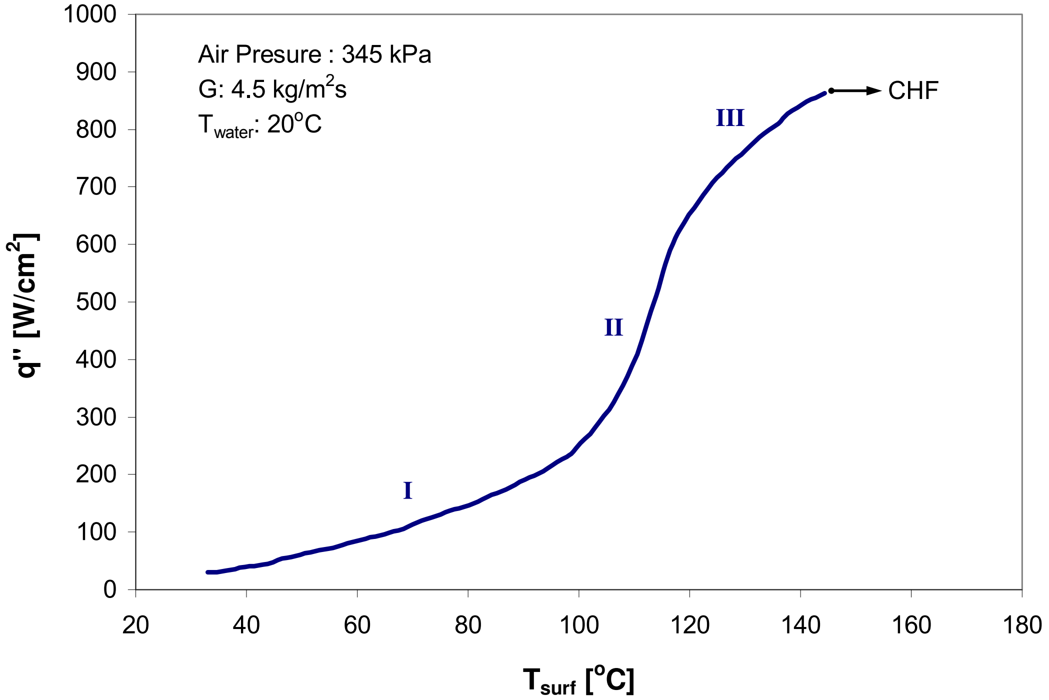

Figure 2-1: A Typical Spray Cooling Curve Illustrating the Three Heat Transfer Regimes (Adopted from [3])

Many studies were conducted to investigate the fundamentals of spray cooling process. Table 2-1 lists important parameters in four groups that are known to affect spray cooling performance. Usually a spray can be characterized by three independent parameters of droplet size, number flux and velocity. More practical aspects, such as, nozzle type, orifice size, liquid and/or vapor flow rates, and driving pressure all indirectly change these three droplet features. As can be expected, the thermophysical properties of the selected fluid are important in determining the overall cooling capability. The properties of the heater, or the cooled object in general, constitutes the other group of parameters. Of these, superheat, surface morphology and surface wettability, control or strongly influence some of the heat transfer mechanisms involved in spray cooling. While proper surface size helps for uniform cooling, surface orientation can change fluid drainage and bubble detachment patterns. All other parameters that are not tied to spray, fluid or heater can be collected under environmental properties.

Table 2-1: Important Parameters that Affect Spray Cooling Performance

| | |
|---|---|
| Spray properties | Droplet size<br>Droplet number flux<br>Droplet velocity |
| Fluid properties | Thermal conductivity of liquid<br>Surface tension of liquid<br>Specific heat of liquid<br>Latent heat of vaporization |
| Heater properties | Superheat<br>Surface morphology<br>Surface wettability<br>Surface size<br>Surface orientation<br>Thermal diffusivity of substrate |
| Environmental properties | Nozzle-to-surface distance<br>Spray angle<br>Subcooling<br>Foreign nuclei<br>Gravity<br>Ambient gas density<br>Ambient gas viscosity |

Due to the complex nature of the spray cooling process, there is currently no clear consensus on the heat transfer mechanisms. However, reviewing the major proposed mechanisms is still very helpful.

For the single phase regime, or low surface superheats, main heat transfer mechanism is forced convection, and spray cooling curve remains quite linear. In their experimental work, Pautsch and Shedd [4] implemented a unique technique to measure local film thickness and verified the dominance of forced convection in this regime.

For the two phase regime, several heat transfer mechanisms were proposed earlier, namely:

- Free surface evaporation.
- Boiling through surface nucleation.
- Boiling through secondary nucleation.
- Contact line heat transfer.

Pais et al. [5] suggested that free surface evaporation provides high heat transfer rates since liquid molecules from a thin liquid film can efficiently escape into vapor/ambient at the surface. As the liquid film thickness decreases, heat is conducted from the hot heater surface to the liquid/vapor interface with less resistance resulting in higher cooling performance.

Yang et al. [6] and Rini et al. [7] investigated boiling through surface and secondary nucleation, and observed that in addition to nucleation sites on the surface cavities, many more secondary nucleation sites are generated within the liquid layer as liquid droplets from spray strike on the liquid surface and entrain vapor. Additional bubbles that grow from secondary nucleation sites can greatly enhance boiling heat transfer and increase turbulent mixing within the film promoting convection and free surface evaporation.

Horacek et al. [8] obtained visualization and measurement of three phase contact line, the region where solid, liquid and vapor phases meet, during spray cooling experiments on a smooth surface. They found a strong correlation between contact line length and heat flux, and concluded that phase-change contribution to heat transfer is directly proportional to contact line length. Horacek et al. considered two possible mechanisms that might be responsible for heat transfer at the contact line, being either thin film heat transfer mechanism or an alternate mechanism such as transient conduction into the liquid when it moves over hot surface as observed in pool boiling.

The mechanisms behind the CHF are not known yet. One of the proposed mechanisms by Tilton [9] and Yang [10], backed by measurements of liquid influx and efflux, describes liquid splash off which increases with the heat flux and ultimately triggers CHF. Sehmbey at al. [11] suggested another mechanism based on macrolayer dryout model. According to this theory, bubbles at high heat fluxes start to coalesce, and subsequently they are broken by the impinging droplets or excessive internal pressure, causing to expel the upper liquid layer, and leave only a wetted patch of film on the heater surface. Finally, complete dryout occurs when incoming droplets cannot wet the surface anymore. Another possible CHF mechanism would be the homogenous nucleation within the liquid film [2].

More comprehensive spray cooling information focusing on high heat flux applications can be found in the review articles by Chow et al. [1] and Kim [2]. A detailed classification of the spray cooling applications is provided by Glassman [12] as well.

## 2.2 Spray Cooling of Enhanced Surfaces

Although a vast amount of research has been done on heat transfer enhancement in general, studies focusing on spray cooling enhancement are fairly limited. In early works, Pais et al. [13] and Sehmbey et al. [14] examined the effects of surface roughness and contact angle using water with air atomized nozzle, at flow rates up to 85 ml/cm$^2$-min water and 400 ml/cm$^2$-s air, and found enhancement in heat transfer coefficient with decreasing surface roughness and increasing contact angle. They obtained heat fluxes up to 1250 W/cm$^2$ at 11 $^o$C surface superheat on ultrasmooth ($R_a$=0.3 μm) copper surface.

Kim et al. [15] investigated spray cooling enhancement on microporous coated surfaces using water at flow rates up to 1.5 ml/cm$^2$-min. The porous layer was fabricated using a mixture of MEK, epoxy, and aluminum powder and its maximum thickness was 500 μm. They found that the CHF increased 50% relative to the uncoated surface. However, highest heat flux reached was 3.2 W/cm$^2$ at 65 $^o$C surface superheat due to very low flow rates.

Stodke and Stephan [16] studied spray cooling on microstructured and microporous surfaces using water at 60 mbar system pressure and 85 ml/cm$^2$-min flow rate. Pyramidal microgrooves and micropyramids with 75 μm height increased the wetted area by a factor of 1.4. Porous layer with 100 μm thickness was very similar to that used by Kim et al. [15] and created with the same ingredients. A maximum heat flux of 97 W/cm$^2$ was observed for the micropyramid surface compared to 30 W/cm$^2$ for the flat surface, both at a surface superheat of 12 $^o$C. This enhancement was much larger than the surface area enhancement. However, microporous surface caused a significant degradation in heat transfer compared to the uncoated surface resulting in 14 W/cm$^2$ maximum heat flux at 12 $^o$C superheat due to the poor thermal conductivity of the epoxy binder.

Amon et al. [17] and Hsieh and Yao [18] performed spray cooling experiments with water using 1x2 nozzle array at very low flow rates of up to 4.41 ml/cm$^2$-min on square microstuds with 160–480 μm heights. This surface texture on silicon was found to have little effect in the single phase and dry out regimes. The authors attributed the higher heat transfer observed for the microtextured surfaces in the intermediate regimes to more effective spreading of the liquid by capillary forces. The maximum heat flux achieved was just over 50 W/cm$^2$ at 55 $^{o}$C surface superheat.

Silk et al. [19] investigated the effect of surface geometry in spray cooling with PF-5060 using 2x2 nozzle array at 96 ml/cm$^2$-min flow rate. They used embedded structures (dimples, pores and tunnels) and compound extended structures (straight fins, cubic pin fins and dimples) all in the order of 1 mm size. Of these macrostructured surfaces, straight fins and porous tunnels performed the best providing a CHF of 175 W/cm$^2$ for gassy conditions at surface superheats of up to 36 $^{o}$C and offered CHF enhancement of 62% over flat surface.

Coursey et al. [20] recently performed spray cooling tests focusing on straight fin geometry with heights between 0.25 to 5 mm. They used PF-5060 at flow rates up to 62 ml/cm$^2$-min and found that fin heights between 1 to 3 mm were optimum for heat fluxes up to 124 W/cm$^2$ at 19 $^{o}$C surface superheat.

Most of the mentioned efforts [15 - 20] used various pressure atomized nozzles. Pais et al. [13] and Sehmbey et al. [14] employed air atomized nozzles in their tests where air flow field was thought to help thinning the liquid film and maintaining lower coolant partial pressures at evaporation surface eventually yielding higher heat transfer coefficients.

The reviewed spray cooling studies in this section are summarized in Table 2-2 for side by side comparison of important parameters. Data here includes maximum reported heat fluxes, surface superheats and corresponding heat transfer coefficients from enhanced surfaces with micro and macro structures having $R_a \geq 1$ μm.

Table 2-2: Comparison of Previous Studies on Spray Cooling of Enhanced Surfaces

| Author | Surface | Nozzle Type | Fluid/ $\dot{V}$ (ml/cm$^2$-min) | Max. $\Delta T_{sat}$ ($^o$C) | Max. h (W/m$^{2o}$C) | Max. q" (W/cm$^2$) |
|---|---|---|---|---|---|---|
| Kim et al. [15] | Micro-porous | Pressure atomized | Water<br>1.5 | 65 | 492 | 3.2 |
| Stodke and Stephan [16] | Micro pyramids | Pressure atomized | Water<br>85 | 11.5 | 83,348 | 97 |
| Amon et al. [17], Hsieh and Yao [18] | Micro studs | Pressure atomized | Water<br>4.4 | 55 | 3,650 | 52 |
| Silk et al. [19] | Macro straight fins | Pressure atomized | PF-5060<br>96 | 28 | 62,057 | 175 |
| Coursey et al. [20] | Macro straight fins | Pressure atomized | PF-5060<br>62 | 19 | 65,263 | 124 |

# CHAPTER 3: EXPERIMENTAL SETUP AND PROCEDURE

The following chapter describes the experimental setup and procedures used to conduct the present study. Detailed descriptions of the spray cooling setup, working fluid, spray nozzle, heaters and spray surfaces, and test conditions and procedures were presented. Infrared thermography was introduced next, along with required preliminary measurements. At the end of the chapter, uncertainty estimations of the main measured quantities were given briefly.

## 3.1 Spray Cooling Setup

Experiments were conducted in a closed loop spray cooling system. Figure 3-1 includes the schematic diagram of the system where main components are reservoir, 1x2 nozzle array, subcooler, condenser, and pump. In this setup, the reservoir supplies ammonia liquid and vapor to the nozzle array. Liquid and vapor mixes in the atomizer nozzles and the resulting spray cools a 1 cm x 2 cm heater where heat source thick film resistors are mounted. Exhaust from 1x2 nozzle array slightly subcools the incoming liquid supply in a small heat exchanger before flowing into the larger heat exchanger to condense. Finally, RINI's two phase pump takes the liquid and vapor ammonia and transfers it back to the reservoir, providing the pressure difference that is needed to drive ammonia in the cycle and generate the spray. A separate air cooled R-22 cycle is employed to reject heat from the ammonia cycle to the ambient. System allows controlling flow rates and pressures across the nozzle array and is equipped with computer controlled data acquisition system for accurate data recording.

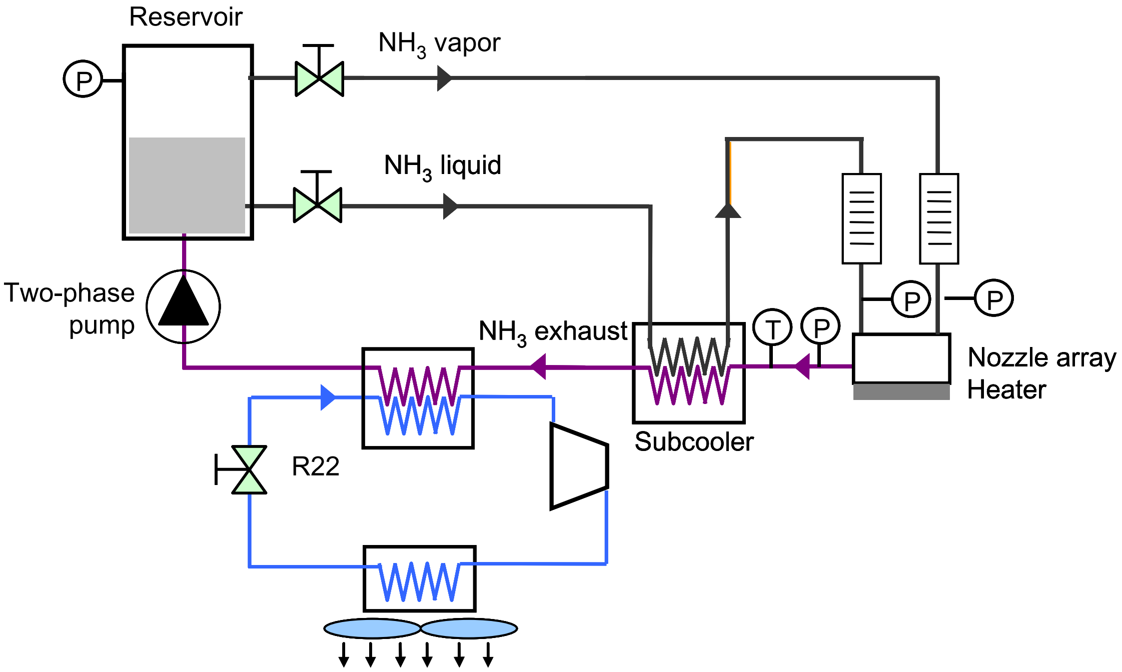

Figure 3-1: Schematic Diagram of the Spray Cooling Setup

## 3.2 Working Fluid

In the present work, anhydrous ammonia (Refrigerant 717) was used as the working fluid. Ammonia possesses certain advantages due to its thermophysical properties that are outlined in Table 3-1 along with those from two widely adapted coolants. First, ammonia has the second highest latent heat of vaporization after water among refrigerants enabling high heat flux removal. For applications that require low temperature device operation, ammonia becomes advantageous to water by offering lower saturation temperature at a given pressure. Ammonia however, is not compatible with all of the commonly used engineering materials, and requires careful material selection and component design for its implementation in cooling systems.

Table 3-1: Thermophysical Properties of Selected Fluids at Atmospheric Pressure [21, 22]

| Property | Ammonia ($NH_3$) | FC-72 ($C_6F_{14}$) | Water ($H_2O$) |
|---|---|---|---|
| $P_{sat}$ (kPa) | 101.3 | 101.3 | 101.3 |
| $T_{sat}$ ($^oC$) | -33.4 | 56 | 100 |
| $\rho_l$ ($kg/m^3$) | 682 | 1593.8 | 958.3 |
| $\rho_v$ ($kg/m^3$) | 0.86 | 13.2 | 0.597 |
| $h_{fg}$ (kJ/kg) | 1368 | 88 | 2256.7 |
| $c_p$ (kJ/kg.$^oC$) | 4.472 | 1.10 | 4.22 |
| $\mu_l$ (kg/m.s) | $285 \times 10^{-6}$ | $430 \times 10^{-6}$ | $278 \times 10^{-6}$ |
| $k_l$ (W/m.$^oC$) | 0.614 | 0.057 | 0.679 |
| $\sigma$ (N/m) | $33.9 \times 10^{-3}$ | $10 \times 10^{-3}$ | $58.9 \times 10^{-3}$ |

## 3.3 Spray Nozzle

RINI’s highly compact 1x2 vapor atomized nozzle array, shown in Figure 3-2, was used in all tests. In these nozzles a fine liquid stream is injected into a high velocity vapor stream. The shear force created by the vapor stream atomizes the liquid into fine droplets that are ejected from the nozzle orifice. Figure 3-2 also indicates the pressure and temperature measurement ports on the nozzle array that were needed to determine the driving pressures across the nozzle, and saturation condition of the coolant.

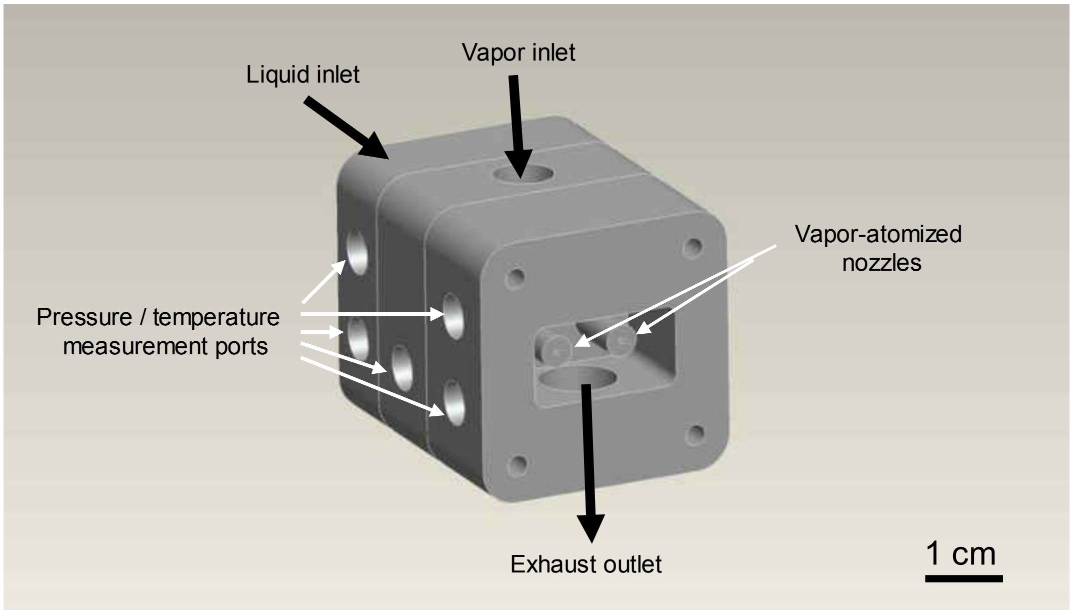

Figure 3-2: RINI 1x2 Vapor Atomized Nozzle Array

One of the parameters that affect spray cooling performance is the distance from nozzle orifice to the surface for a specific type of nozzle. Nozzle-to-surface distance of 11 mm was determined to be adequate for each spray to cover 1 $cm^2$ area, and therefore it was held constant. Nozzle array was then tested to visually inspect the spray quality in terms of droplet size and mass flux distribution, as well as alignment and coverage in the target surface. Spray patterns were observed through a borosilicate sight window that replaced the spray cooled surface of an actual heater, and oriented normal to the nozzle tip. Liquid and vapor flow rates were varied to change the spray conditions, and some still images were recorded as shown in Figure 3-3. Within the tested range of flow rates, sprays had a solid-cone pattern characterized by very fine, uniformly distributed droplets. As can be noticed, there is no obvious difference to the naked eye when these images of spray patterns are compared.

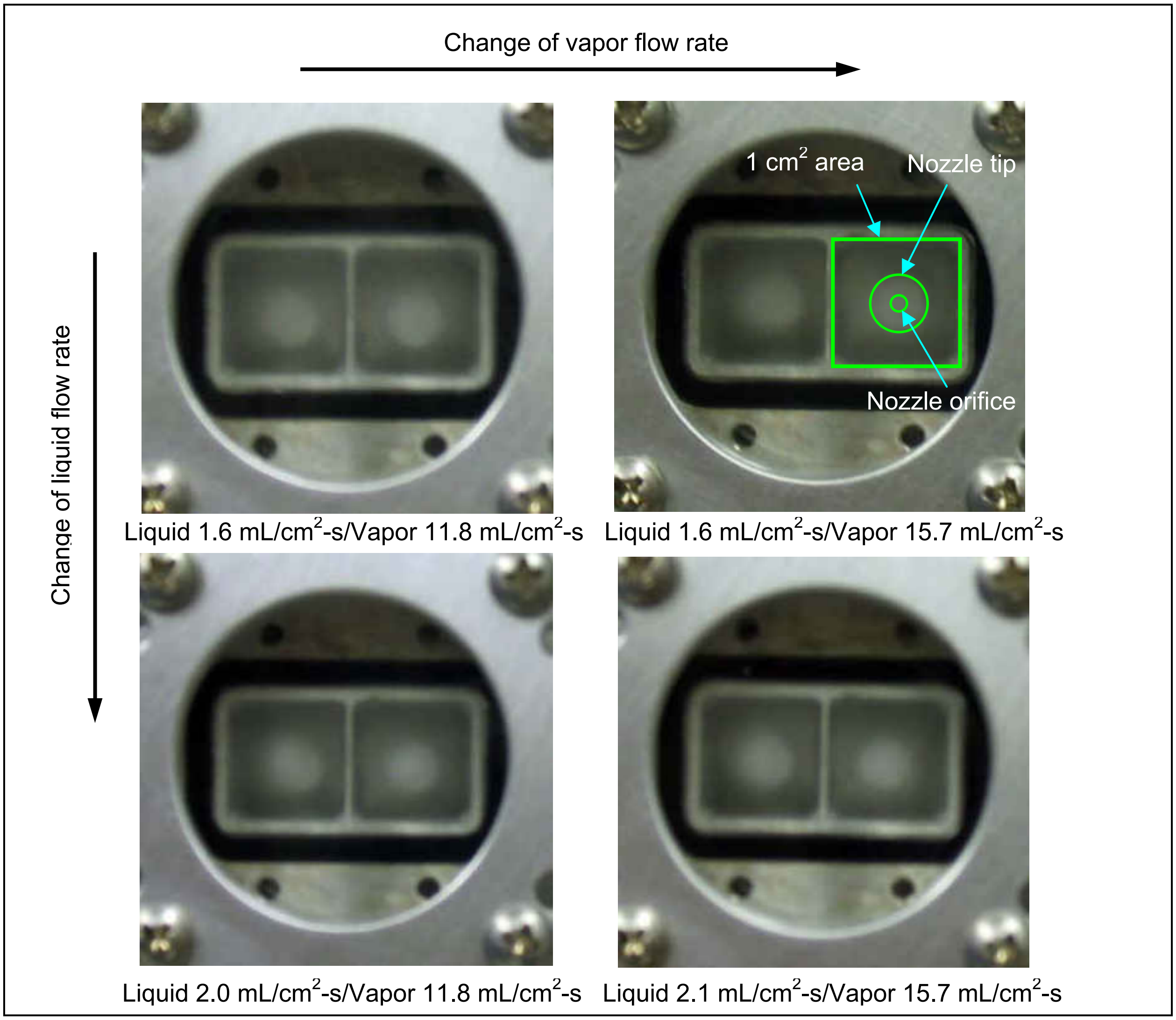

Figure 3-3: Photographs of Spray Patterns at Various Flow Rates

## 3.4 Heaters and Spray Surfaces

Two types of heater designs were employed in this study as shown in Figure 3-4. Although they had a common spray surface area on one side, they had either 1 cm x 2 cm or 1 cm x 1 cm heated areas on the opposite side, featuring two- or one-1 $cm^2$ thick film resistors, respectively, that were soldered onto heater to simulate heat generating device.

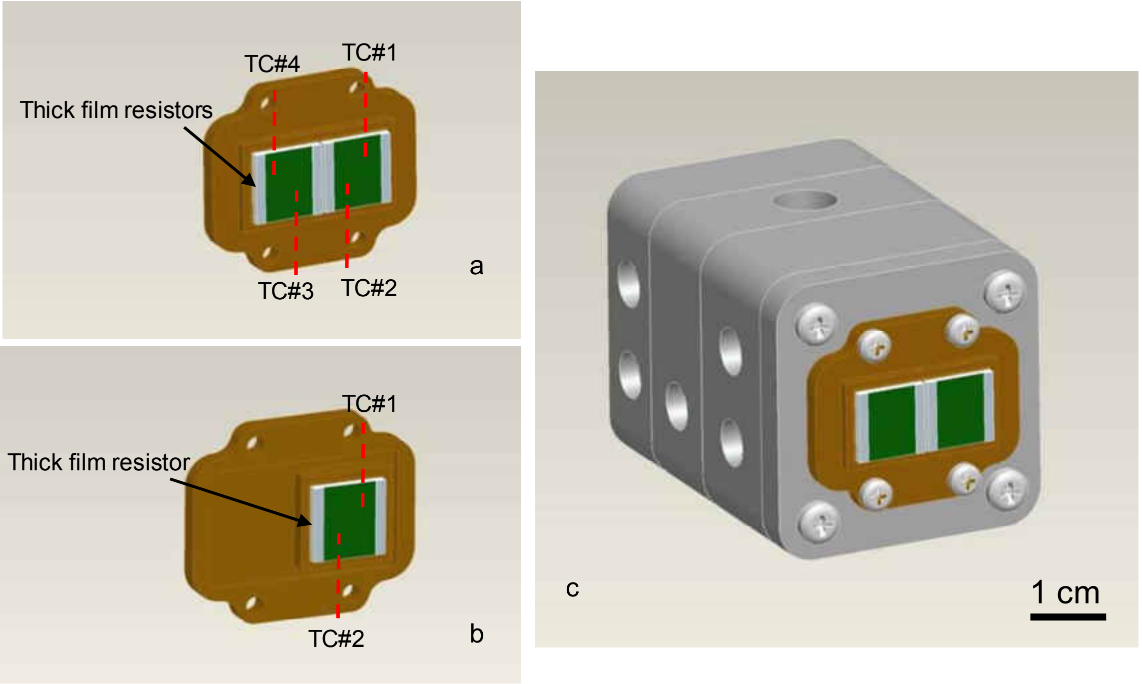

Figure 3-4: 1x2 Heater (a), 1x1 Heater (b), and Complete 1x2 Nozzle Array and Heater Assembly (c)

Heat flux $q''$ was determined from the total power supplied into the thick film resistors per unit base area, and defined as:

$$q'' = \frac{V\,I}{A} \tag{1}$$

where, $V$ is the voltage drop across the heater, $I$ is the current, and $A$ is the resistor base area. Heater temperature was monitored with four (or two) fine gage thermocouples (30 AWG, type-T) embedded halfway in the heater wall and spaced equally across the 2 (or 1) cm$^2$ area. Spray surface temperature $T_{surf}$ was calculated by extrapolating the measured temperature, with the assumption of steady 1-D conduction through heater wall, as:

$$T_{surf} = TC_{avg} - \frac{(q''x)}{k} \tag{2}$$

where, $TC_{avg}$ is the average of four (or two) thermocouple readings, $x$ is the known distance to the surface, and $k$ is the thermal conductivity of the heater wall. In practice, when thick film resistors are replaced with the actual device (such as laser diodes), temperature at the mounting surface can be estimated by starting with the surface superheat, extrapolating it through the actual wall thickness, used in that particular design, and adding the saturation temperature of ammonia at the system operation pressure.

Heaters used in the initial evaluation of enhanced surfaces, and later in comprehensive investigation of enhanced surfaces for highest heat transfer coefficient and CHF were made out of different materials to facilitate testing at each stage of the study. Table 3-2 lists the heater materials where, as can be noticed, the ones selected for spray surface were all ammonia compatible.

Table 3-2: Classification of Test Heaters Based on Heater Material

| | | | Material | |
|---|---|---|---|---|
| Type | Test purpose | Heated area | Heater body | Spray surface |
| # | Initial evaluation | 1 cm x 2 cm | Cu | Al |
| A | Investigation of highest ***h*** | 1 cm x 2 cm | Al 6061 | Al 6061 |
| C | Investigation of ***CHF*** | 1 cm x 1 cm | Cu | Ni |

Based on the outlined technical approach, heaters featured various surface structures that can be mainly grouped as micro-, macro- and multi-scale structured surfaces. As part of these groups, there were various test heaters that allowed investigation of structure geometry and size effects. Performance of each test heater was compared to the reference heater with machine finished-smooth surface, to obtain quantitative comparison. A classification of test heaters based on the mentioned surface characteristics is provided in Table 3-3.

Table 3-3: Classification of Test Heaters Based on Surface Characteristics

| | Structural parameter | Surface condition |
|---|---|---|
| | | **Smooth** |
| | Geometry | plain |
| | Size (roughness level) | machine finish |
| **Enhanced Surfaces** | | **Micro structured** |
| | Geometry | plain / micro indentations / micro protrusions |
| | Size (roughness level) | polished / fine / medium / coarse |
| | | **Macro structured** |
| | Geometry | pyramids / triangular grooves / straight fins / pin fins |
| | Size (mm) | 0.75 / 0.50 / 0.25 |
| | | **Multi-scale structured** |
| | Geometry | optimum Macro + micro geometry (indentation/protrusion) |
| | Size (mm/roughness level) | optimum Macro + micro size |

In an effort to provide heater names that describe heater material, surface enhancement type, structure geometry, and structure size, a nomenclature was developed as illustrated in Figure 3-5. Although complete heater names were identified on plots (e.g. A39Mpy-0.50mp-c), during the discussion of the results heater type and fabrication number was dropped from the name to describe only surface condition of the heater (e.g. Mpy-0.50mp-c).

Figure 3-6 includes some schematics and solid models of micro- and macrostructured surfaces to help visualize their surface characteristics in general.

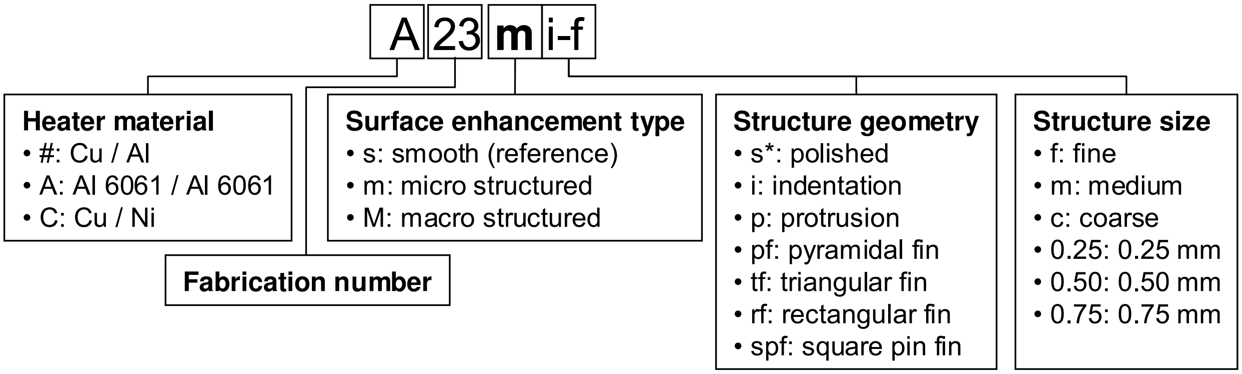

As an example, A 39 **M** py-0.25 **m** p-c refers to an Al 6061 heater with multi-scale structured surface featuring 0.25 mm high pyramids and coarse size micro protrusions

Figure 3-5: Description of Heater Names

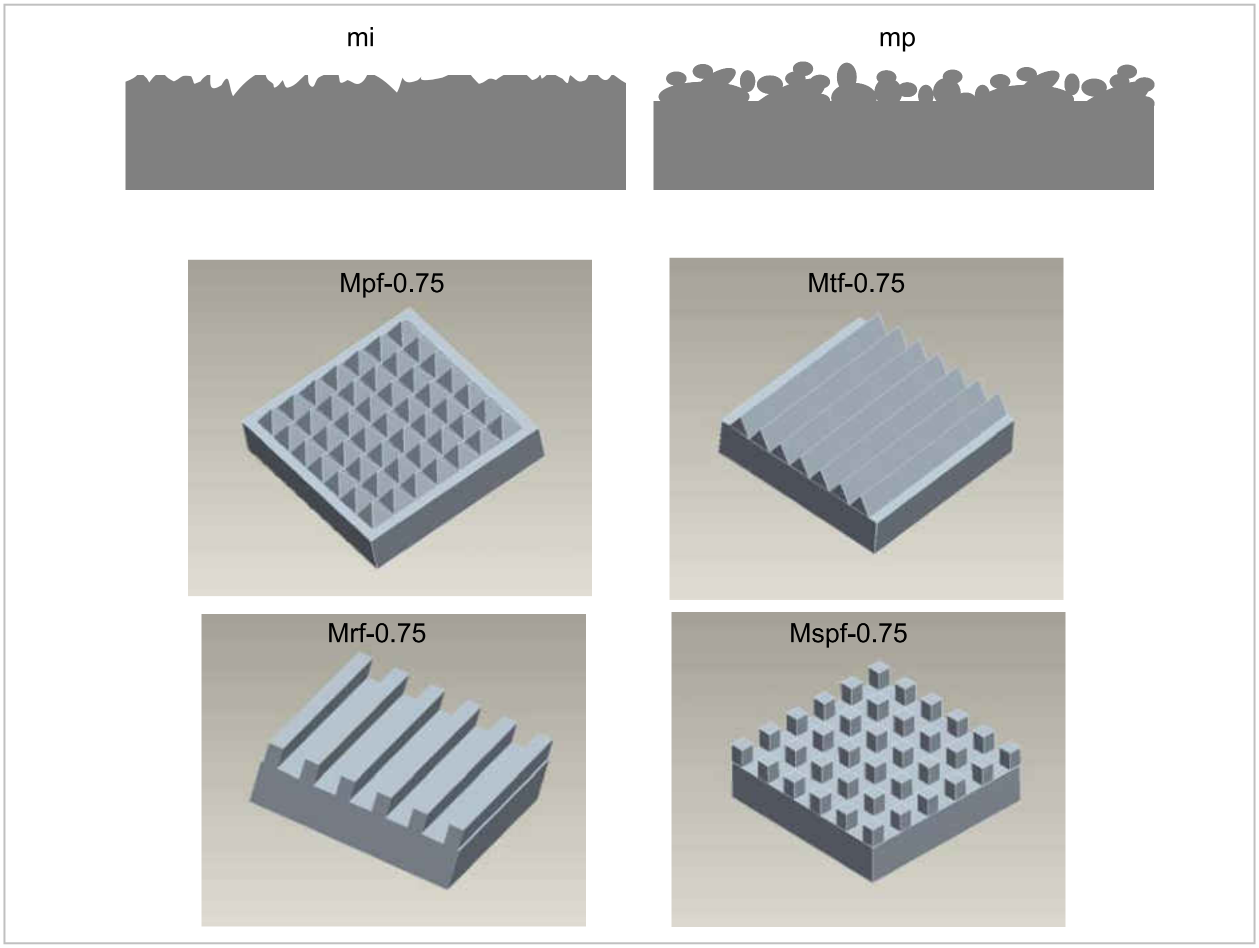

Figure 3-6: Schematics of Microstructured and Solid Models of Macrostructured Surfaces

Unlike the macrostructured surfaces, microstructured surfaces required additional efforts for characterization. First, scanning electron microscopy (SEM) method was utilized with JEOL 6400F and Zeiss ULTRA-55 FEG devices operated at 5 keV to determine the morphology of the surfaces. Figure 3-7 to Figure 3-12 include SEM images of six microstructured surfaces with indentations and protrusions at various roughness levels. Each figure includes images taken at 100X and 500X magnifications, providing both an overall and detailed view. Surfaces with micro size protrusions also offer many randomly sized re-entrant cavities, as indicated in Figure 3-10.

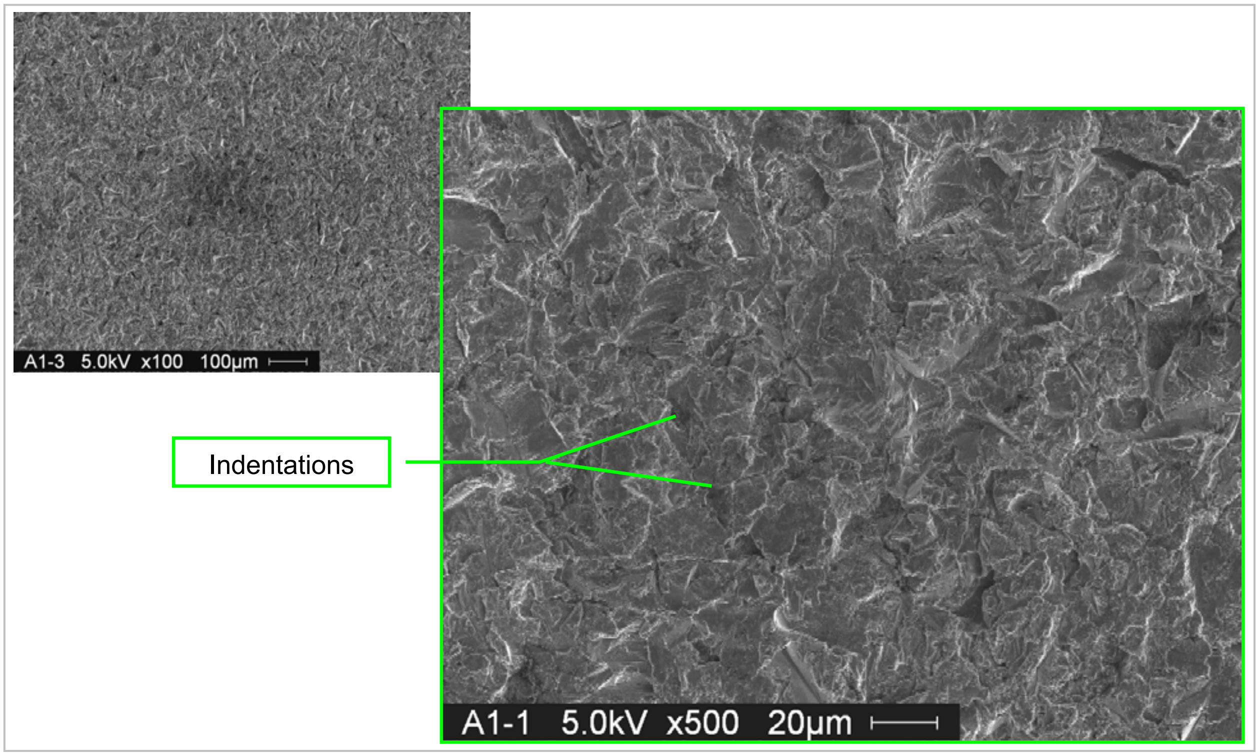

Figure 3-7: SEM Images of the Surface ***mi-f***

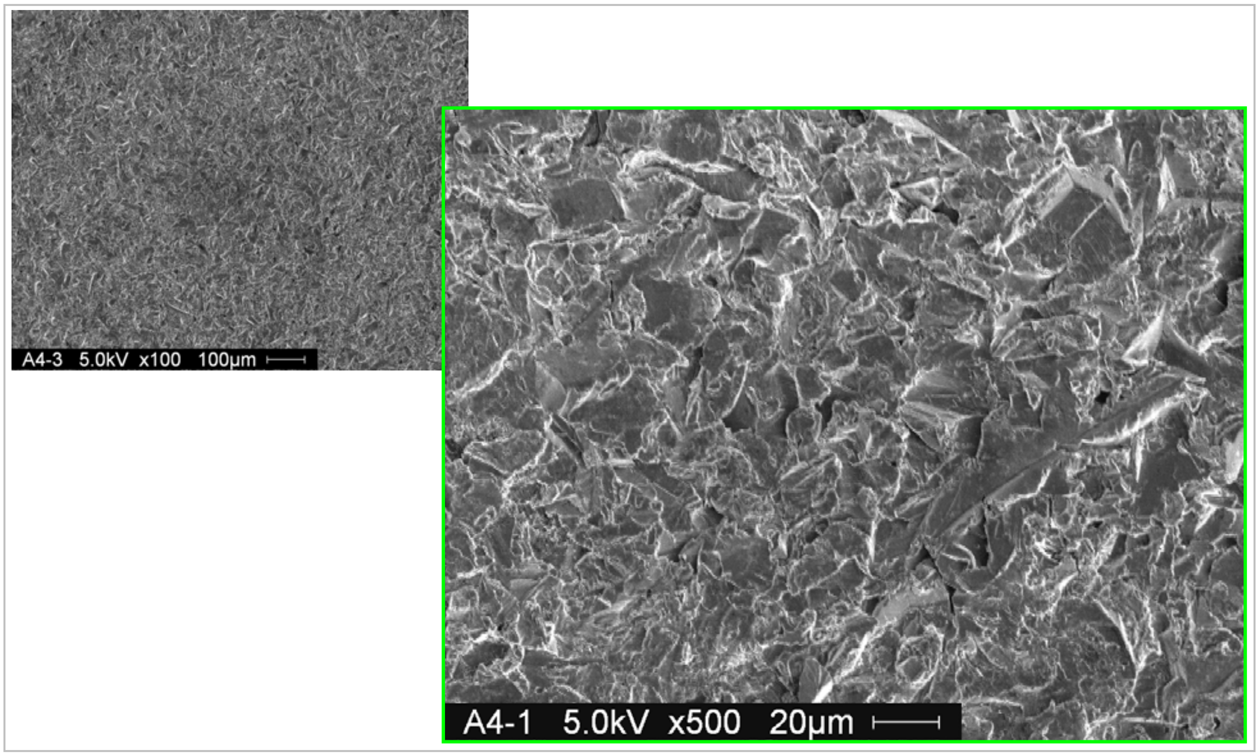

Figure 3-8: SEM Images of the Surface ***mi-m***

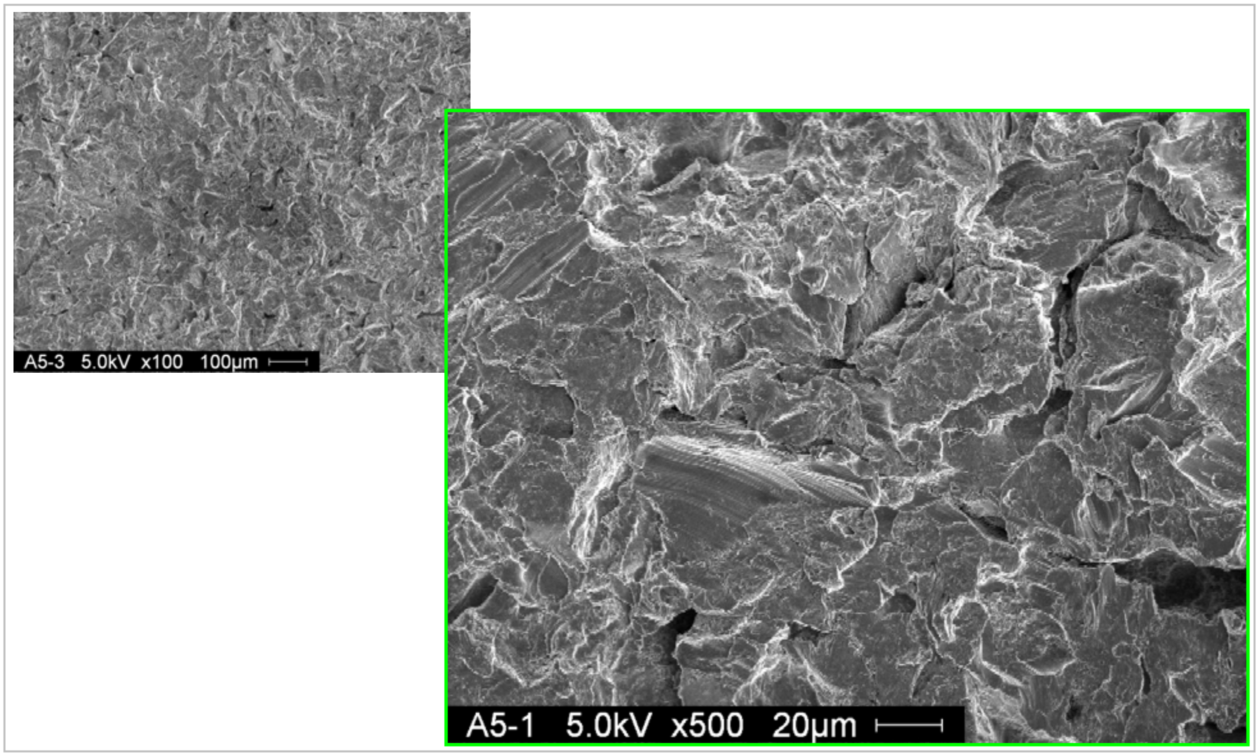

Figure 3-9: SEM Images of the Surface ***mi-c***

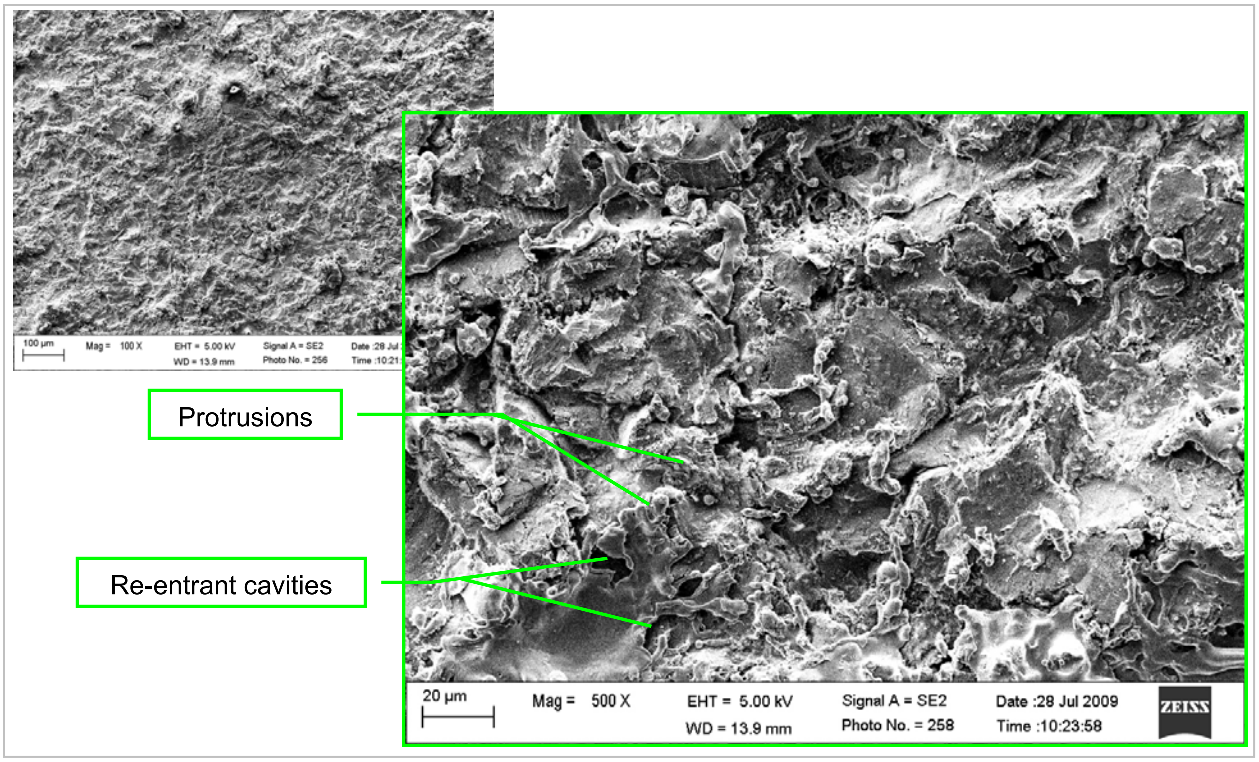

Figure 3-10: SEM Images of the Surface ***mp-f***

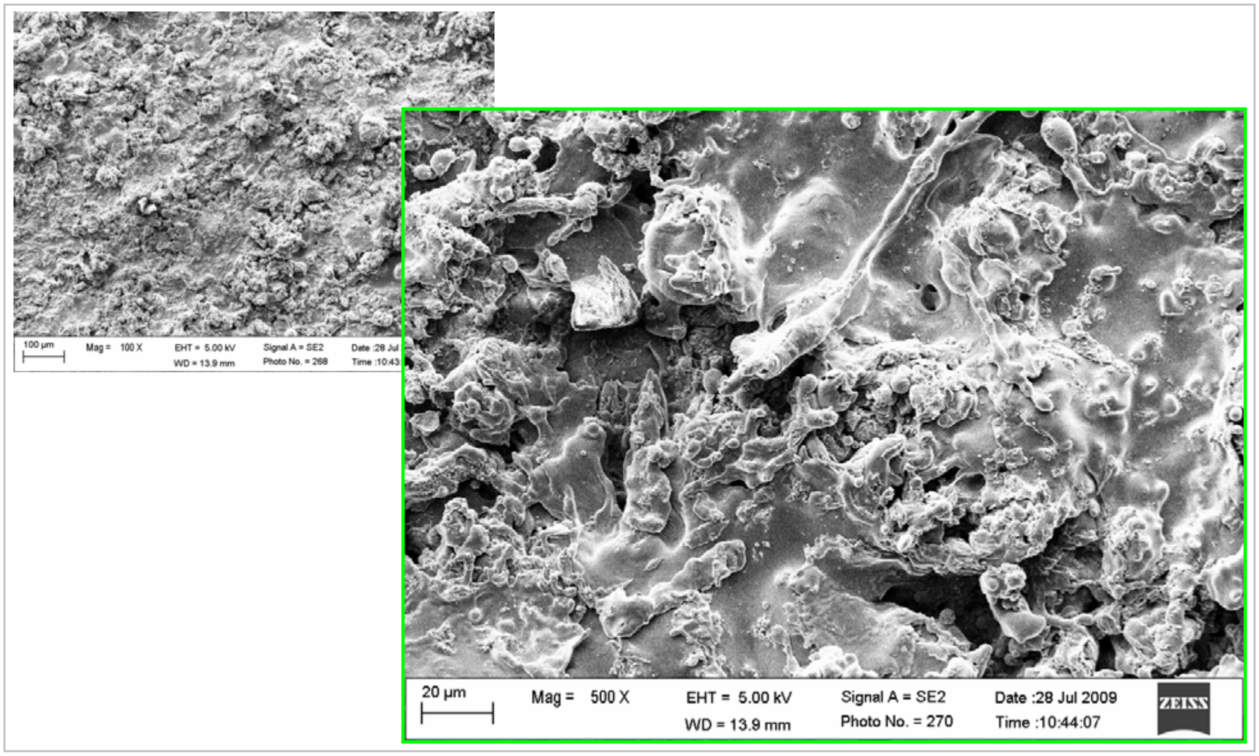

Figure 3-11: SEM Images of the Surface ***mp-m***

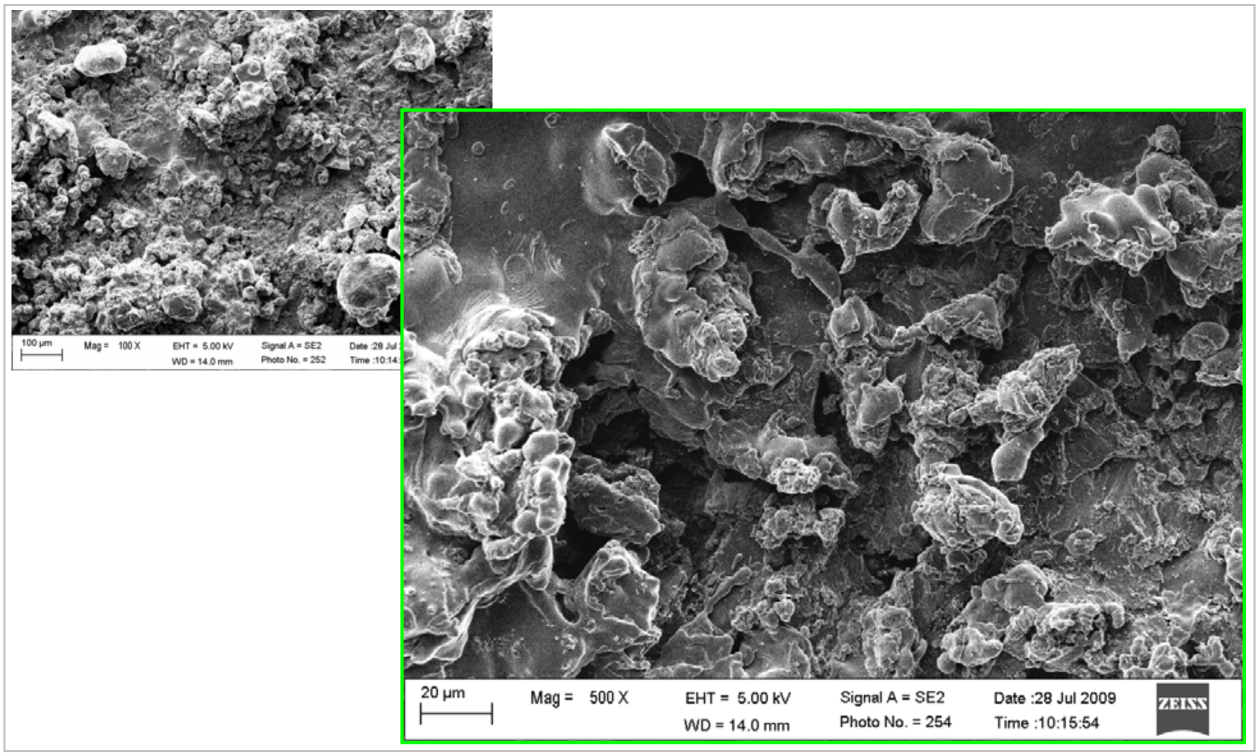

Figure 3-12: SEM Images of the Surface ***mp-c***

In addition to SEM imaging, a confocal scanning laser microscope (Olympus LEXT OLS3100) was also used for further characterization of micro structured surfaces. Figure 3-13 and Figure 3-14 include 3-D images of surfaces with indentations and protrusions, taken by scanning 1.28 mm x 0.96 mm area. Although these images are not as detailed or revealing as SEM images, they enable roughness analysis with the help of software.

Roughness data from all surfaces are presented with statistical and extreme-value height descriptors in Figure 3-15 and Figure 3-16 along with their mathematical definitions. The most commonly used roughness parameter, arithmetic mean roughness ($R_a$), ranges between 0.3 μm for the surface ***s***, to 19.5 μm for the surface ***mp-c***. The surfaces ***mp(-f,-m,-c)*** in general have higher roughness than the surfaces ***mi(-f,-m,-c)***. However, $R_a$ parameter alone would be misleading, since surfaces with widely different profiles, shapes, and frequencies can exhibit the same $R_a$ value [23, 24]. Thus, another parameter, mean height of roughness curve elements ($R_c$), was also considered, which basically confirmed the same trend.

For even a broader view, extreme-value height descriptors, maximum peak height ($R_p$), maximum valley depth ($R_v$) and maximum roughness height ($R_z$), are useful. As shown in Figure 3-16, the deepest valley is 77.6 μm for the surface ***mp-c***, while its maximum roughness height reaches 308.6 μm. In order to avoid occasional unrepresentative peaks and valleys in the characterization, a different roughness parameter, 10-point mean roughness ($R_{zjis}$), representing the highest five peaks and deepest five valleys, was also verified.

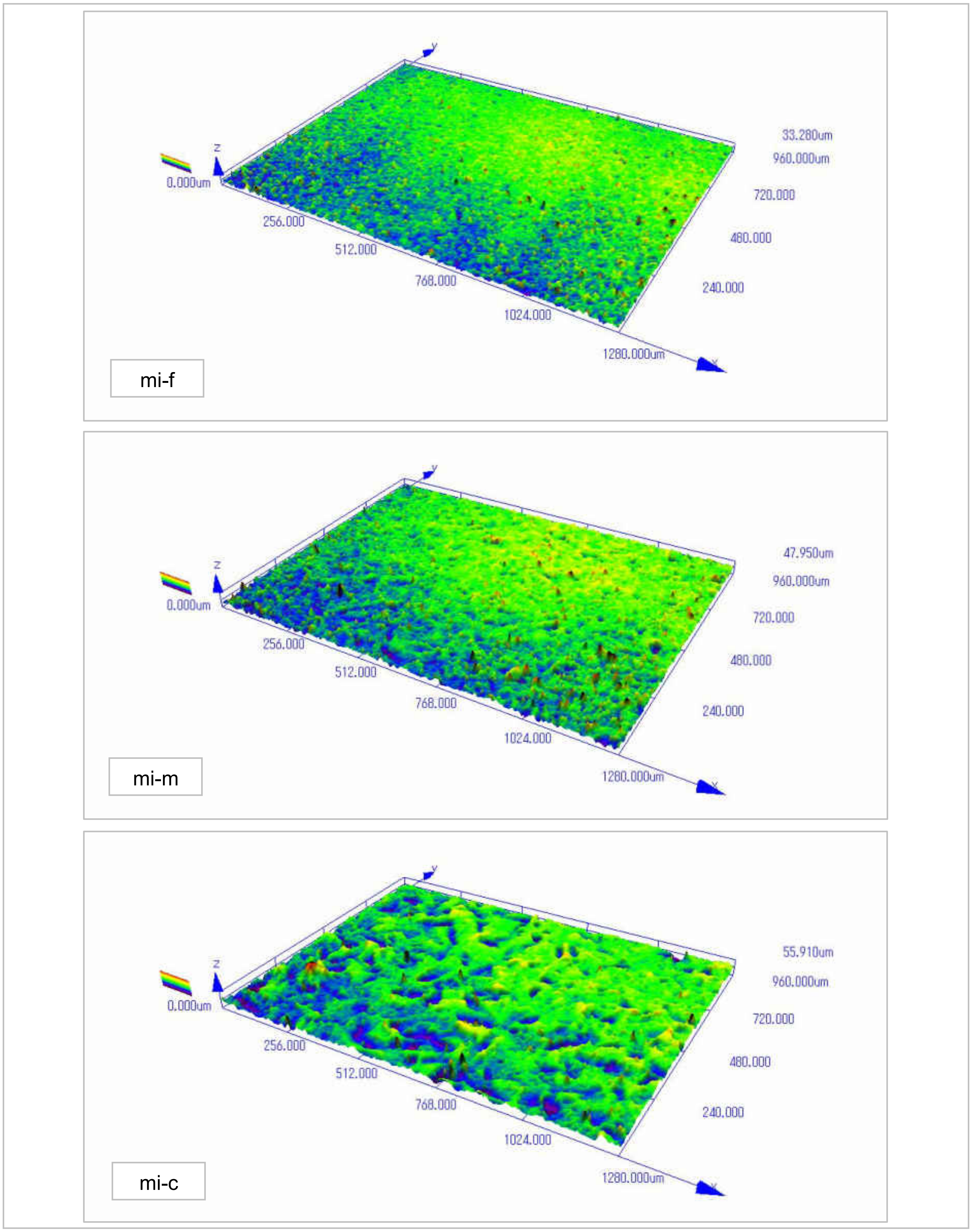

Figure 3-13: Confocal Scanning Laser Microscope Images of the Surfaces ***mi(-f,-m,-c)***

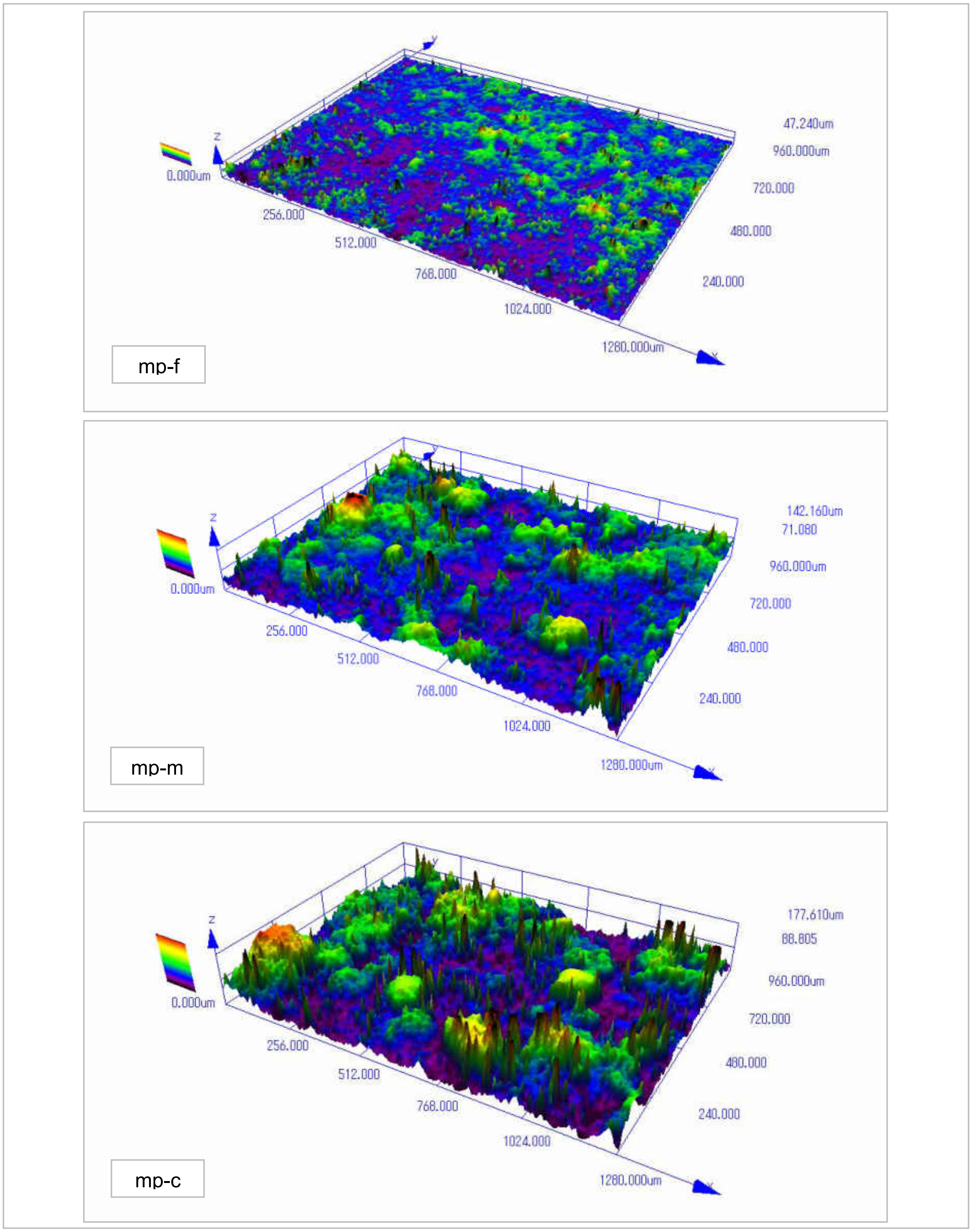

Figure 3-14: Confocal Scanning Laser Microscope Images of the Surfaces ***mp(-f,-m,-c)***

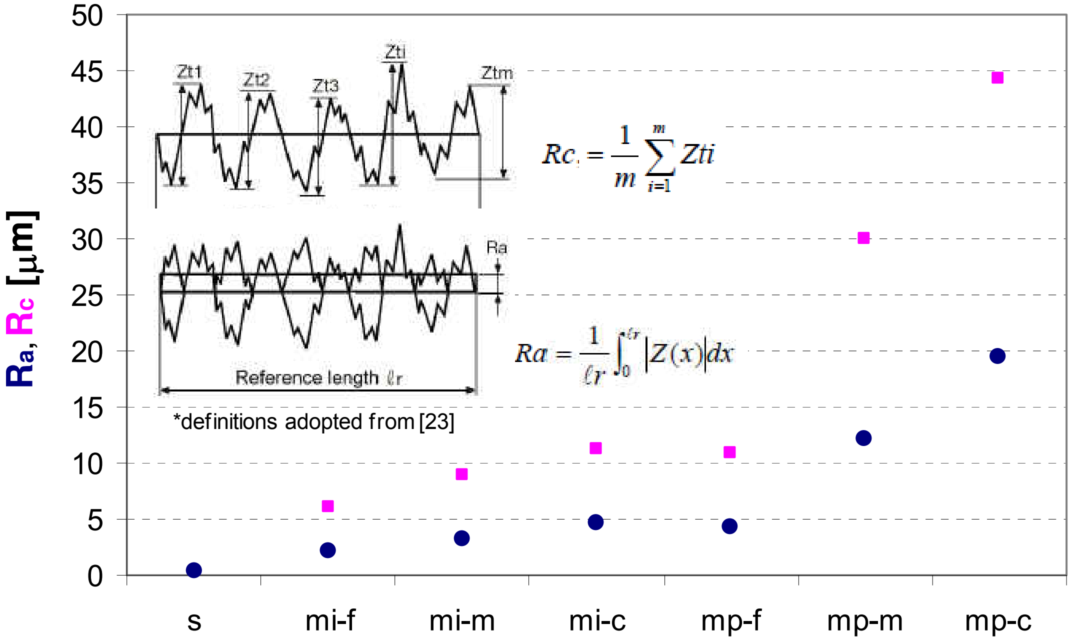

$$Rc = \frac{1}{m}\sum_{i=1}^{m} Zti$$

$$Ra = \frac{1}{\ell r}\int_0^{\ell r} |Z(x)|dx$$

Figure 3-15: Roughness of Microstructured Surfaces with Statistical Height Descriptors

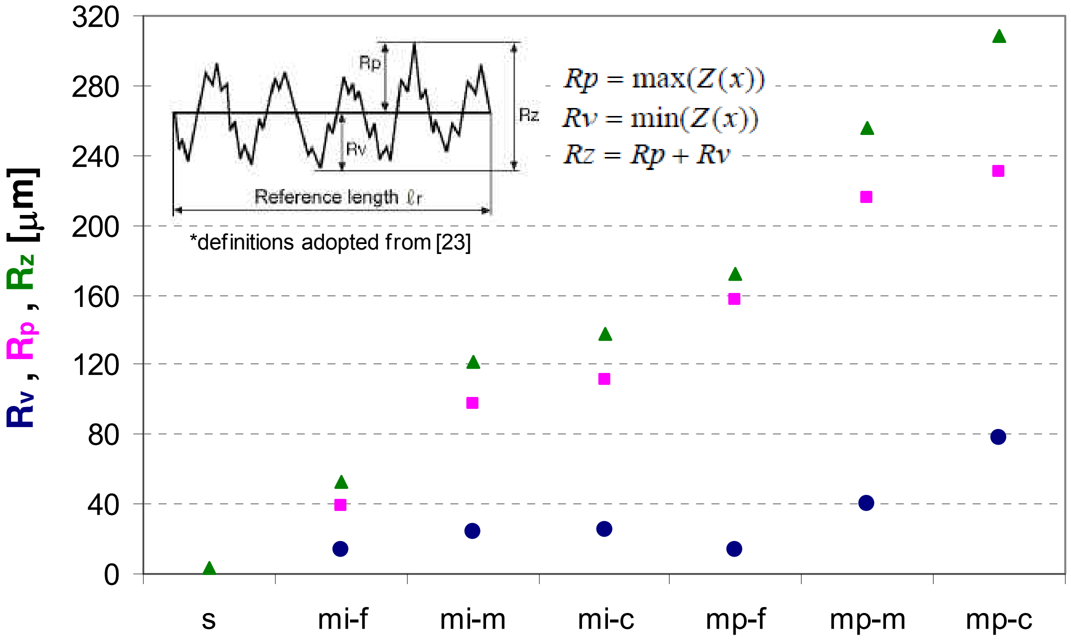

$$Rp = \max(Z(x))$$
$$Rv = \min(Z(x))$$
$$Rz = Rp + Rv$$

Figure 3-16: Roughness of Microstructured Surfaces with Extreme-Value Height Descriptors

Another useful set of data obtained from the surface analysis with confocal laser scanning microscope was the actual surface area of the scanned section. This information was used to define an area enhancement factor $EF_A$, as:

$$EF_A = \frac{A_{surface}}{A_{projected}} \tag{3}$$

where $A_{surface}$ is the surface area, and $A_{projected}$ is the projected area. Figure 3-17 plots $EF_A$ values of all microstructured surfaces. As can be expected, with increased roughness, available surface area for a fixed projected area increases. Data indicated that area enhancement for the surface ***mp-c*** reaches 2.8. It should be noted that since the microscope cannot scan and capture the re-entrant cavities very well, these values for the surfaces ***mp(-f,-m,-c)*** are conservative and believed to be even higher.

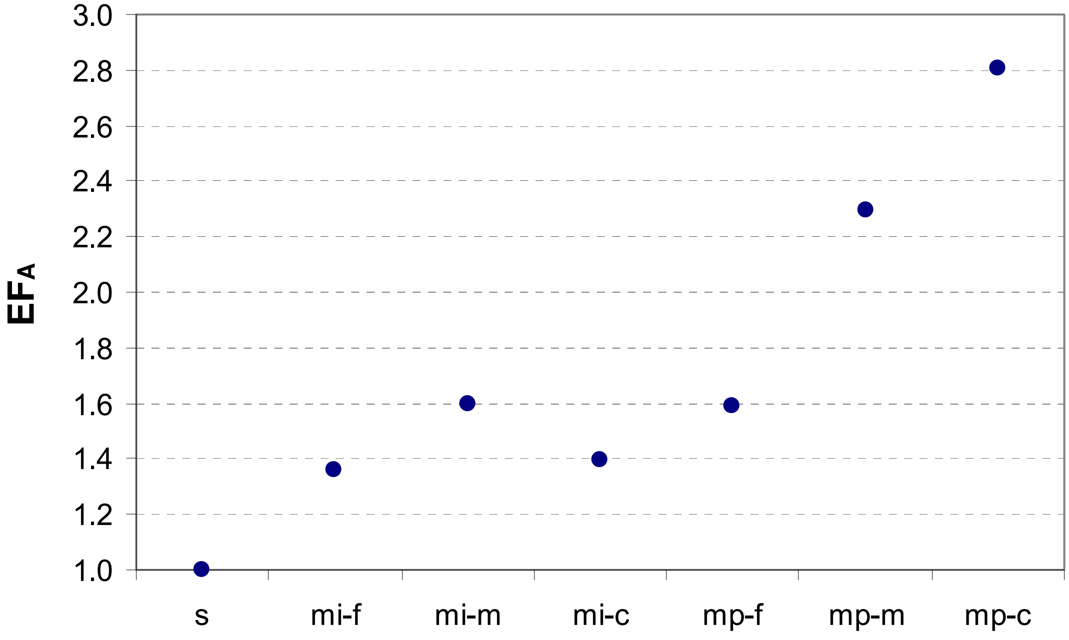

Figure 3-17: Area Enhancement Factor Provided by Microstructured Surfaces

### 3.5 Test Conditions and Procedure

All the tests were conducted using saturated ammonia at 550-570 kPa (65-68 psig) and 7-8 $^{o}$C conditions. Cooling curves, in the form of surface superheat ($\Delta T_{sat} = T_{surf} - T_{sat}$) vs. heat flux (q”), were generated for each test heater by increasing the heat flux gradually and recording the corresponding heater temperatures at certain sampling rates.

After the visual inspection of spray patterns, a series of tests were performed in order to find the optimum flow rates that balances high heat transfer rate, and reasonably low coolant usage and pumping power. In these tests, a type ***A*** heater with the surface ***s*** (machine finished-smooth) was utilized, and liquid flow rate was first varied between 1.4 to 1.8 mL/cm$^2$-s, at constant vapor flow rate of 15.7 mL/cm$^2$-s. Data in Figure 3-18 illustrate that increase in liquid flow rate from 1.4 to 1.6 mL/cm$^2$-s clearly improves the heat transfer, but further increase to 1.8 mL/cm$^2$-s results in practically the same cooling curve. Therefore, in the next step, effect of vapor flow rate was examined for the constant 1.6 mL/cm$^2$-s liquid flow rate. Data in Figure 3-19 suggest that varying vapor flow rate in the range of 11.8 to 15.7 mL/cm$^2$-s does not change the spray characteristics much, and have no considerable effect on the heat transfer. Based on these data, optimum flow rates were determined to be 1.6 mL/cm$^2$-s for liquid, and 13.8 mL/cm$^2$-s for vapor (corresponding to 48 kPa (7 psi) pressure drop across the nozzle), and they were applied for tests that investigated highest heat transfer coefficient. Higher flow rates of up to 2.1 mL/cm$^2$-s for liquid, and 17.7 mL/cm$^2$-s for vapor (corresponding to 83 kPa (12 psi) pressure drop across the nozzle), were only employed for those tests that investigated CHF.

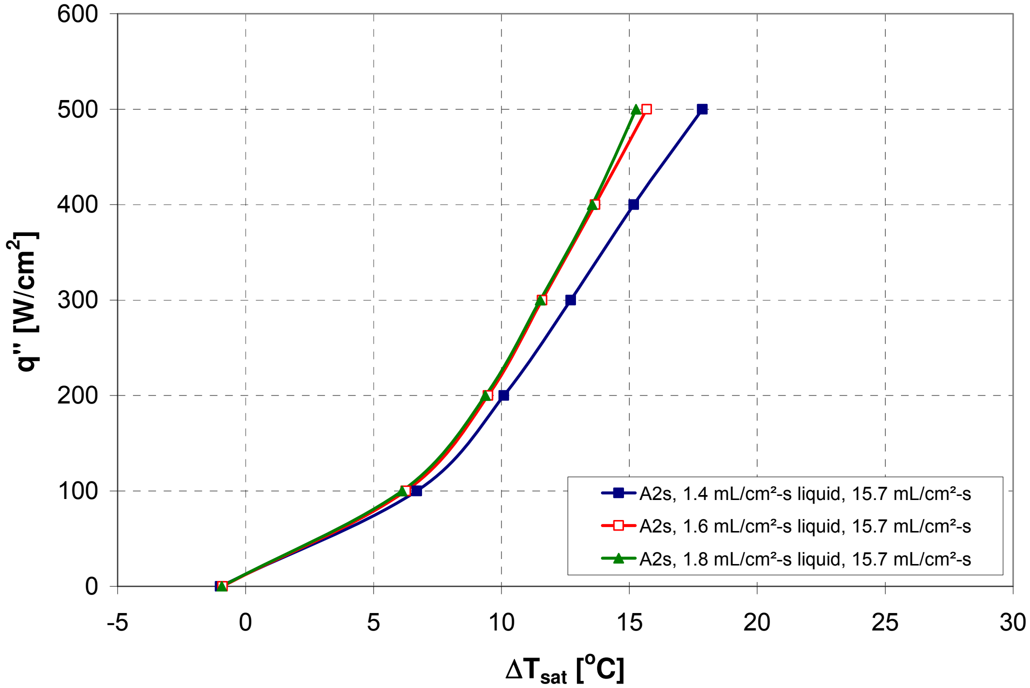

Figure 3-18: Effect of Liquid Flow Rate on Cooling Performance

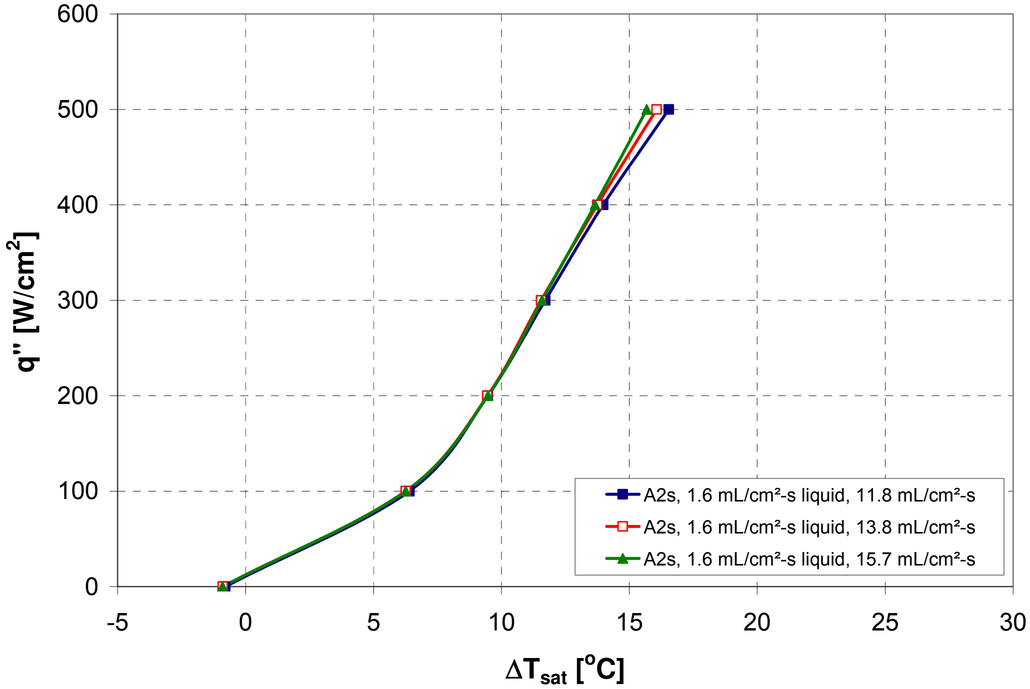

Figure 3-19: Effect of Vapor Flow Rate on Cooling Performance

Two tests were run to determine whether the magnitude and duration of the heat flux steps in the generation of cooling curves are critical. In the first test, heat flux was gradually increased in steps of 100 W/cm$^2$ up to 500 W/cm$^2$, and the corresponding heater temperatures were recorded every 3 seconds over 5 minutes long duration as shown in Figure 3-20. In the following test, heat flux was increased in smaller steps of 25 W/cm$^2$ lasting over a shorter period of 3 minutes as illustrated in Figure 3-21. As can be seen, surface superheats reach steady-state very quick, well before the 3 minutes mark at each heat flux level.

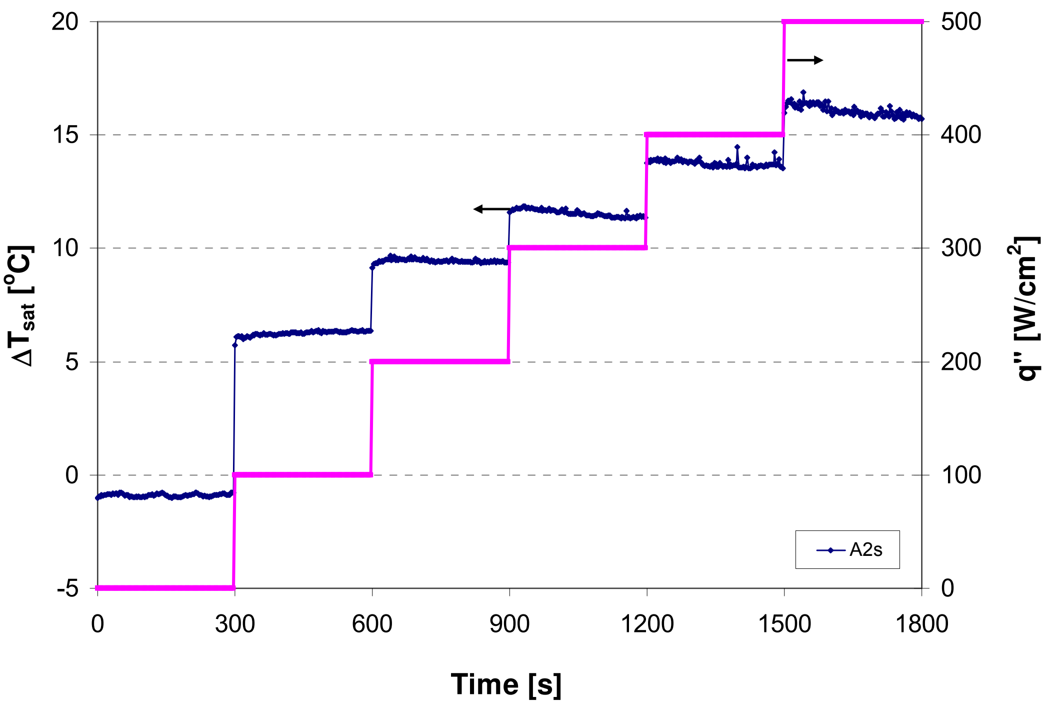

Figure 3-20: Heat Flux Steps with 100 W/cm$^2$ Magnitude and 5 Minutes Long Duration

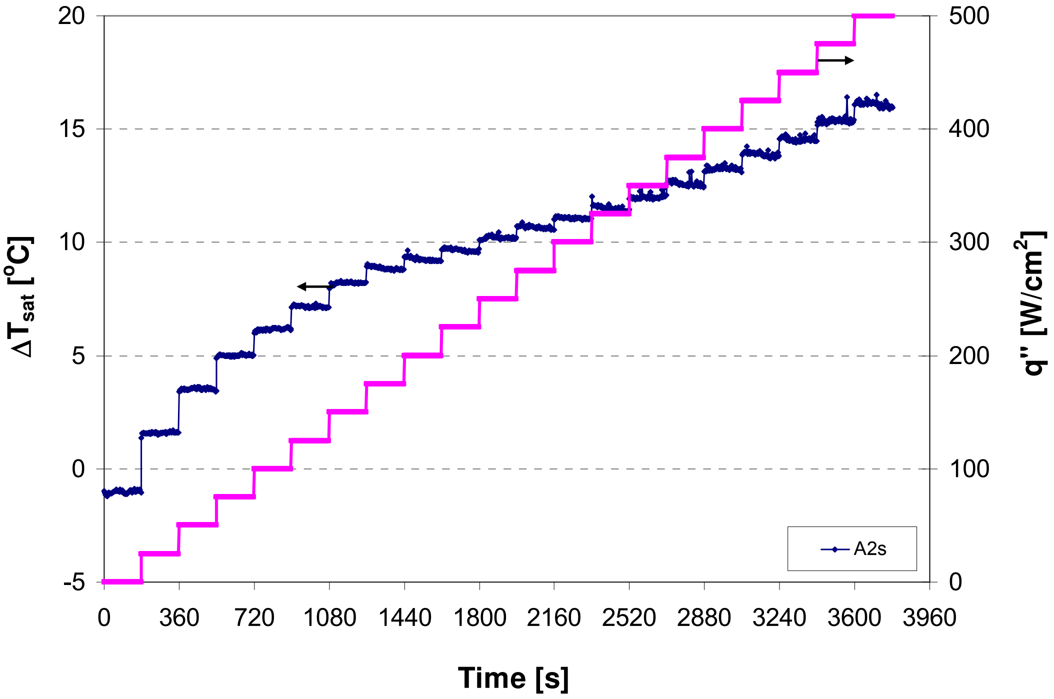

Figure 3-21: Heat Flux Steps with 25 W/cm$^2$ Magnitude and 3 Minutes Long Duration

The cooling curves in Figure 3-22, generated based on the data from Figure 3-20 and Figure 3-21 for comparison, match very well and indicate flexibility in the selection of the heat flux steps in tests. Heat flux control parameters determined for different stages of the study are outlined in Table 3-4. For the majority of the tests, heat flux was changed in steps of 50 W/cm$^2$ every 3 minutes. For CHF tests however, heat flux was changed in steps of as low as 10 W/cm$^2$ every 1 minute. This adjustment for the high heat flux ranges enabled keeping the overall testing time at a reasonable level, and approaching CHF in a slower and controllable pace.

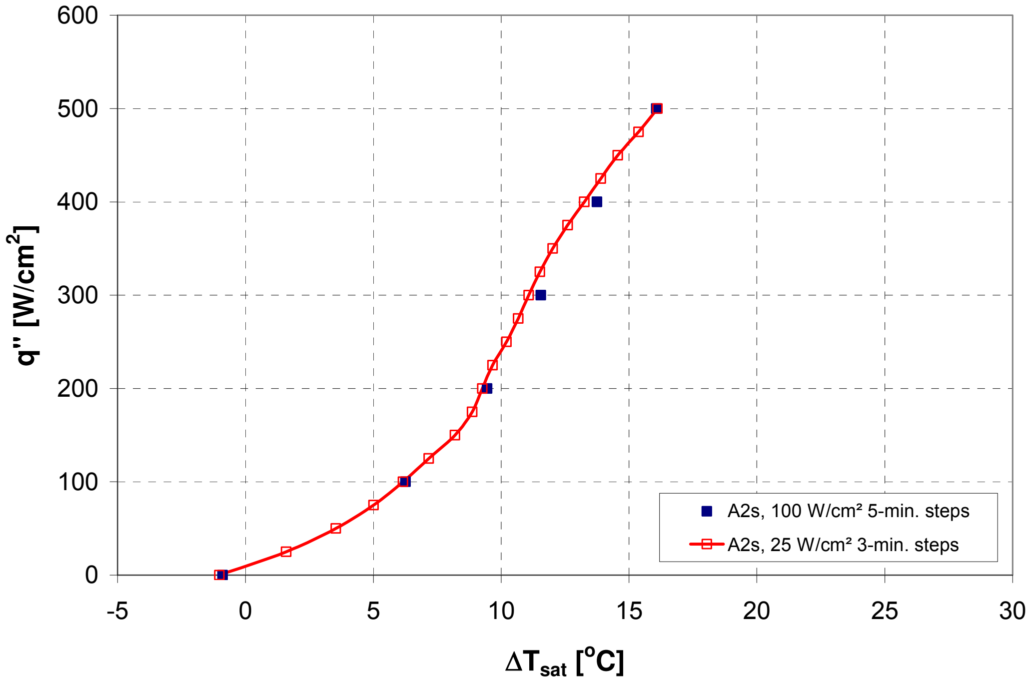

Figure 3-22: Comparison of Cooling Curves with Different Heat Flux Steps

Table 3-4: Heat Flux Control Parameters Implemented in the Tests

| | Heat flux step | | |
|---|---|---|---|
| Test purpose | Magnitude (W/cm$^2$) | Duration (min.) | Data recording interval (s) |
| Initial evaluation | 25 to 100 | 3 to 5 | 3 |
| Investigation of highest ***h*** | 50 | 3 | 3 |
| Investigation of ***CHF*** | 10 to 100 | 1 to 2 | 1 to 3 |

## 3.6 Infrared Thermography

Infrared (IR) thermography was utilized in the current work as an alternative temperature measurement technique. Besides the embedded TCs in the heater wall, IR thermography allowed measuring temperatures at the thick film resistor surface, the outermost surface of the heater assembly. This helped validating critical temperature readings for a better performance comparison between various heaters.

IR thermography is known to be capable of providing practical and fast measurements. With careful attention to the required input parameters, such as object emissivity, distance, and ambient temperature, as well as atmospheric conditions, IR technique can also give very accurate results. Emissivity of the target object is particularly important since it depends on the surface characteristics and also changes with temperature. A two-step preparation was therefore conducted for effective use of IR thermography in this study. First, IR camera measurements were validated following a common procedure [25, 26], and then emissivity of the thick film resistor surface was determined at a range of temperatures. A rather basic setup, shown in Figure 3-23, was employed for these purposes. An Inframetrics PM290 ThermaCam model IR camera was placed directly across a copper test block that included a reference emitter with known emissivity (3M Scotch Super 88 Vinyl Tape), two thick film resistors, and five TCs. Resistors were soldered onto a central location in the front, while TCs were soldered onto front, back and top surfaces of the copper block, and onto each resistors to monitor the temperature uniformity. Copper block was brought to desired temperature levels via a heater base equipped with cartridge heaters and temperature controller. TC readings were constantly monitored and recorded through a DAQ system.

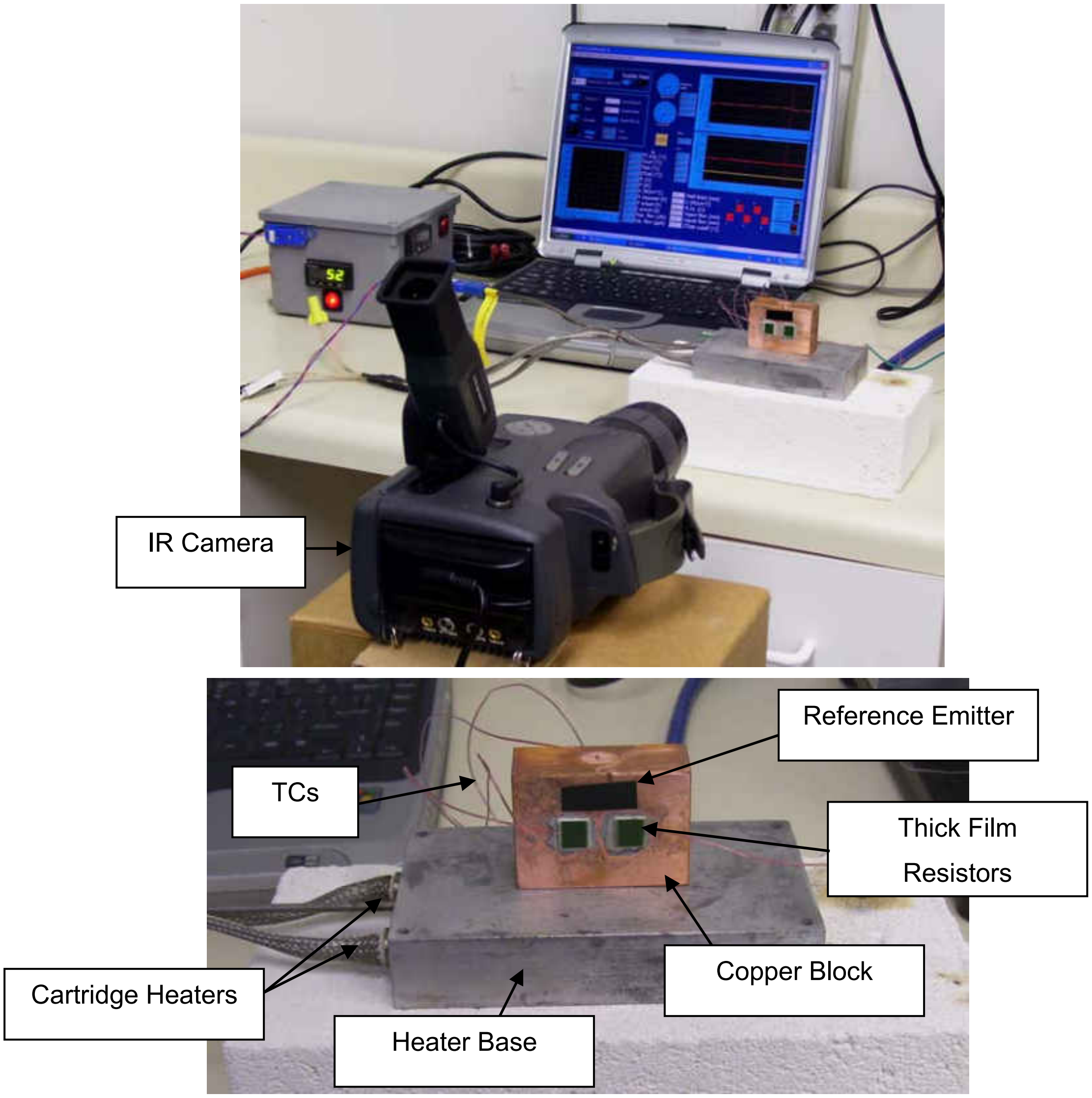

Figure 3-23: Test Setup for IR Camera Validation and Resistor Emissivity Measurement

### 3.6.1 IR Camera Measurement Validation

In order to validate the IR camera measurements, copper block was heated to 50 and 75 $^{o}$C, and time averaged TC readings at steady-state condition were compared to IR temperature readings on the reference emitter tape. This specific tape has an emissivity of 0.95 and is widely used in quick calibration tests. Figure 3-24 includes two sample IR images that were taken at the mentioned temperature levels. Indicated IR temperature readings represent the average temperature within the marked region on the tape. Comparison of these IR readings to corresponding averaged TC readings in Figure 3-25, reveals that the IR camera measurements are satisfactorily accurate.

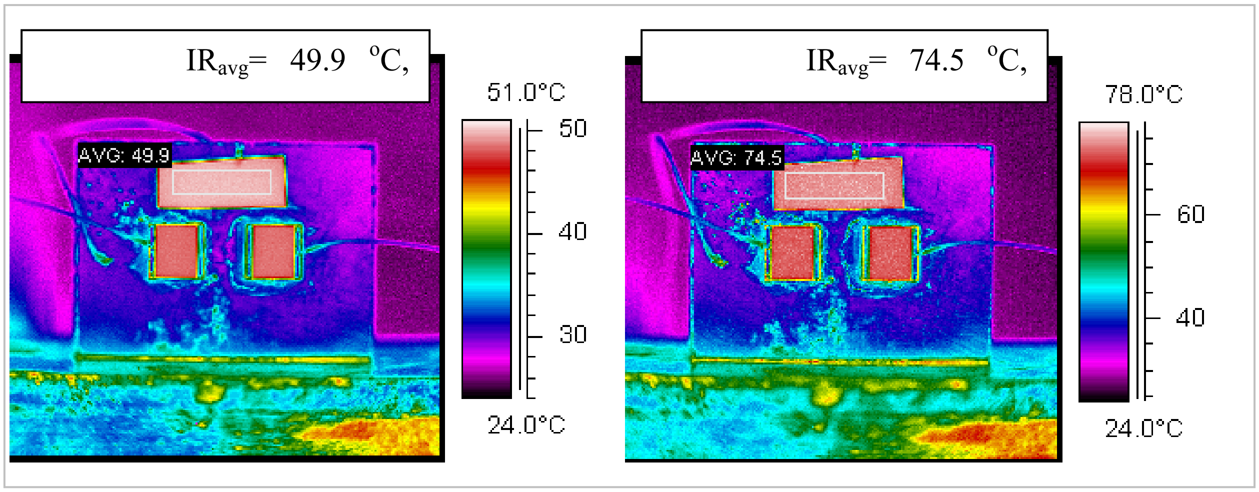

Figure 3-24: Sample Images from IR Camera Measurement Validation Tests

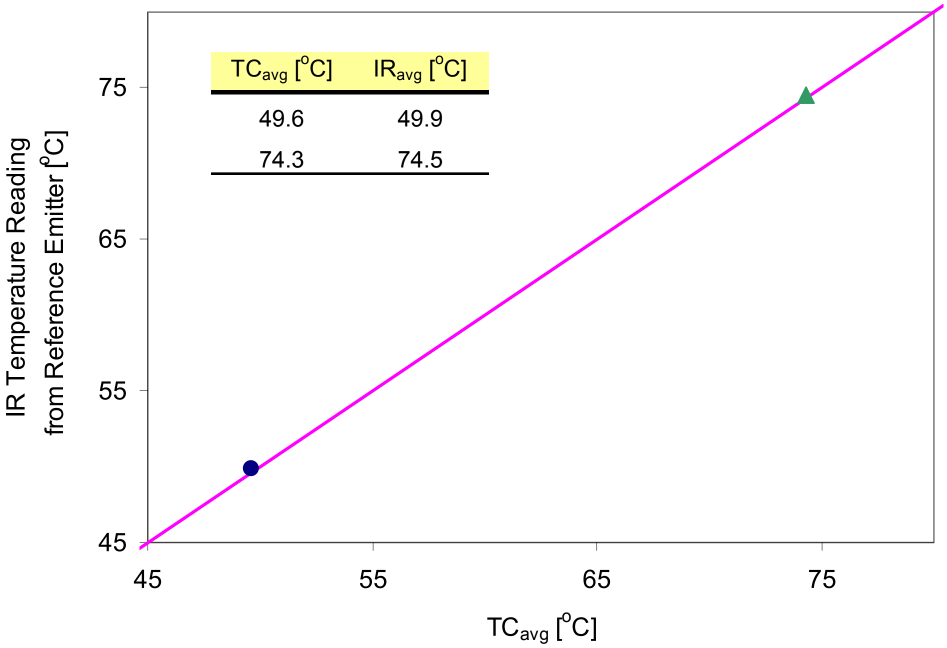

| $TC_{avg}$ [$^oC$] | $IR_{avg}$ [$^oC$] |
|---|---|
| 49.6 | 49.9 |
| 74.3 | 74.5 |

Figure 3-25: IR Camera Measurement Validation Tests

### 3.6.2 Resistor Emissivity Measurement

In emissivity measurements, the copper block was heated to temperatures between 50 to 150 $^oC$ with 25 $^oC$ increments, time averaged TC readings at steady-state condition were taken as basis, and then emissivity values for IR temperature readings on resistor surfaces were adjusted until finding matching temperatures. Figure 3-26 presents two sample IR images along with determined resistor emissivity of 0.90 and 0.81, for average TC readings of 49.6 and 99.7 $^oC$, respectively.

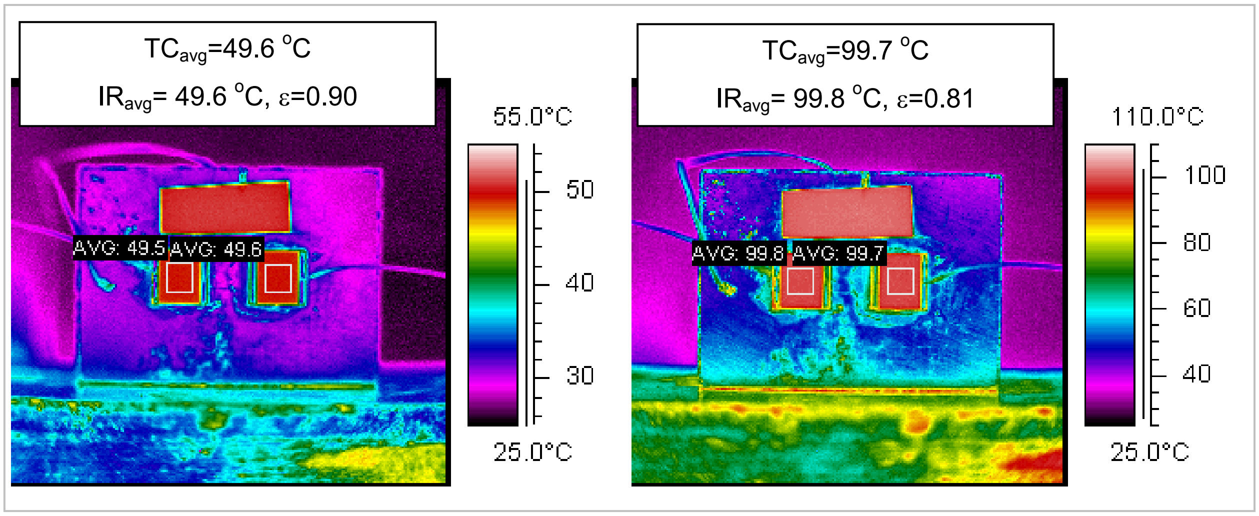

Figure 3-26: Sample Images from Resistor Emissivity Measurement Tests

The more complete trend, characterizing the change of emissivity as a function of temperature, is shown in Figure 3-27, where initial measured value of 0.90 at 50 $^{o}$C decreases down to 0.74 at 150 $^{o}$C. In the scope of this study, IR thermography was used to confirm heater temperatures at heat fluxes of ≥500 W/cm$^2$, with resistor temperatures of ≥100 $^{o}$C. Therefore, a constant emissivity value of 0.75 was adapted in all measurements.

In order to ensure consistent and accurate IR temperature readings that represent resistor temperature, $T_{res}$, the other important step is to define a proper area on target object for IR data averaging. Although the resistors used in this work had 1 cm$^2$ base area, actual heat generation took place in a smaller area between solder pads located on the sides. The IR data were therefore averaged over a 0.64 cm$^2$ selected surface area, obtained after trimming the base length and width for a certain amount, as illustrated in Figure 3-28.

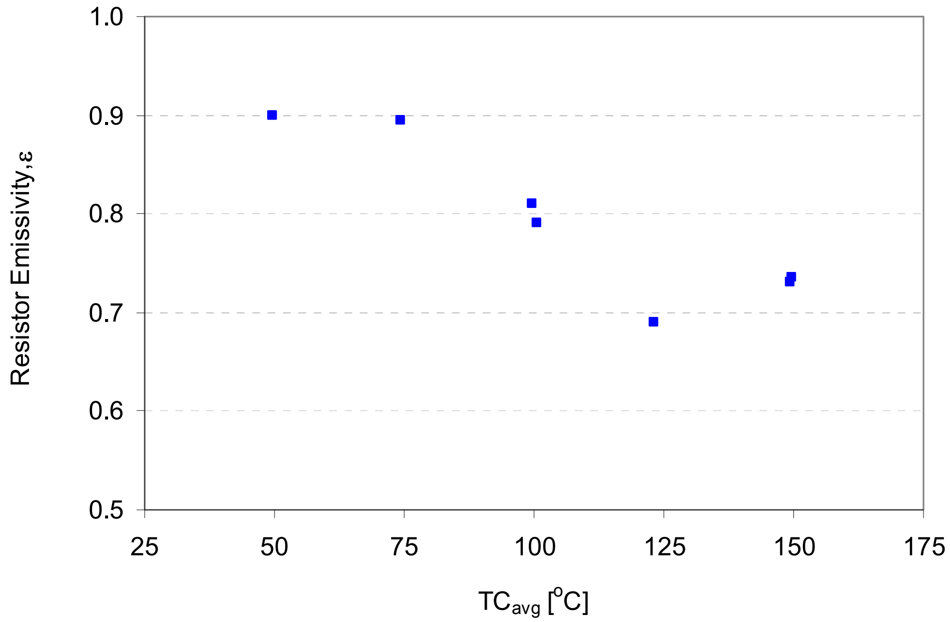

Figure 3-27: Resistor Emissivity Value as a Function of Temperature

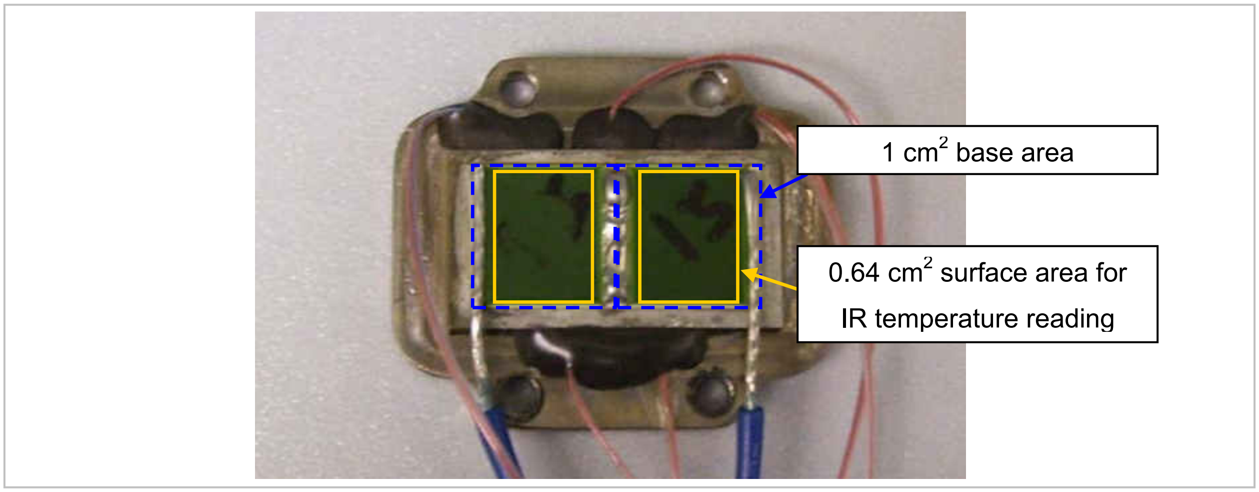

Figure 3-28: Selected Resistor Surface Area on a Heater for IR Temperature Readings

### 3.7 Uncertainty Analysis

Uncertainties were estimated mainly for heat flux and temperature measurements. Error involved in heat flux measurement (considering variations in voltage, current, and area) was ±2.3% at 500 W/cm$^2$. Error in temperature measurements from the embedded thermocouples in heater wall (considering thermocouple and data acquisition system specifications) was calculated to be ±1.0 $^{o}$C. Spray surface temperature had a slightly higher uncertainty at ±1.1 $^{o}$C. IR thermography based temperature readings are believed to have an uncertainty of ±0.75 $^{o}$C primarily due to manual area selections on resistor surfaces for data averaging. Heat transfer coefficients included ±5.5, 7.7 and 10.3% uncertainty at 500 W/cm$^2$ for the surfaces ***s***, ***mi*** and ***mp***, respectively. Heat loss from thick film resistors to the surroundings was negligibly small (<1 W) based on calculations considering natural convection and black body radiation from 100 $^{o}$C heater surface to 20 $^{o}$C ambient air.

# CHAPTER 4: INVESTIGATION OF ENHANCED SURFACES FOR HIGHEST HEAT TRANSFER COEFFICIENT

This chapter reports and discusses the results of the first stage of current study regarding the investigation of enhanced surfaces for the highest heat transfer coefficient at heat fluxes of up to 500 W/cm$^2$. First section addresses the initial testing of selected enhanced surfaces, and the following four sections focus on results and heat transfer enhancement mechanisms of reference, and micro-, macro- and multi-scale structured surfaces in order.

## 4.1 Initial Testing with Selected Enhanced Surfaces: Performance Enhancement and Hysteresis Effect

Preliminary spray cooling data were obtained using type ***#*** heaters featuring microstructured surfaces, surfaces ***mi*** and ***mp***, and a machine finished-smooth surface, surface ***s*** that represented the reference case. The purpose of initial testing was to quickly evaluate the performance of these surfaces without focusing on optimization of structural parameters. Surfaces ***mi*** and ***mp*** had approximate roughness levels of fine and medium, corresponding to their respective roughness ranges.

Data from these described surfaces are presented in Figure 4-1 where heat flux was first gradually increased in steps of 100 W/cm$^2$ every five minutes from 0 to 500 W/cm$^2$ (heating-up mode) and then decreased in a similar manner back to 0 W/cm$^2$ (cooling-down mode). Cooling curves with time-averaged temperatures are plotted in Figure 4-2 for an easier performance comparison. As shown, both microstructured surfaces provided considerable performance enhancement over the smooth surface while the surface ***mp*** was superior to the surface ***mi***. Steep changes in the cooling curves of both microstructured surfaces indicate contribution of phase-change mechanism into overall heat transfer.

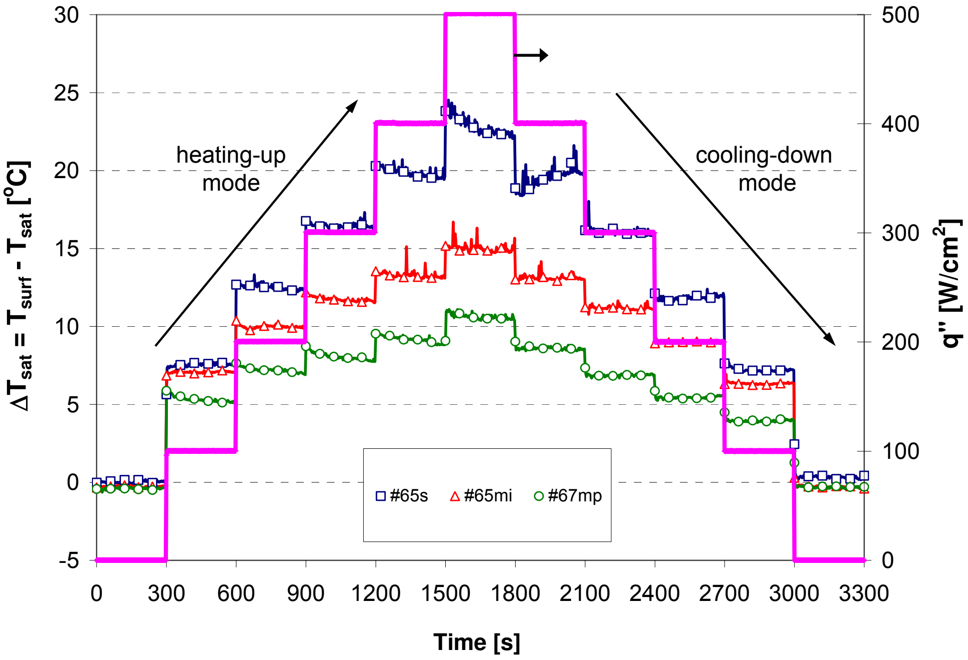

Figure 4-1: Heat Transfer Performance of the Surfaces ***mi***, ***mp***, and ***s*** as Heat Flux Changes in Steps of 100 W/cm$^2$ Every Five Minutes from 0 to 500 Then Back to 0 W/cm$^2$ in Heating-up and Cooling-down Mode

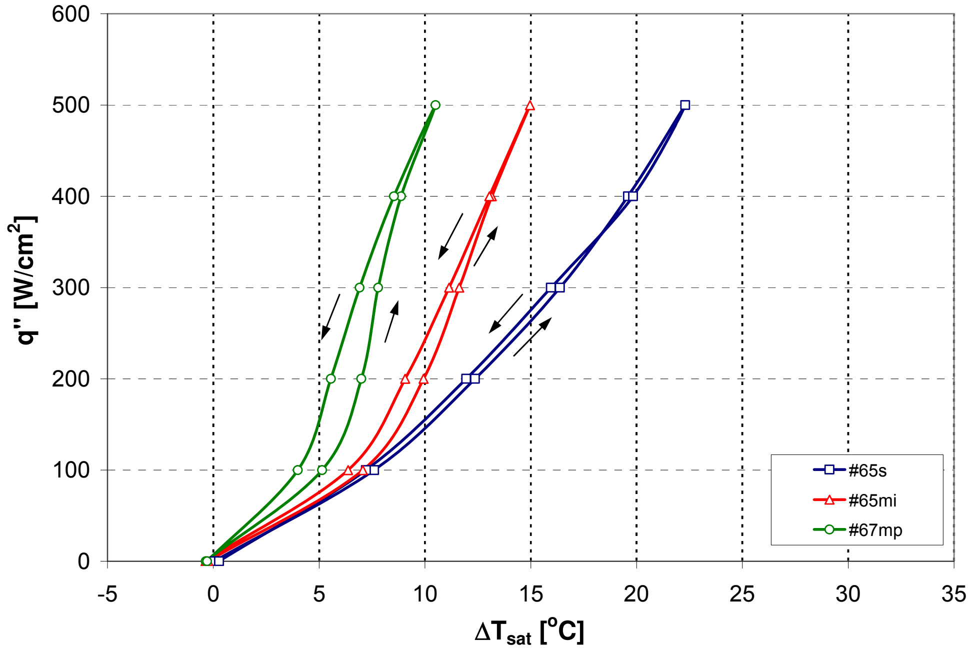

Figure 4-2: Heat Transfer Performance of the Surfaces ***mi***, ***mp***, and ***s*** in Heating-up and Cooling-down Modes

Based on the outlined phase-change heat transfer mechanisms in Section 2.1, namely, free surface evaporation, boiling through surface and secondary nucleation, and contact line heat transfer, current results can be examined. It is obvious that all three surfaces were subjected to similar free surface evaporation and secondary nucleation mechanisms since the spray conditions were same throughout the tests. In addition to these mechanisms, substantial heat transfer enhancement provided by the microstructured surfaces can be attributed to the increase in surface area and stronger contribution of other phase-change mechanisms. Both microstructured surfaces provided a spectrum of cavity sizes, and thus had the potential to generate additional surface nucleation sites, and increase three-phase contact line length density. Better performance of the surface ***mp***, compared to the surface ***mi***, can be explained with its complex structure that offers more surface area and reentrant cavities.

For a common way of performance comparison, the heat transfer coefficient $h$, defined as

$$h = \frac{q''}{\Delta T_{sat}} \tag{4}$$

was calculated, and plotted as a function of heat flux for all test surfaces in Figure 4-3. As seen, heat transfer coefficient continuously increased as heat flux increased, and reached 219,000, 333,000, and 470,000 W/m$^2$°C for the surfaces ***s***, ***mi***, and ***mp***, respectively, at 500 W/cm$^2$. An enhancement factor $EF_h$, defined as

$$EF_h = \frac{h}{h_{ref}} \tag{5}$$

was implemented to normalize the heat transfer coefficients of enhanced surfaces over that of the reference smooth surface. Data in Figure 4-4 shows 1.52X (52%) and 2.15X (115%) improvement for the surfaces ***mi*** and ***mp***, respectively, over the surface ***s*** at 500 W/cm$^2$.

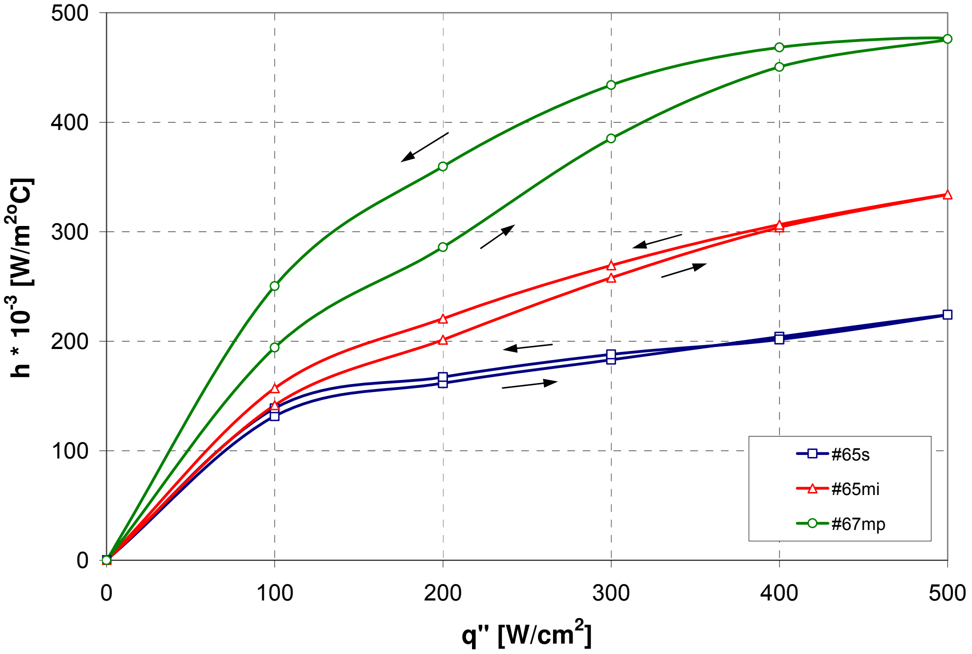

Figure 4-3: Heat Transfer Coefficients as a Function of Heat Flux for the Surfaces ***mi***, ***mp***, and ***s*** in Heating-up and Cooling-down Modes

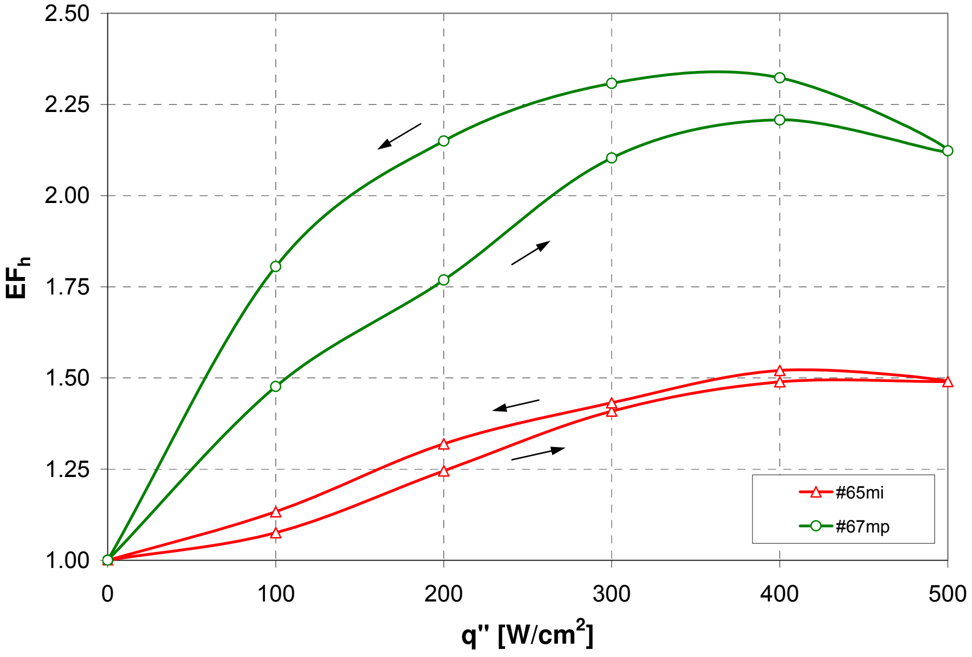

Figure 4-4: Performance Enhancement Factor as a Function of Heat Flux for the Surfaces ***mi***, ***mp***, and ***s*** in Heating-up and Cooling-down Modes

Besides the significant heat transfer enhancement, microstructured surfaces also revealed a hysteresis phenomenon when cooling curves in the heating-up and cooling-down modes are compared in Figure 4-2. Although the smooth surface gives nearly identical cooling curves, microstructured surfaces experience lower surface superheats in the cooling-down mode at a given heat flux. This deviation in superheats is more pronounced for the surface ***mp***, implying hysteresis dependence on the surface roughness level.

None of the previous spray cooling research on surface effects [13-20] reported a hysteresis phenomena which results in lower surface superheats in cooling-down mode, compared to heating-up mode, at a given heat flux. Many nucleate pool boiling literature however addressed hysteresis issue especially with highly wetting liquids such as R-113 and FC-72.

Bergles and Chyu [27] and Marto and Lepere [28] were among the first to mention boiling hysteresis known as “temperature excursion” or “temperature overshoot” hysteresis which manifests itself with large temperature drops on the surface when nucleation starts.

Shi et al. [29] later observed another type of boiling hysteresis and described it as “temperature deviation” hysteresis. This hysteresis caused temperature deviation between the cooling curves in the heating-up and cooling-down modes. Lower surface superheats occurred in the cooling-down mode of fully developed nucleate boiling regime, and distinguished itself from the temperature overshoot hysteresis that occurs at boiling incipience.

Several mechanisms can be identified in explaining boiling hysteresis. One of these, recognized since the early works, was “vapor gathering” where nucleation site, initially flooded with highly wetting fluid, requires a large surface superheat for the first bubble departure, but retains enough vapor afterwards enabling boiling at much lower surface superheat. In other mechanisms, early growing bubbles help neighboring cavities, which retained less or no residual gas, activate at lower surface superheats by “vapor propagation” (for non-wetting fluids) and “vapor covering” (for wetting fluids). Shi et al. concluded that vapor gathering, vapor propagation and covering are the main mechanisms of temperature overshoot hysteresis while further vapor propagation causes temperature deviation hysteresis.

Hwang and Kaviany [30] on the other hand, used microporous surfaces in their boiling tests and observed temperature deviation hysteresis with an opposite trend where cooling-down mode resulted in higher surface superheats, compared to heating-up mode, at a given heat flux. They thought the hysteresis was caused by the trapped vapor within the porous layer, which decreases the effective conductivity.

In order to gain a better understating on spray cooling hysteresis effect, additional experiments were decided to conduct with the surface ***mp***. First set of experiments considered whether the initially observed hysteresis effect (e.g., temperature deviation between heating-up and cooling-down curves) changes with varying heat flux conditions. In these tests, heat flux was first ramped up from 0 to 500 W/cm$^2$. In the following test segments, heat flux was ramped down to gradually decreasing values and then ramped up again through several cycles to observe how hysteresis effect changes. As plotted in Figure 4-5 along with corresponding surface superheat, heat flux was changed from 0 to 500, then back to 150, then to 300, back to 100, then to 200, back to 50 W/cm$^2$, and so on. All changes in heat fluxes, up or down, were in steps of 50 W/cm$^2$ (25 W/cm$^2$ for q”<100 W/cm$^2$) every three minutes. Change in hysteresis through the initial heating-up mode, and the following test segments can easily be seen when this data is plotted in the form of cooling curves in Figure 4-6. Results show that once the heater is brought to a high heat flux (and high superheat), superheat will track the same cooling curve on the left with decreasing (as low as 25 W/cm$^2$ for the present study) or increasing heat fluxes. However, if heat flux is reduced all the way down to zero, then superheat will follow the cooling curve on the right for heating-up mode as can be closely seen in Figure 4-7. Data therefore suggest that once the three-phase contact line is established on the surface at a certain heat flux, microstructures are able to retain vapor effectively in the cavities and heater can provide a consistent cooling curve and hysteresis effect at lower heat fluxes. At zero heat flux condition, microstructures cannot support the retained vapor anymore and lose the contact line length. A consecutive heat flux increase at this state is no different than initial heating-up mode where contact line is established gradually.

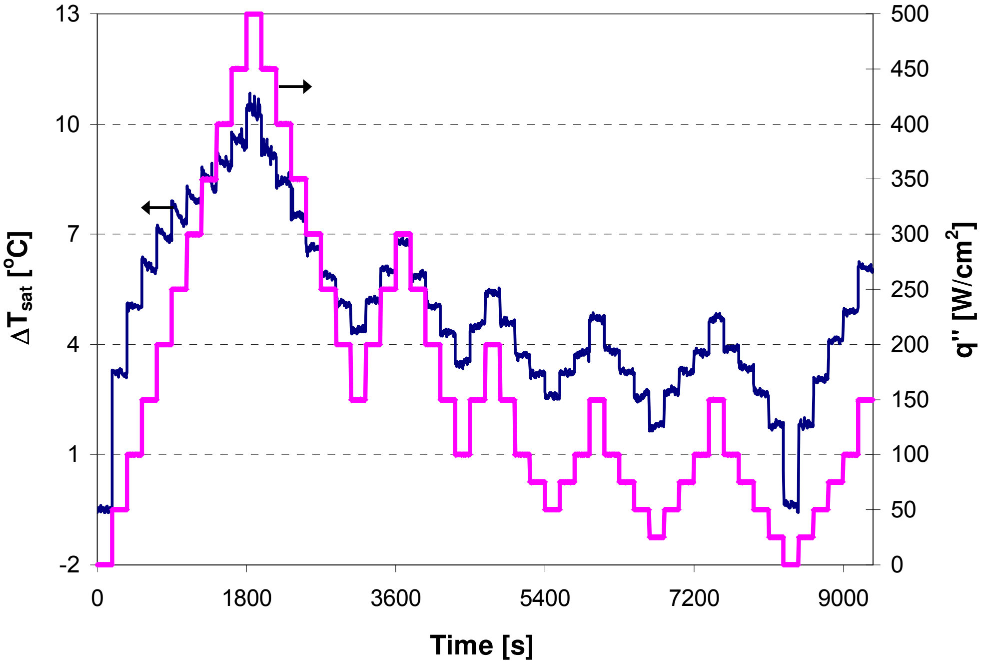

Figure 4-5: Heat Transfer Performance of the Surface ***mp*** as Heat Flux Changes in Steps of 25-50 W/cm$^2$ Every Three Minutes in Heating-up and Cooling-down Modes

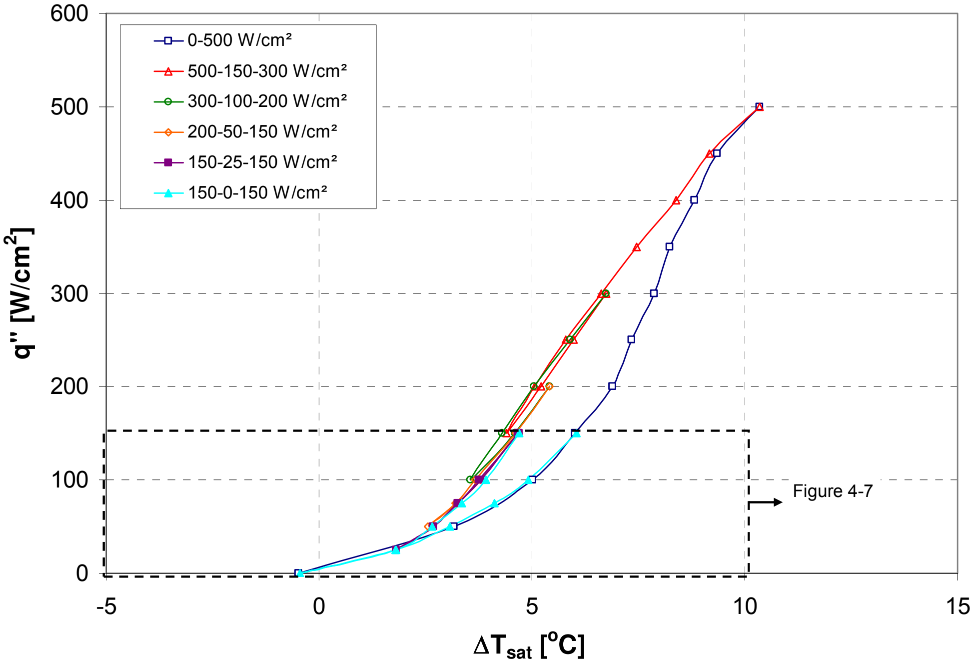

Figure 4-6: Heat Transfer Performance of the Surface ***mp*** in Heating-up and Cooling-down Modes

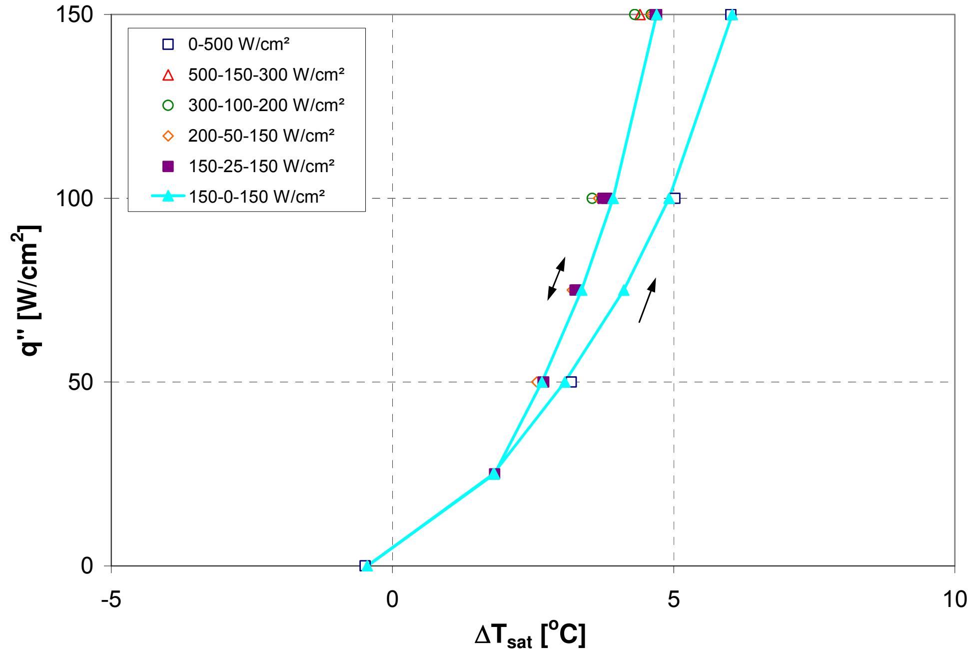

Figure 4-7: Heat Transfer Performance of the Surface ***mp*** in Heating-up and Cooling-down Modes (A Close-up View of Figure 4-6)

Second set of experiments addressed how hysteresis effect relates to thermal history of the heater. In each segment of these tests, heat flux was increased up to a maximum value and then decreased down to 0 W/cm$^2$ each time to observe the amount of hysteresis. As seen in Figure 4-8 along with corresponding surface superheat, heat flux was changed from 0 to 100, then back to 0, then to 200, back to 0, then to 300, back to 0 W/cm$^2$, and so on. All changes in heat fluxes, up or down, were in steps of 100 W/cm$^2$ every three minutes. Amount of hysteresis occurred in each test segment can be better examined when cooling curves are compared in Figure 4-9. Data here, and further in the close-up view in Figure 4-10, clearly indicate the trend where amount of hysteresis increases as maximum heat flux increases from 100 to 500 W/cm$^2$. This observation suggests that as heat flux and surface temperature of the heater increase, contact line length on the microstructured surface increases. If the surface can maintain some of the established contact line, as in the case of microstructured surfaces in the present study, this results in a larger hysteresis or lower superheat later at lower heat fluxes.

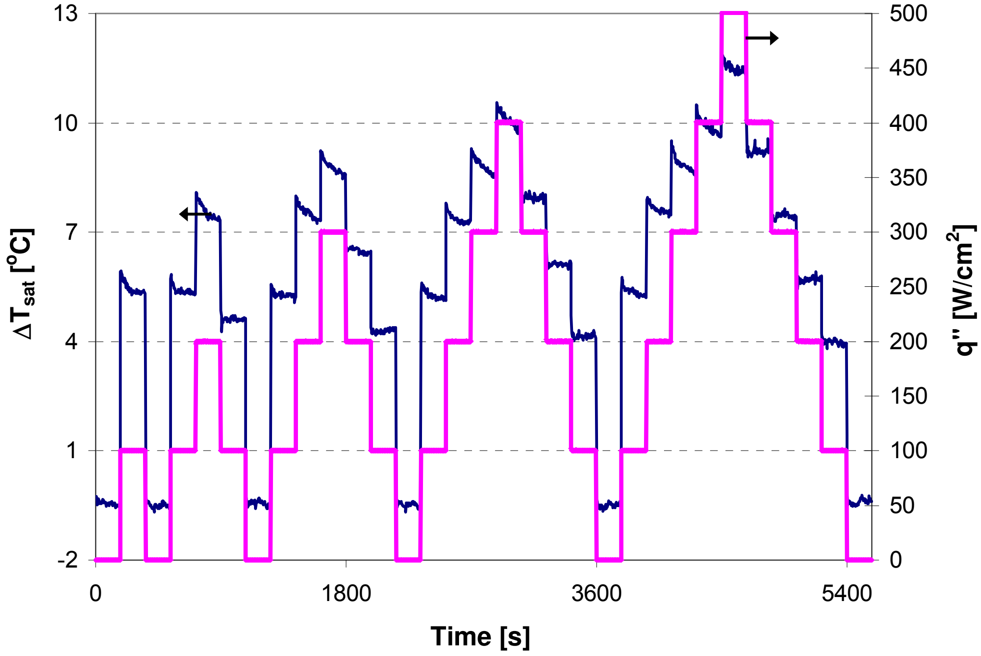

Figure 4-8: Heat Transfer Performance of the Surface ***mp*** as Heat Flux Changes in Steps of 100 W/cm$^2$ Every Three Minutes in Heating-up and Cooling-down Modes

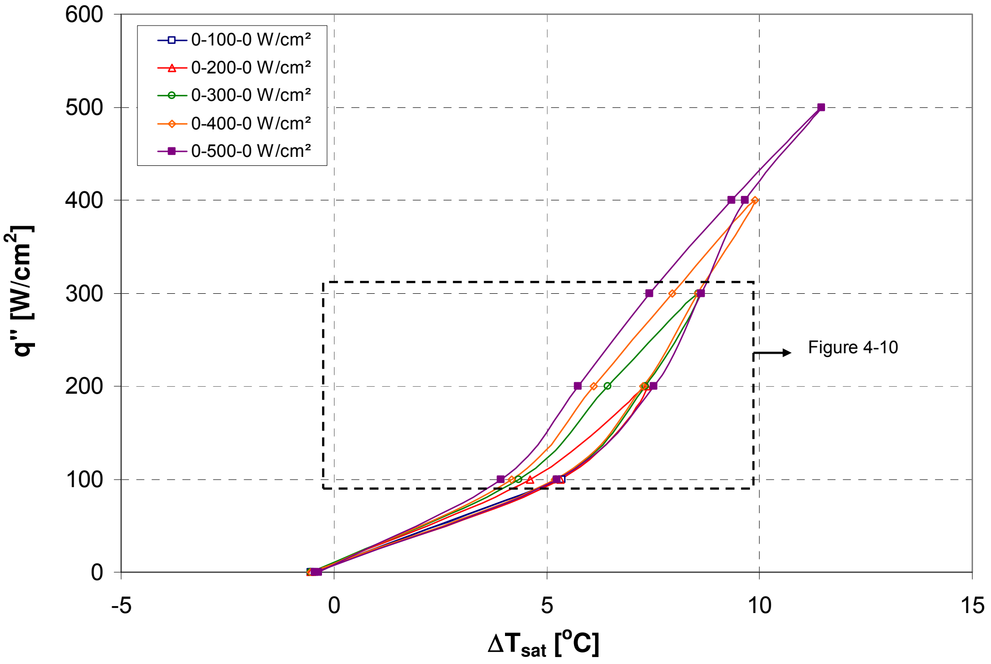

Figure 4-9: Heat Transfer Performance of the Surface ***mp*** in Heating-up and Cooling-down Modes

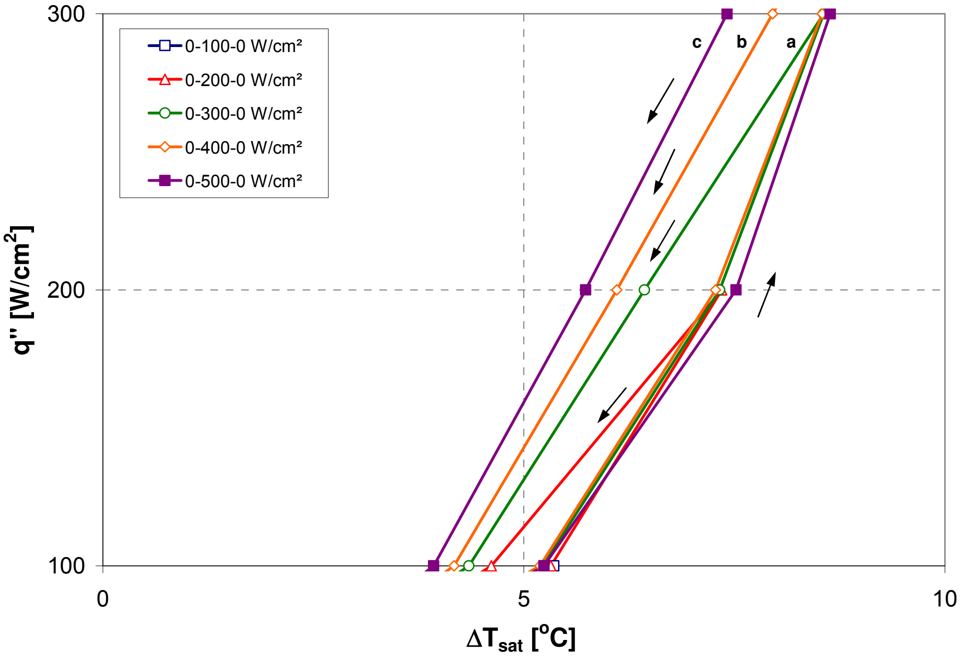

Figure 4-10: Heat Transfer Performance of the Surface ***mp*** in Heating-up and Cooling-down Modes (A Close-up View of Figure 4-9)

Figure 4-11 reflects the change in heat transfer due to hysteresis effect quantitatively. Utilizing data from the second set of experiments, heat transfer coefficients in cooling-down mode can be normalized based on those in heating-up mode. For instance, when change in heat transfer at 300 W/cm$^2$ is considered using normalized heat transfer coefficients of $h_c/h_a$, $h_b/h_a$ and $h_a/h_a$ in Figure 4-11, corresponding to points c, b and a in Figure 4-10, the heat transfer coefficient improves 1.08X (8%) and 1.16X (16%) if the surface is first exposed to 400 and 500 W/cm$^2$, respectively, and then brought back to 300 W/cm$^2$. Similarly, at 100 W/cm$^2$, heat transfer coefficient can be increased by up to 1.36X (36%) if the surface is previously exposed to 500 W/cm$^2$.

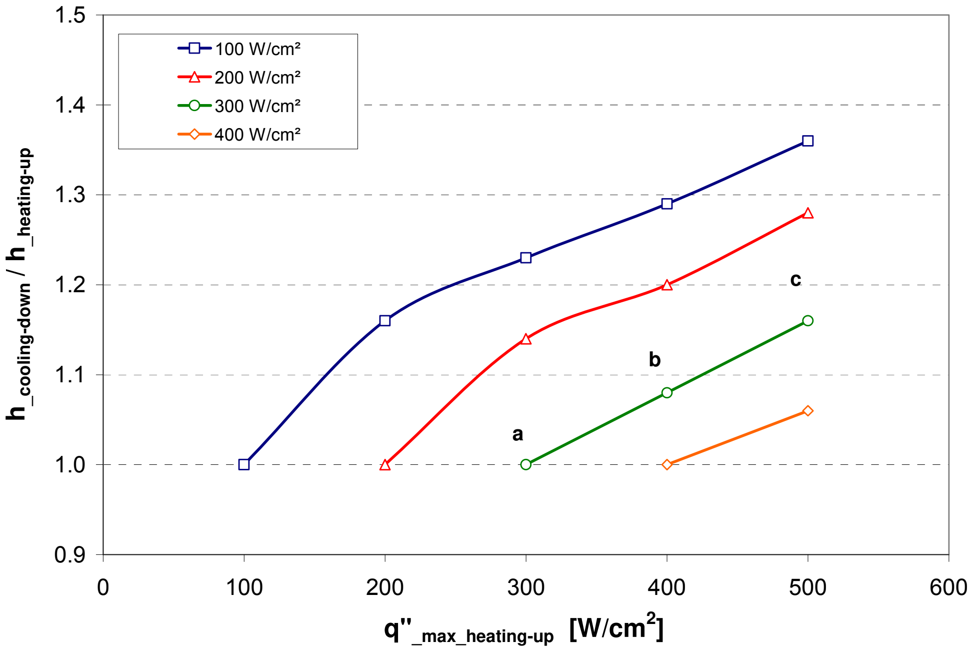

Figure 4-11: Normalized Heat Transfer Coefficients at Constant Heat Fluxes as a Function of Maximum Heat Flux in Heating-up Mode Indicating Quantitative Change in Heat Transfer due to Hysteresis Effect

Larger hysteresis observed with the surface ***mp*** in Figure 4-2 can also be explained based on the findings from the hysteresis related testing with this surface. Having more surface area and re-entrant cavities, the surface ***mp*** has the potential to capture and retain more vapor, and establish higher three-phase contact line density compared to the surface ***mi***. Therefore for the surface ***mp***, difference between the contact line lengths in the heating-up and cooling-down modes is larger, resulting in larger hysteresis.

## 4.2 Reference Surfaces

Upon completion of the initial testing of type ***#*** heaters with the selected enhanced surfaces, comprehensive investigation of enhanced surfaces for the highest heat transfer coefficient continued with type ***A*** heaters. For this part of study, the surface ***s*** was considered as "reference" as well, in the evaluation of all other enhanced surfaces.

### 4.2.1 Results with Reference Surfaces

Since the performance of reference surface is critical in comparisons, five heaters were selected and tested at least twice to obtain a pool of data. As shown in Figure 4-12, these heaters provided a consistent performance and their surface superheats varied approximately ± 1 $^{o}$C.

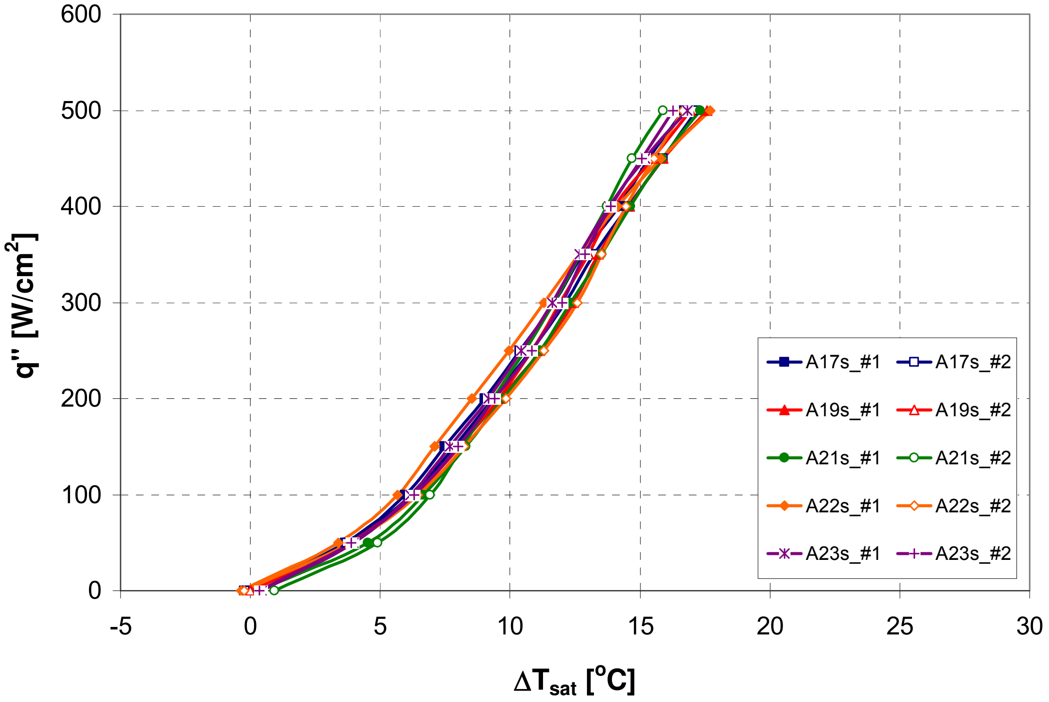

Figure 4-12: Heat Transfer Performance of the Surface ***s*** from Five Different Heaters

The averaged data from ten tests were then plotted as the reference cooling curve for type ***A*** heaters, and called as A-Ref in Figure 4-13. Two straight lines marked on the cooling curve represent two of the heat transfer regimes explained earlier, single phase forced convection, region I, and two phase boiling/evaporation, region II. Since heat flux was limited to 500 W/cm$^2$ at this stage of the study, cooling curves do not reach the two phase-to-CHF transition regime, or region III, yet.

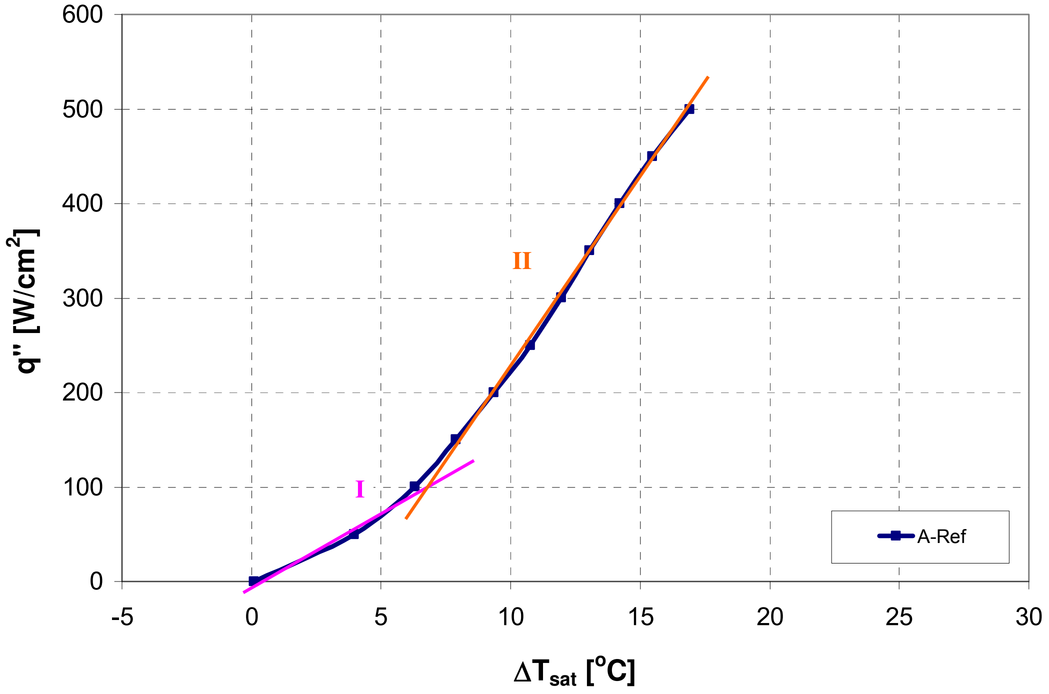

Figure 4-13: Reference Cooling Curve for Type ***A*** Heaters Representing Average Heat Transfer Performance of the Surface ***s*** from Five Different Heaters

As detailed in Section 3.6, IR thermography was utilized to independently validate temperature readings, and better compare performance of enhanced surfaces. This approach required establishing a resistor temperature for reference surfaces that was normalized for saturation temperature. Therefore, all available IR temperature readings from the reference surface tests were collected and processed. Figure 4-14 includes some sample IR images from the reference surface tests.

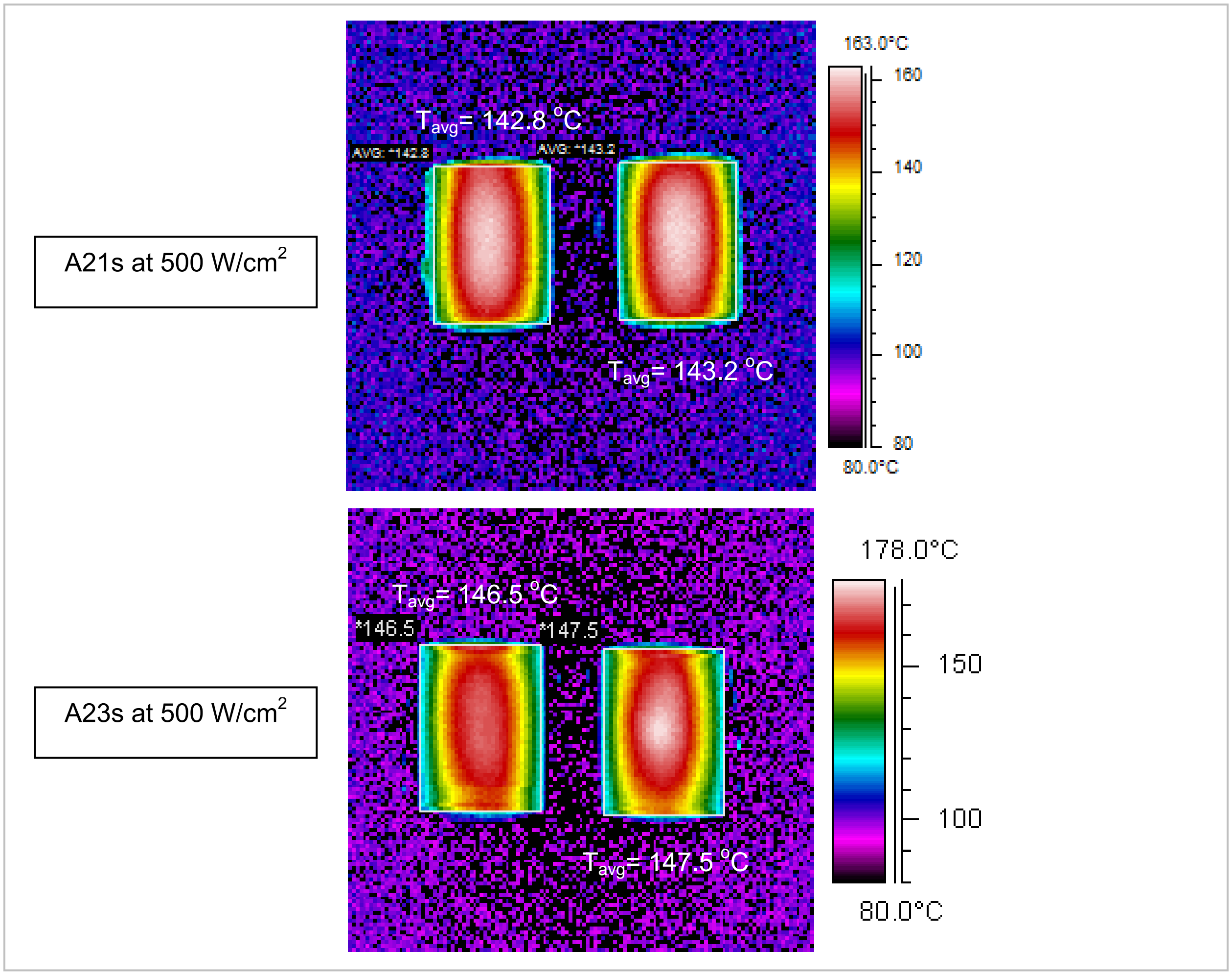

Figure 4-14: Sample IR Images Showing Resistor Temperatures during Reference Surface Tests

Figure 4-15 summarizes the normalized resistor temperature, $T_{res}$-$T_{sat}$, data from the reference surfaces at 500 W/cm$^2$. These temperatures lie within a ±1.5 $^{o}$C range resulting an average value of 136.3 $^{o}$C as indicated. Thus, these data independently confirm that the five different reference surfaces perform very consistently, and also suggest that the IR thermography can be a valuable tool to obtain normalized resistor temperatures for verifying heater performances with various enhanced surfaces.

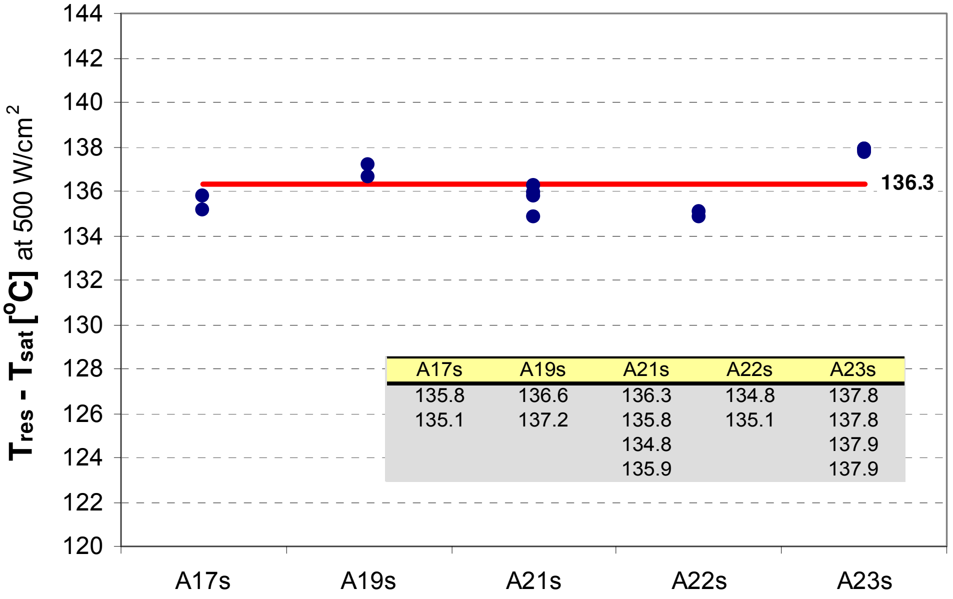

| A17s | A19s | A21s | A22s | A23s |
|---|---|---|---|---|
| 135.8 | 136.6 | 136.3 | 134.8 | 137.8 |
| 135.1 | 137.2 | 135.8 | 135.1 | 137.8 |
|  |  | 134.8 |  | 137.9 |
|  |  | 135.9 |  | 137.9 |

Figure 4-15: IR Thermography Based Normalized Resistor Temperatures for the Surface *s* from Five Different Heaters

## 4.3 Microstructured Surfaces

With the baseline performance established for type ***A*** heaters, testing of microstructured surfaces was started next. This group of heaters featured the surfaces ***s**** (polished), ***mi(-f,-m,-c)***, and ***mp(-f,-m,-c)*** in search of higher heat transfer coefficients.

### 4.3.1 Results with Microstructured Surfaces

As mentioned earlier, the surface ***s*** (machine finished-smooth) was the reference surface for type ***A*** heaters. Any extra treatment that changes original surface condition was considered as surface enhancement. Pais et al. [13] reported superior heat transfer for ultra-polished surface over smooth surface, with approximate $R_a$ values of 0.1 and 1 μm, respectively, and attributed the improvement to favorable free surface evaporation due to a thinner liquid film that ultra-polished surface might have. Therefore, one of the heaters with the surface ***s*** (***A23s***) was selected, and its surface condition was modified to investigate the performance of polished surface.

Data from the surface ***s**** are plotted in Figure 4-16, along with those from the surface ***s***. When the cooling curves are compared, it can be noticed that the one for the surface ***s**** has a constant slope throughout the two-phase regime, while the surface ***s*** experiences a slight slope increase at heat fluxes >300 W/cm$^2$. IR thermography based normalized resistor temperatures for the surface ***s**** are given in Figure 4-17. In addition to the average reference surface data (A-Ref), the surface ***s*** data from heater ***A23s*** are also included in the plot to indicate the difference more accurately. Data therefore suggest that the polished surface does not provide any heat transfer enhancement over the smooth surface, and actually its performance might even tend to slightly deteriorate.

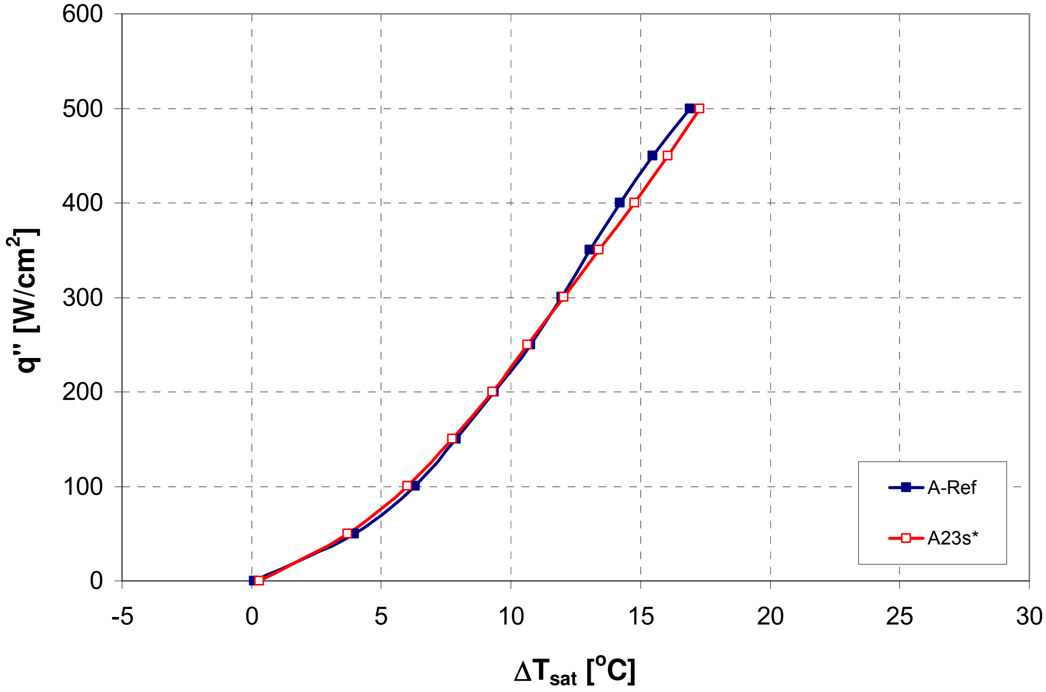

Figure 4-16: Heat Transfer Performance of the Surface *s**

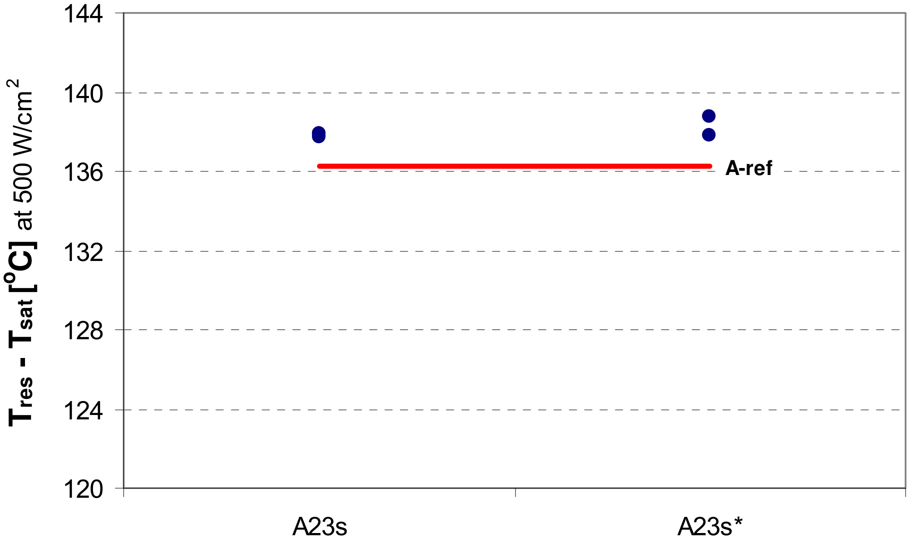

Figure 4-17: IR Thermography Based Normalized Resistor Temperatures for the Surfaces *s* and *s**

Testing of the surface ***mi*** aimed to evaluate the effect of micro scale surface indentations on the heat transfer enhancement. A range of roughness level, referred as fine, medium and coarse, was generated sequentially on the same heater, ***A23mi(-f,-m,-c)***. Data in Figure 4-18 clearly show that the surfaces ***mi(-f,-m,-c)*** provide a significant improvement over the surface ***s***. Although the surfaces ***mi(-f,-m,-c)*** resulted in nearly the same surface superheat value of 9 $^{o}$C at 500 W/cm$^2$, examination of the cooling curves at lower heat fluxes indicates that roughness level still have an effect on the performance, and lower roughness level helps reducing superheat. Normalized resistor temperatures in Figure 4-19 further illustrates the nearly identical performance of the surfaces ***mi(-f,-m,-c)*** at 500 W/cm$^2$.

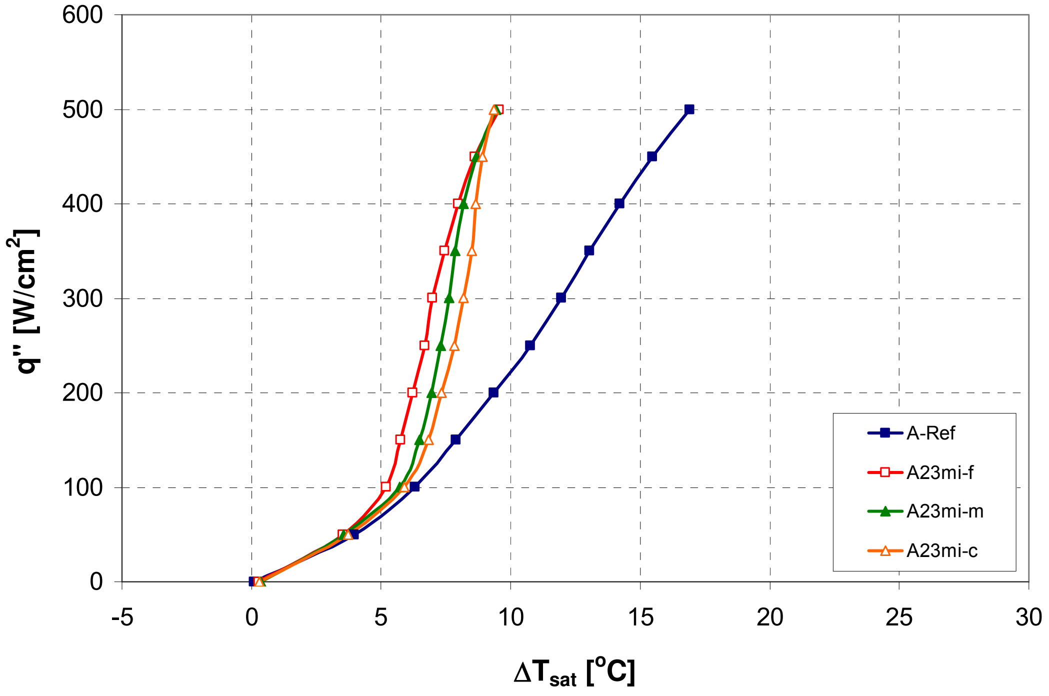

Figure 4-18: Heat Transfer Performance of the Surfaces ***mi(-f,-m,-c)***

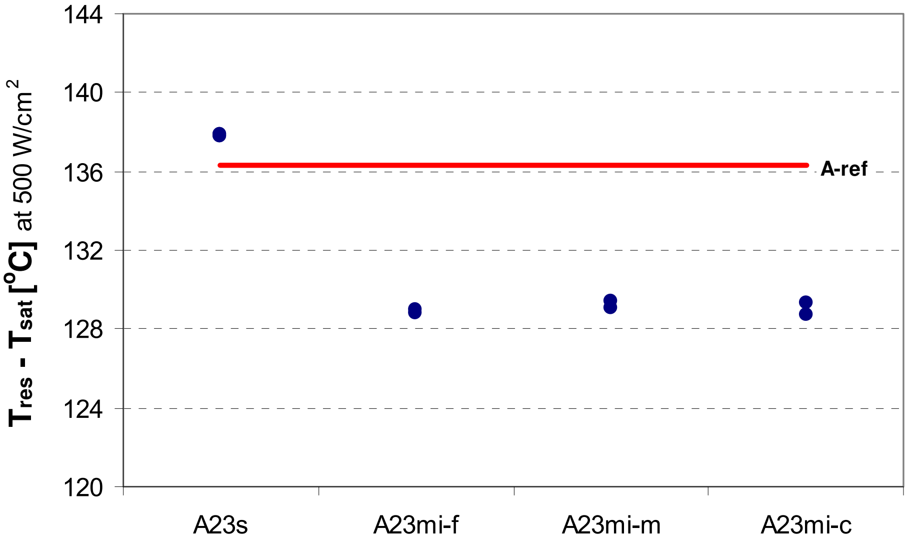

Figure 4-19: IR Thermography Based Normalized Resistor Temperatures for the Surfaces ***mi(-f,-m,-c)***

The surface ***mp*** was another type of microstructured surface featuring protrusions, and its heat transfer enhancement was also evaluated for a range of roughness level, referred as fine, medium, and coarse. Data in Figure 4-20 show a substantial enhancement for the surfaces ***mp(-f,-m,-c)*** over the surface ***s***, resulting in a surface superheat of 9.5 to 10.5 $^{o}$C at 500 W/cm$^2$. Cooling curves also provide some insights into the heat transfer characteristics of the surface ***mp***. First, it can be noticed that the surface ***mp*** compared to the surface ***mi*** transition to two-phase regime earlier starting at around 50 W/cm$^2$. Up to 300 W/cm$^2$ heat flux, there is a clear distinction between the three surfaces, where the surface ***mp-c*** performs best, followed by the surface ***mp-m*** and then the surface ***mp-f***. At higher heat fluxes, >300 W/cm$^2$, however, all curves merge together emphasizing a similar cooling performance. Figure 4-21 includes normalized resistor temperatures at 500 W/cm$^2$ and confirms the performance of the surface ***mp(-f,-m,-c)***.

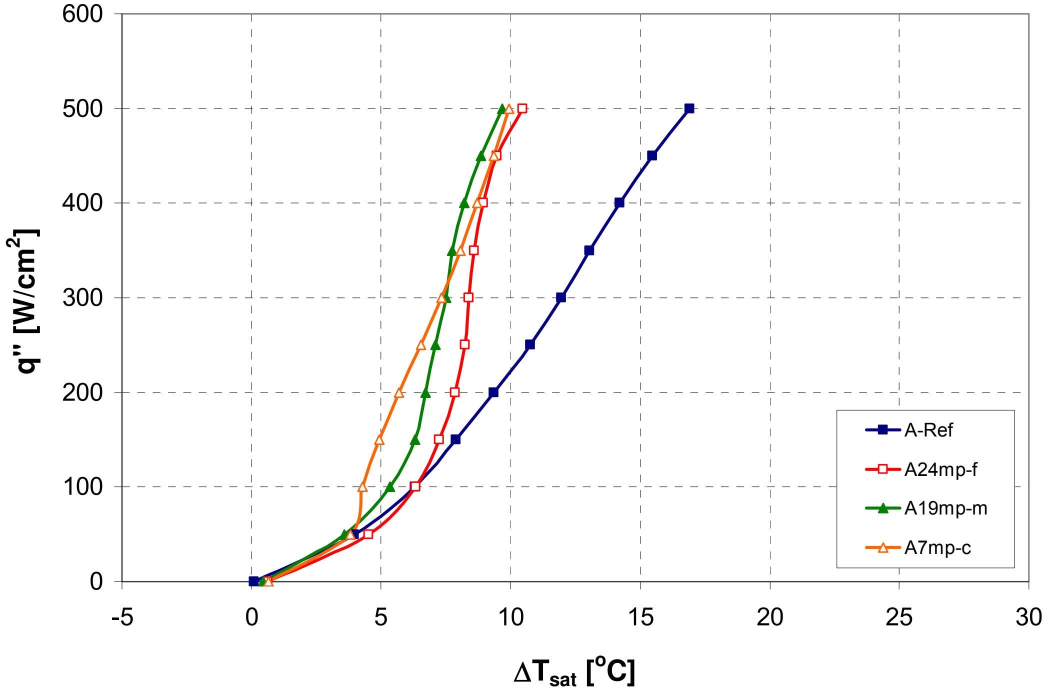

Figure 4-20: Heat Transfer Performance of the Surfaces ***mp(-f,-m,-c)***

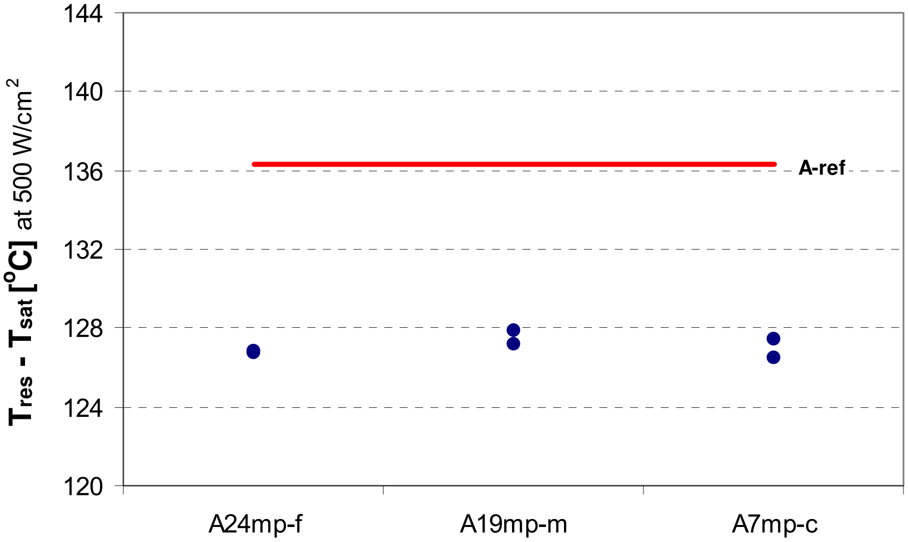

Figure 4-21: IR Thermography Based Normalized Resistor Temperatures for the Surfaces ***mp(-f,-m,-c)***

The performance comparison of all microstructured surfaces in terms of the heat transfer coefficient at heat fluxes of 0 to 500 W/cm$^2$ is provided in Figure 4-22. As shown, all microstructured surfaces, except the surface ***s****, attained higher heat transfer coefficients compared to the surface ***s***. At heat fluxes of up to 250 W/cm$^2$, the surface ***mp-c*** performed the best. At higher heat fluxes however, performance of the surfaces ***mi*** and ***mp*** with various roughness levels approached together. It should be noted that based on these results, performance of the type ***A*** heaters differed from the type **#** heaters tested initially, and implied the effect of surface material.

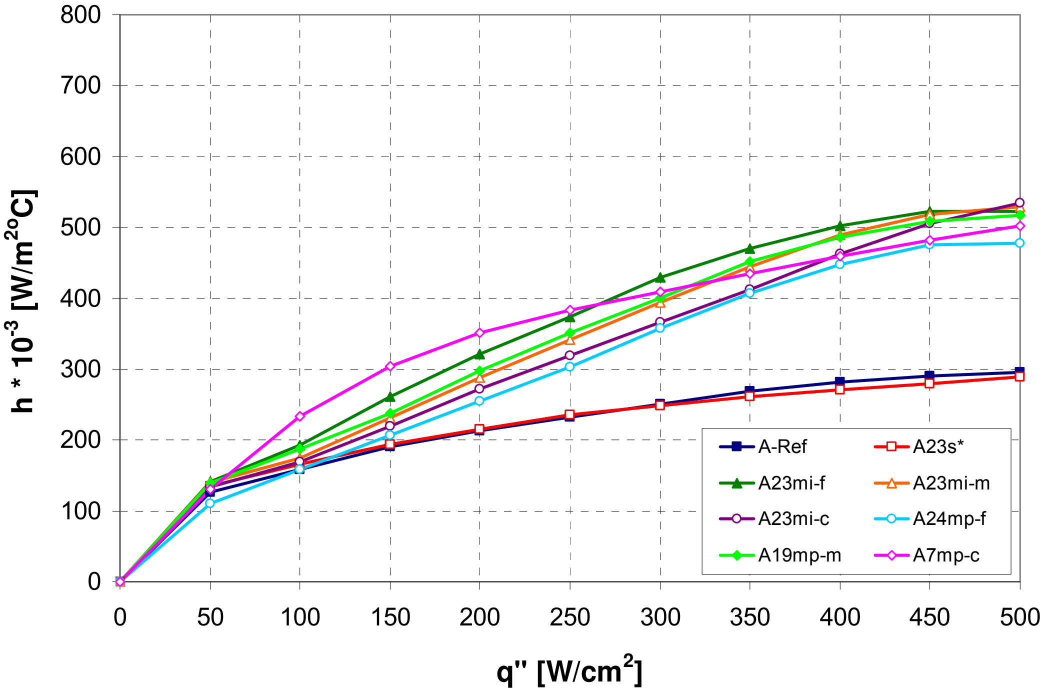

Figure 4-22: Performance Comparison of All Microstructured Surfaces Based on Heat Transfer Coefficient at Heat Fluxes of Up to 500 W/cm$^2$

A side by side performance comparison of all microstructured surfaces at heat flux of 500 W/cm$^2$ is presented in Figure 4-23. The highest heat transfer coefficient of 534,000 W/m$^{2o}$C was achieved by the surface ***mi-c***, providing 81% enhancement over the reference surface ***s***.

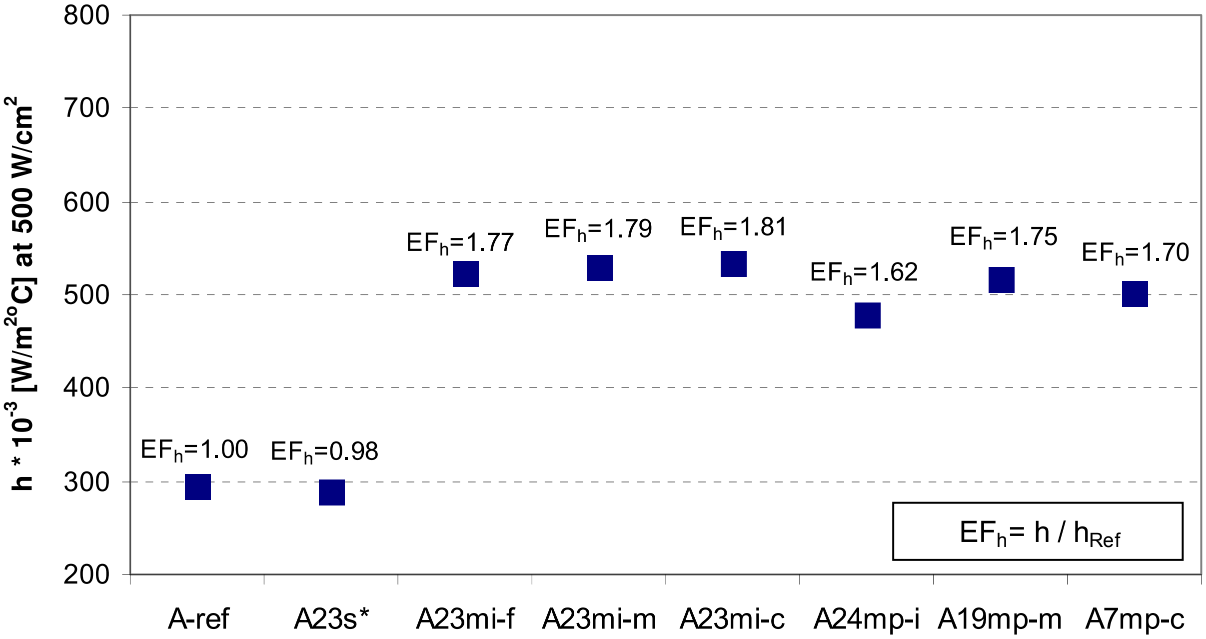

Figure 4-23: Performance Comparison of All Microstructured Surfaces Based on Heat Transfer Coefficient at Heat Flux of 500 W/cm$^2$

### 4.3.2 Heat Transfer Enhancement Mechanisms with Microstructured Surfaces

As outlined earlier during the discussion of initial testing results, microstructured surfaces in this study, are believed to greatly enhance boiling through surface nucleation, in addition to other existing heat transfer mechanisms of free surface evaporation and boiling through secondary nucleation, in two phase regime. Based on the data presented in this section, further observations can be made.

The first type of surface considered, the surface ***s****, with its polished surface, did not provide any enhancement over the surface ***s***. At heat fluxes >300 W/cm$^2$, the surface ***s*** even resulted in slightly lower surface surperheats. This can be attributed to the tool marks on the surface ***s*** which can serve as nucleation sites. Highly polished surface on the other hand, minimizes the surface nucleation.

The surface ***mi*** possesses abundant indentations that boost surface nucleation. Results suggested that in the region up to 450 W/cm$^2$, lower roughness provides better performance. As long as the size of indentations are within the range of active cavity sizes for a certain surface superheat, having smaller indentations in a fixed spray area translates into more potential nucleation sites (or higher nucleation site density). The model developed by Hsu [31] can be used to predict the range of active cavity sizes, in terms of the minimum and maximum cavity mouth radius, $r_{c,\min}$ and $r_{c,\max}$, respectively, as

$$\left\{\frac{r_{c,\min}}{r_{c,\max}}\right\} = \frac{\delta_t}{4}\left[1-\frac{(T_{sat}-T_l)}{(T_{surf}-T_l)}\{\mp\}\sqrt{\left(1-\frac{(T_{sat}-T_l)}{(T_{surf}-T_l)}\right)^2-\frac{12.8\cdot\sigma\cdot T_{sat}}{\rho_v\cdot h_{fg}\cdot\delta_t\cdot(T_{surf}-T_l)}}\right] \tag{6}$$

where, $T_l$ is the bulk liquid temperature, $\sigma$ is the surface tension, $\rho_v$ is the vapor density, $h_{fg}$ is the latent heat of vaporization, and $\delta_t$ is the thermal boundary layer thickness that can be estimated as

$$\delta_t = \frac{k_l}{h} \tag{7}$$

where, $k_l$ is the liquid thermal conductivity.

Figure 4-24 presents the range of active cavity sizes for the case of saturated ammonia at 7 $^{o}$C. Here, $\delta_t$ was estimated using an $h$ value based on the cooling curve A-Ref in Figure 4-13, at the inception of two phase regime.

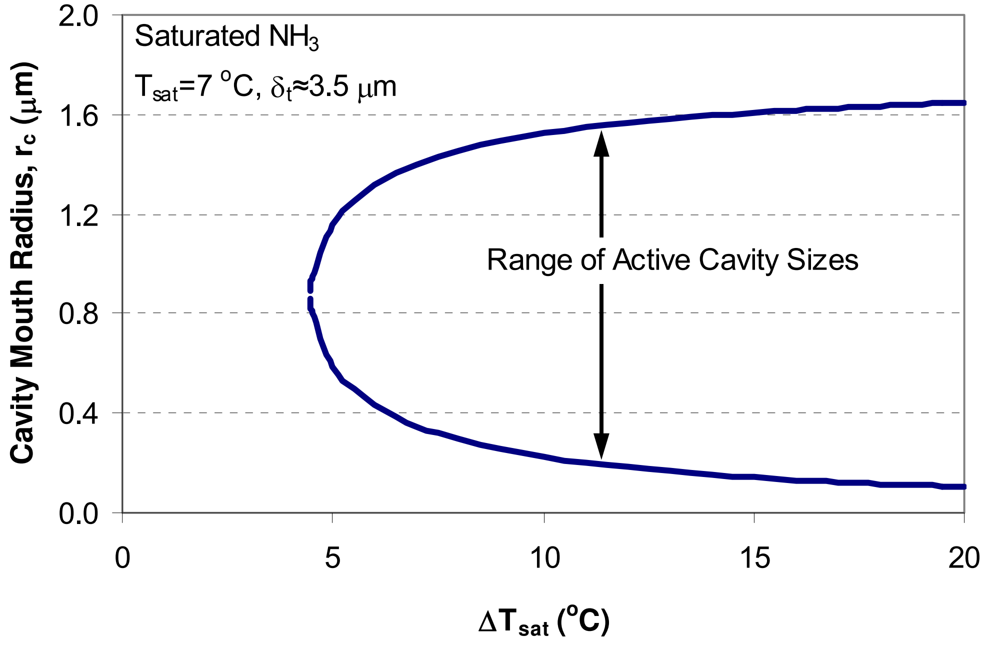

Figure 4-24: Prediction of the Range of Active Cavity Sizes Using Hsu's Analysis

Although the geometry of real cavities is highly irregular, it is reasonable to idealize the micro scale indentations in this study as conical cavities. The mouth radius of these conical cavities then can be assumed to be nearly half of the $R_a$ value. As shown in Figure 3-15, $R_a$ values of the surfaces ***mi-f***, ***mi-m*** and ***mi-c*** are 2.1, 3.2 and 4.6 μm, respectively. At 7 $^{o}$C surface superheat corresponding to the early part of two phase regime, for instance, the predicted range of active cavity sizes is 0.35 to 1.40 μm in Figure 4-24. Therefore, even the smallest cavity mouth radius found in the surface ***mi-f*** falls within the predicted range, and supports the conclusion that among the surfaces ***mi(-f,-m,-c)***, the surface ***mi-f*** would have more potential nucleation sites in a fixed area and perform better than the surfaces ***mi-m*** and ***mi-c***.

The surfaces ***mp(-f,-m,-c)*** resulted in an opposite trend where higher roughness provides better performance. As surface characterization efforts revealed, the surface ***mp*** in general features large surface area, and many randomly sized re-entrant cavities that can entrap vapor and facilitate nucleation at low surface superheats. Hence, the surface ***mp-c*** with its larger surface area is expected to have more of the re-entrant cavities and enter the two phase regime earlier than the surfaces ***mp-m*** and ***mp-f***.

### 4.4 Macrostructured Surfaces

Macrostructured surfaces featured mm-scale fins positioned normal to the spray nozzle. Their heat transfer enhancement was investigated in two steps, in terms of structure geometry and size. Initially, finite element analysis (FEA) was employed to gain better understanding on the effect of these parameters, and to narrow the test matrix down. Then four types of geometries, pyramidal, triangular, rectangular, and square pin fins, were tested and compared. Finally, the best performing geometry was further tested for various fin heights to reach the optimum configuration.

### 4.4.1 Results with Macrostructured Surfaces

A series of finite element analysis (FEA) was conducted to roughly evaluate the effect of macrostructure size and geometry on spray cooling performance, and determine the proper scope for actual test surfaces used in the experiments.

Optimization of macrostructured surfaces requires consideration of the parameters such as structure geometry, height, width and spacing as well as material. For this stage of the study, pyramidal, triangular, rectangular, and square pin fins were selected as structure geometries, and heater material was already determined as Al 6061. First, a unit building block of rectangular fin with 1 mm x 1 mm base area was used for FEA. A fin spacing of 0.50 mm was chosen that would eventually accommodate application of microstructures between the fins to form the multi-scale structured surface. Fin heights of 0.75 and 1.25 mm, with the fixed fin width of 0.50 mm, were then considered for comparison with a reference flat surface. In the FEA, heater bottom surface received a heat flux of 500 W/cm$^2$. The wetted spray surface including base and all fin surfaces were exposed to a temperature dependent heat transfer coefficient calculated from the reference experimental data, the cooling curve A-Ref in Figure 4-13. Use of this simple model at the beginning also helped the optimization of critical nonlinear FEA parameters. Figure 4-25 shows FEA results of the flat and two finned surfaces in terms of their temperature distribution across the heater base and fins. For a performance comparison, enhancement factor $EF_h$ was calculated for each surface. In the calculation of $h$, spray surface temperature $T_{surf}$ was obtained by extrapolating the bottom surface temperature through the heater wall, with the assumption of steady 1-D conduction, as

$$T_{surf} = T_{bottom} - \frac{(q''x)}{k} \tag{8}$$

where, $T_{bottom}$ is the average temperature on the bottom surface of FEA model.

Figure 4-26 presents calculated $EF_h$ as a function of fin height. As expected, $EF_h$ increases as fin height increases. While the 0.75 mm high fin provide a 9% improvement, the taller 1.25 mm high fin only adds another 1% improvement.

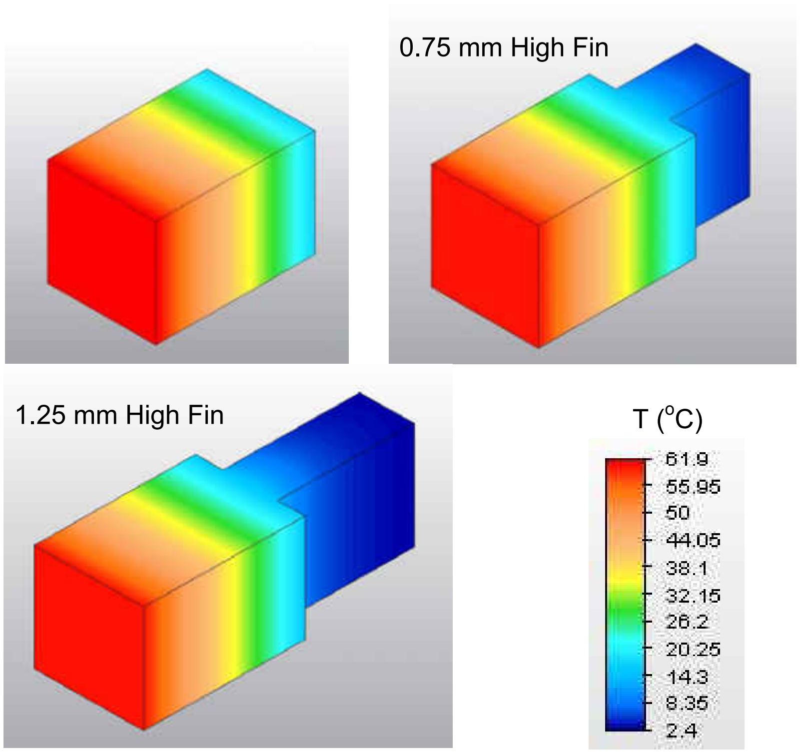

Figure 4-25: FEA Temperature Distributions on Flat and Finned Geometries (Al6061)

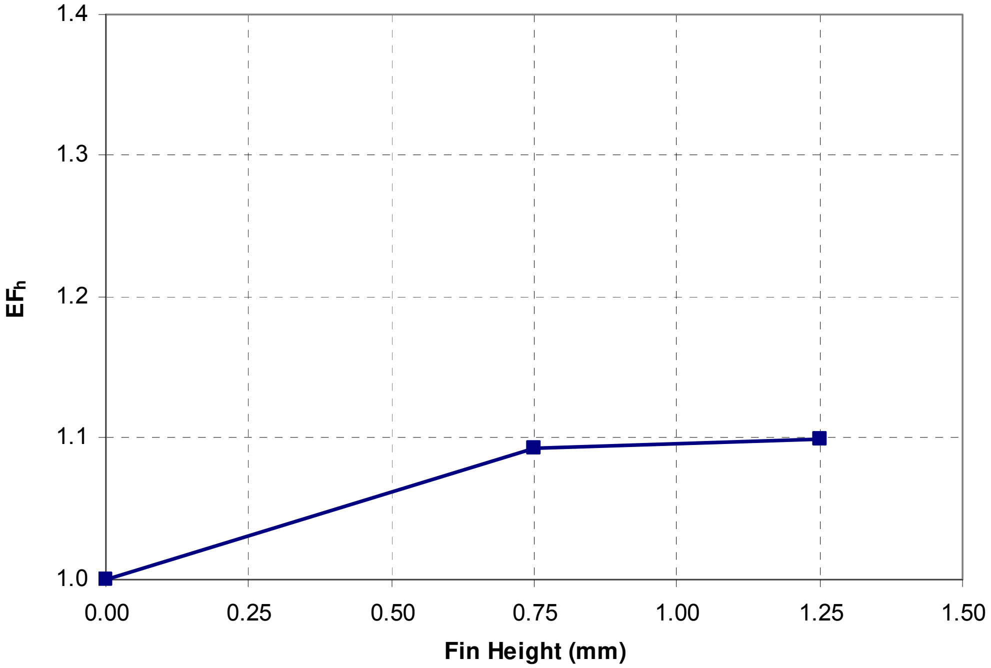

Figure 4-26: FEA Based Performance Enhancement Factor as a Function of Fin Height (Al6061)

In order to evaluate the effect of fin material on enhancement, the same analysis was repeated for Cu fins. The much higher thermal conductivity of oxygen-free Cu (391 W/m$^o$C) compared to that of Al 6061 (167 W/m$^o$C) made a noticeable difference as shown in Figure 4-27 and Figure 4-28. Here, 0.75 and 1.25 mm high fins provide 30% and 33% heat transfer enhancement, respectively.

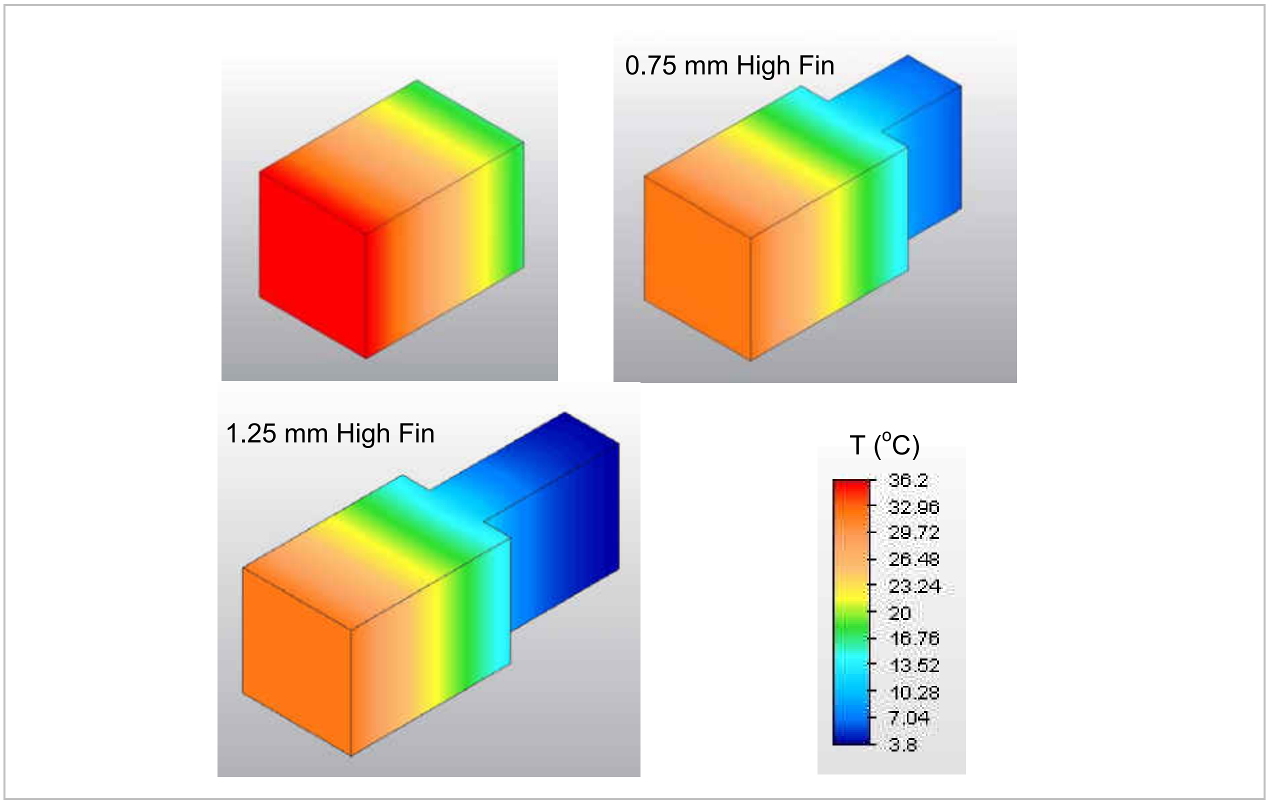

Figure 4-27: FEA Temperature Distributions on Flat and Finned Geometries (Cu)

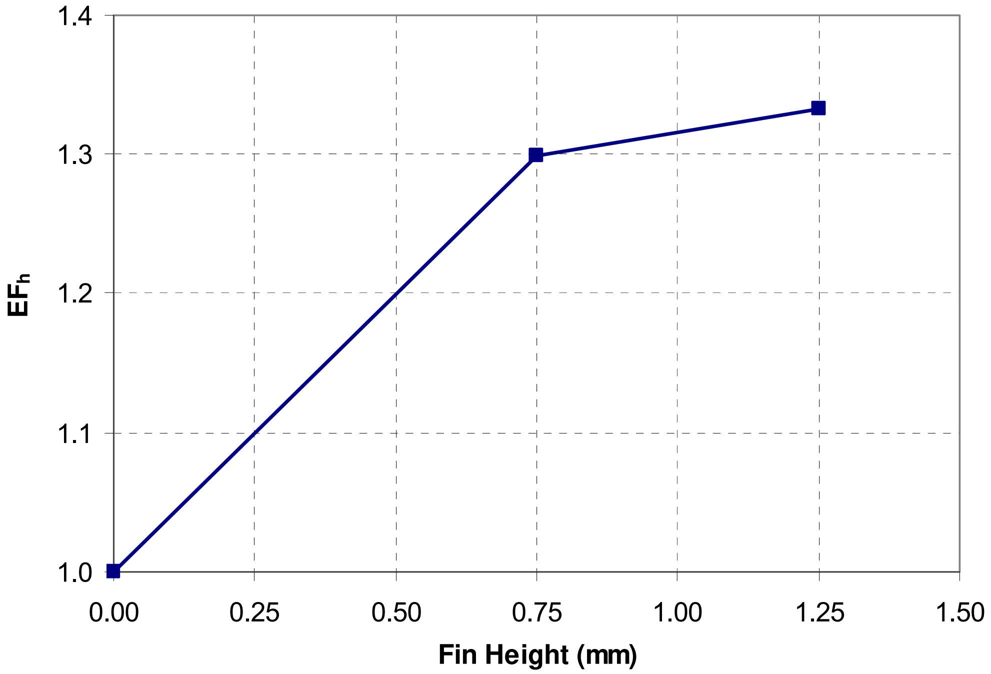

Figure 4-28: FEA Based Performance Enhancement Factor as a Function of Fin Height (Cu)

These FEA results therefore, especially the ones for Al6061 fins, suggested the limitation of fin height to 0.75 mm. Next round of FEA was aimed to evaluate the four structure geometries at a fixed 0.75 mm fin height, utilizing quarter models of the test heaters with 5 mm x 5 mm base area. After obtaining temperature distributions, shown in Figure 4-29, performance of these four fin geometries was compared in a similar way through the calculation of $EF_h$. Figure 4-30 includes the results where finned surfaces having an area increase of ≈1.5-1.6X, only provide performance enhancements of up to 5%. In the case of triangular fins, performance was lower than that of the reference flat surface. This FEA effort however was not expected to be capable of capturing the complex spray cooling mechanisms, and the results were considered as a useful tool for initial design process.

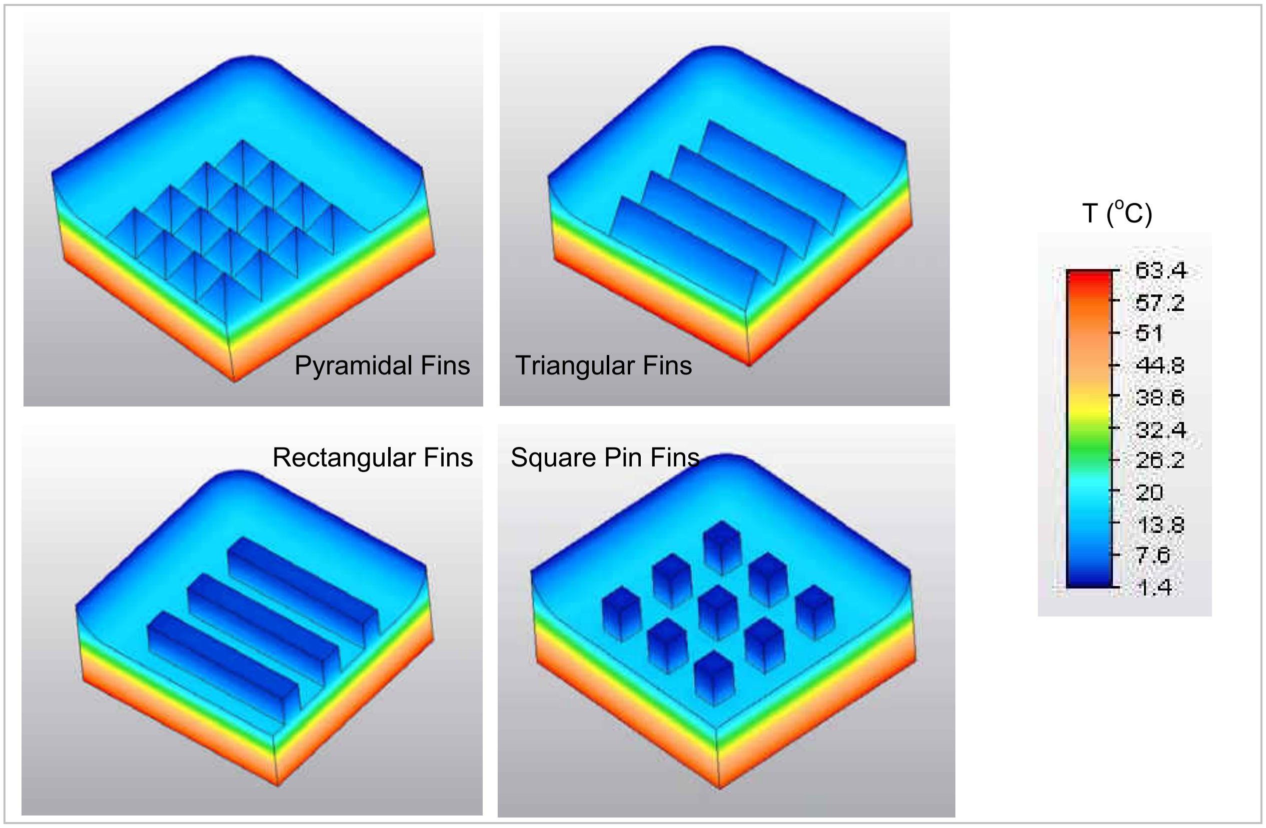

Figure 4-29: FEA Temperature Distributions on Four Macrostructure Geometries

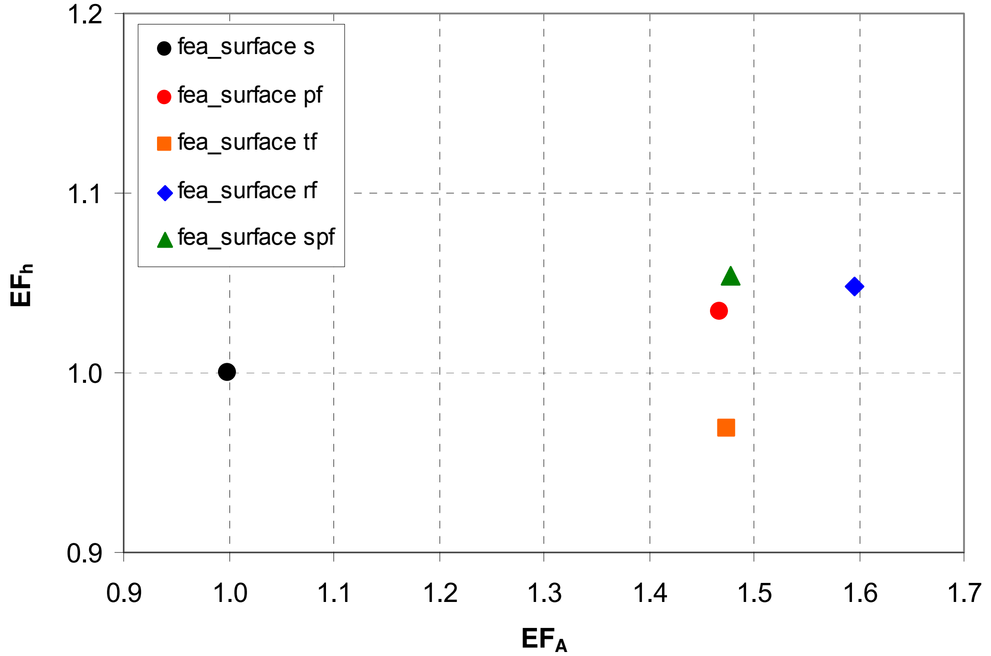

Figure 4-30: FEA Based Performance Enhancement Factor vs. Area Enhancement Factor for Four Macrostructure Geometries

Once the FEA study was completed, a full set of experiments was resumed to evaluate the actual performance of macrostructured surfaces. First, heaters featuring four types of fin geometries with a fixed fin height of 0.75 mm were tested for the effect of structure geometry. As the cooling curves in Figure 4-31 reflect, these surfaces experienced an extended single phase regime, and entered the two phase regime quite late at higher surface superheats. Therefore, none of the tested geometries were able to provide an enhancement over the surface ***s***. While the results from the surface ***Mpf-0.75*** are comparable to the surface ***s*** at 500 W/cm$^2$, the surfaces ***Mtf-0.75***, ***Mrf-0.75***, and ***Mspf-0.75*** yielded higher surface superheats. Normalized resistor temperatures of four types of macrostructured surfaces are compared in Figure 4-32. This plot also includes data from the additional heaters, ***A34Mpf-0.75*** and ***A28Mrf-0.75***, used to repeat the pyramidal and rectangular fin tests later. As shown, these tests generated consistent data, and marked the pyramidal fins as the best structure geometry.

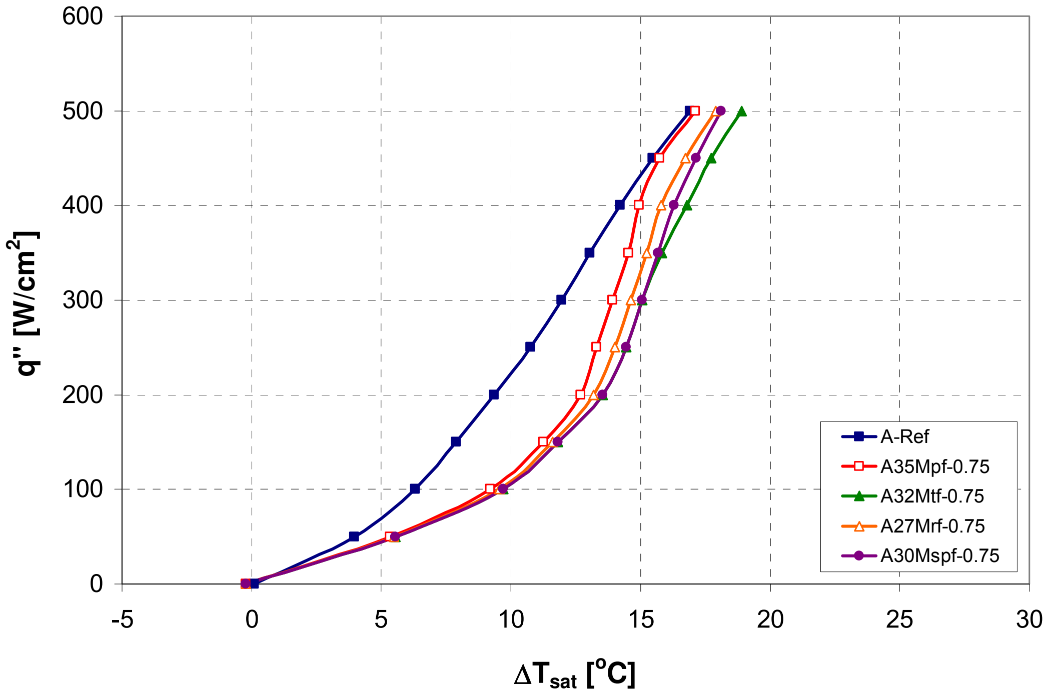

Figure 4-31: Heat Transfer Performance of the Surfaces ***Mpf***, ***Mtf***, ***Mrf***, and ***Mspf***

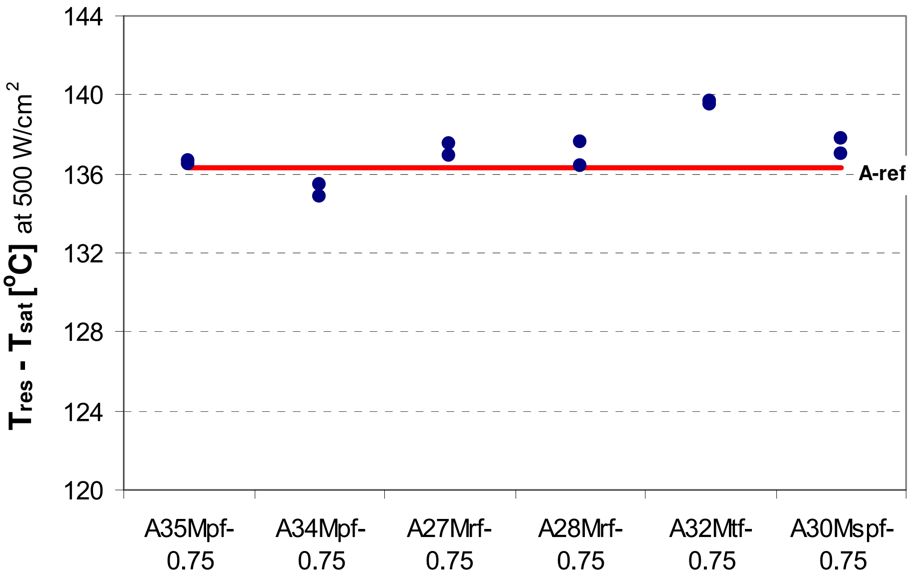

Figure 4-32: IR Thermography Based Normalized Resistor Temperatures for the Surfaces ***Mpf***, ***Mtf***, ***Mrf***, and ***Mspf***

In the next step of the evaluation of macrostructured surfaces, two more heaters with shorter, 0.50 and 0.25 mm high pyramidal fins were tested. Data in Figure 4-33 clearly illustrate that shorter pyramids help transition to two phase regime (region II) earlier, and provides lower superheats throughout. At 500 W/cm$^2$, the surfaces ***Mpf-0.50*** and ***Mpf-0.25*** lower the superheat by 2.6 and 5.3 $^o$C, respectively, compared to the initially tested surface ***Mpf-0.75***. However, the surface superheats at low heat fluxes are still higher than that of the surface ***s***. Figure 4-34 includes normalized resistor temperatures that decrease as structure height decrease, and thus validates the performance of the surfaces ***Mpf(-0.75, -0.50, -0.25)***.

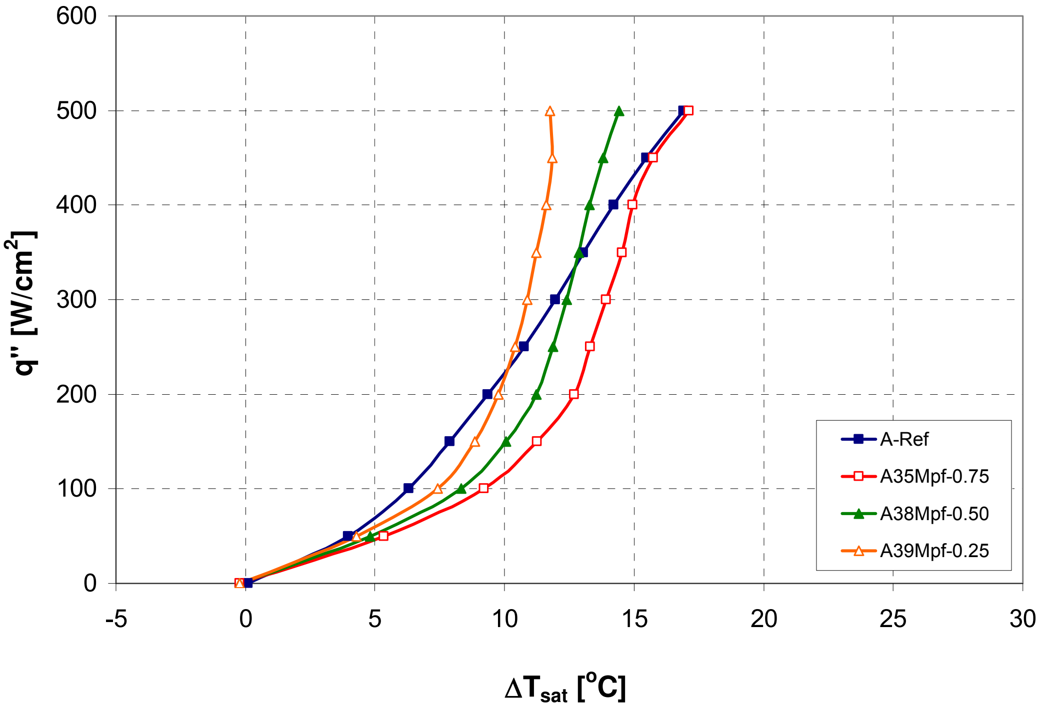

Figure 4-33: Heat Transfer Performance of the Surfaces ***Mpf(-0.75, -0.50, -0.25)***

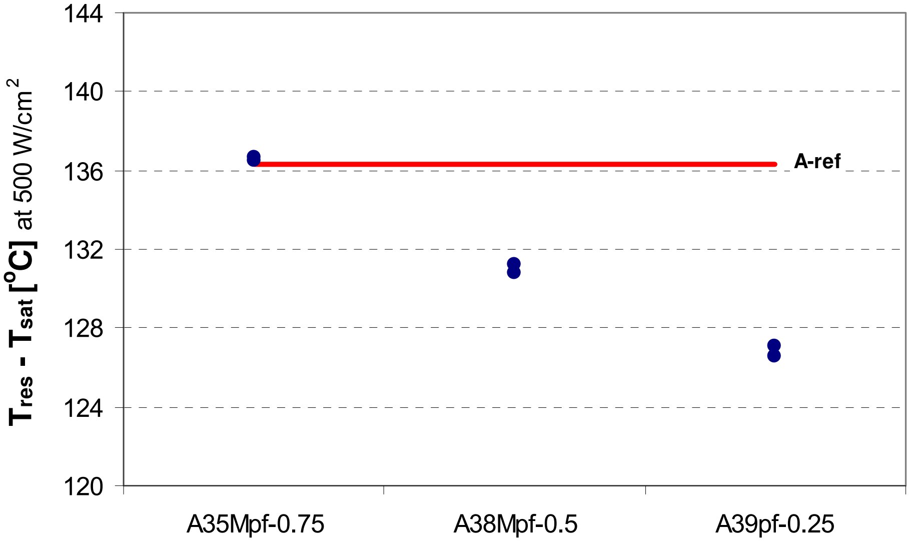

Figure 4-34: IR Thermography Based Normalized Resistor Temperatures for the Surfaces ***Mpf(-0.75, -0.50, -0.25)***

The performance comparison of all tested macrostructured surfaces in terms of the heat transfer coefficient is provided in Figure 4-35 and Figure 4-36. The highest heat transfer coefficient of 426,000 W/m$^{2o}$C here was reached by the surface ***Mpf-0.25***, offering a 44% enhancement over the surface ***s***.

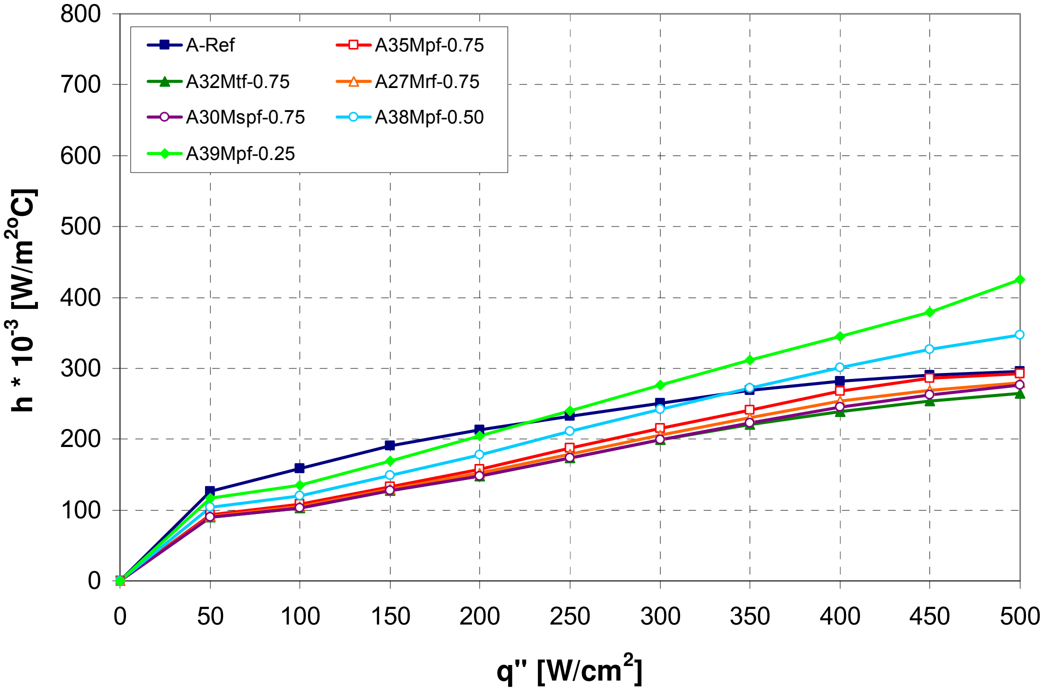

Figure 4-35: Performance Comparison of All Macrostructured Surfaces Based on Heat Transfer Coefficient at Heat Fluxes of Up to 500 W/cm$^2$

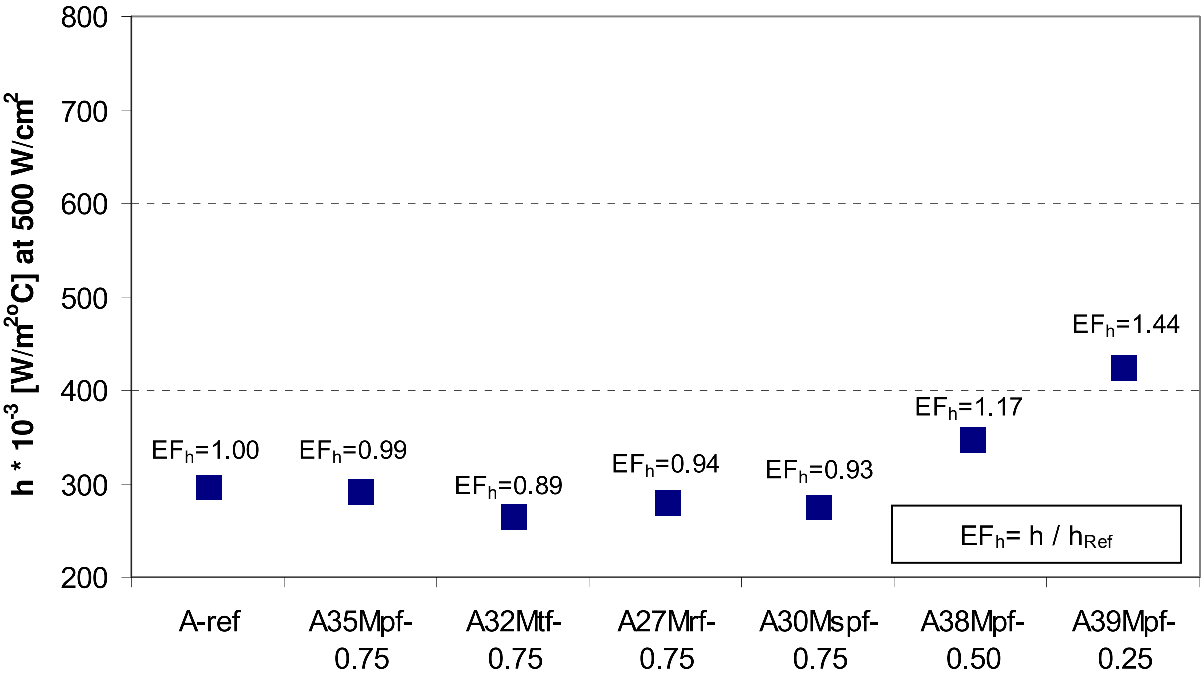

Figure 4-36: Performance Comparison of All Macrostructured Surfaces Based on Heat Transfer Coefficient at Heat Flux of 500 W/cm$^2$

### 4.4.2 Heat Transfer Enhancement Mechanisms with Macrostructured Surfaces

Although the initial evaluation of macrostructured surfaces for the effect of geometry indicated that the surface ***Mpf-0.75*** was slightly better than the others, the reasoning behind it was not very obvious. Most likely the pyramidal fins offer the most favorable temperature distribution in the structures. When pyramids were investigated further by varying the structure size, but specifically keeping their surface area enhancement constant (over the flat reference surface), the shortest pyramids performed the best. This can be attributed to some advantages shorter structures have, such as lower added thermal resistance, higher superheat on the fin surfaces, and more direct liquid access to the substrate due to the longer boundary around the structure base.

## 4.5 Multi-scale Structured Surfaces

Third group of enhanced surfaces, multi-scale structured surfaces, incorporated the combination of best performing macro and micro scale structures. Based on the earlier results, the surfaces ***Mpf-0.25***, ***mi-f***, and ***mp-c*** were considered to produce the two new surfaces of ***Mpf-0.25mi-f*** and ***Mpf-0.25mi-f*** for the evaluation.

### 4.5.1 Results with Multi-scale Structured Surfaces

Data from the multi-scale structured surfaces in Figure 4-37 indicates that for the surface ***Mpf-0.25mi-f***, two phase effects starts to dominate after 100 W/cm$^2$ and the performance is characterized by a very steep curve resulting in a wide range of heat flux removal at nearly constant surface temperature. For the surface ***Mpf-0.25mi-f***, boiling through surface nucleation picks up even earlier, after 50 W/cm$^2$, and results in lower superheat at heat fluxes of up to 450 W/cm$^2$. However, at 500 W/cm$^2$, performance of the two multi-scale structured surfaces match, achieving the lowest surface superheat of 6.48 $^{o}$C. IR thermography based normalized resistor temperatures in Figure 4-14 confirms the results, indicating these two heaters have the matching, and the lowest resistor temperatures obtained so far.

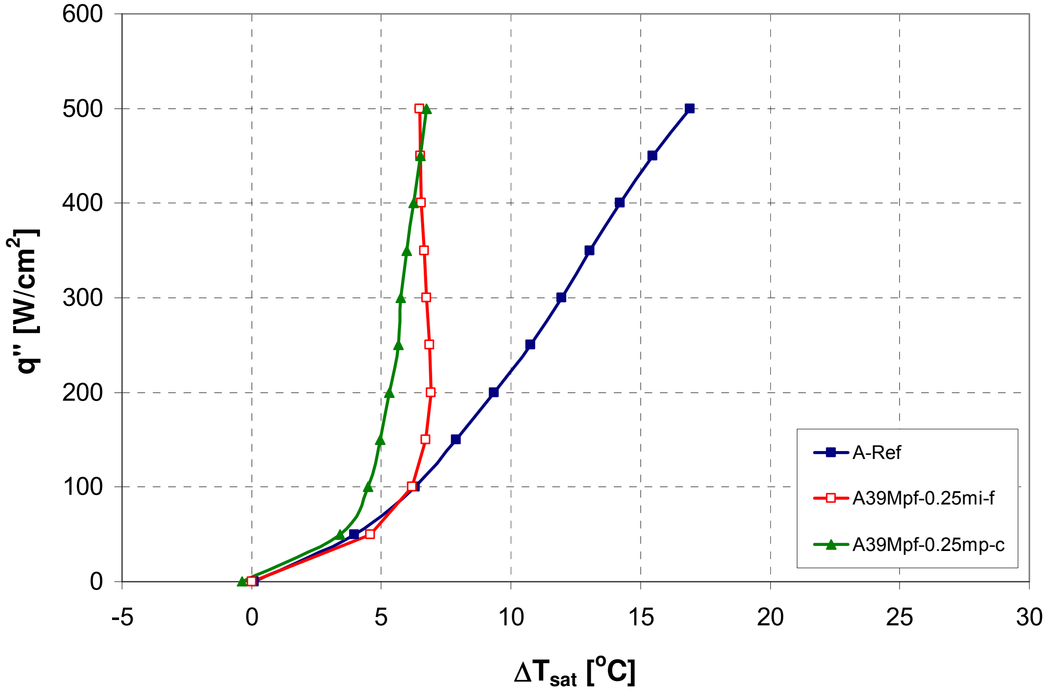

Figure 4-37: Heat Transfer Performance of the Surfaces ***Mpf-0.25mi*** and ***Mpf-0.25mp***

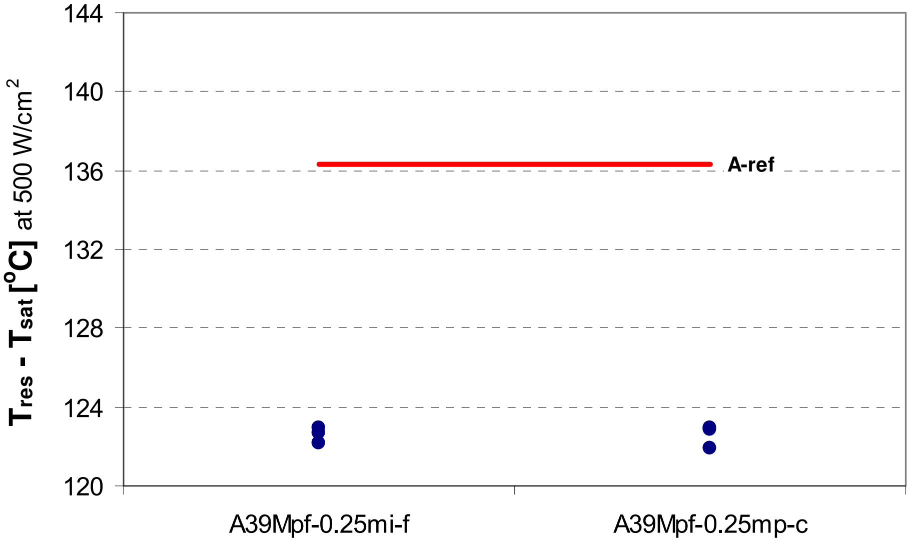

Figure 4-38: IR Thermography Based Normalized Resistor Temperatures for the Surfaces ***Mpf-0.25mi-f*** and ***Mpf-0.25mp-c***

Figure 4-39 and Figure 4-40 compare the performance of multi-scale structured surfaces in terms of the heat transfer coefficient. The surfaces ***Mpf-0.25mi-f*** and ***Mpf-0.25mp-c*** provide heat transfer coefficients of 772,000 and 741,000 W/m$^{2o}$C at 500 W/cm$^2$, respectively, corresponding to 161% and 150% improvement over the surface ***s***. These data also mark the best performance of the enhanced surfaces tested so far.

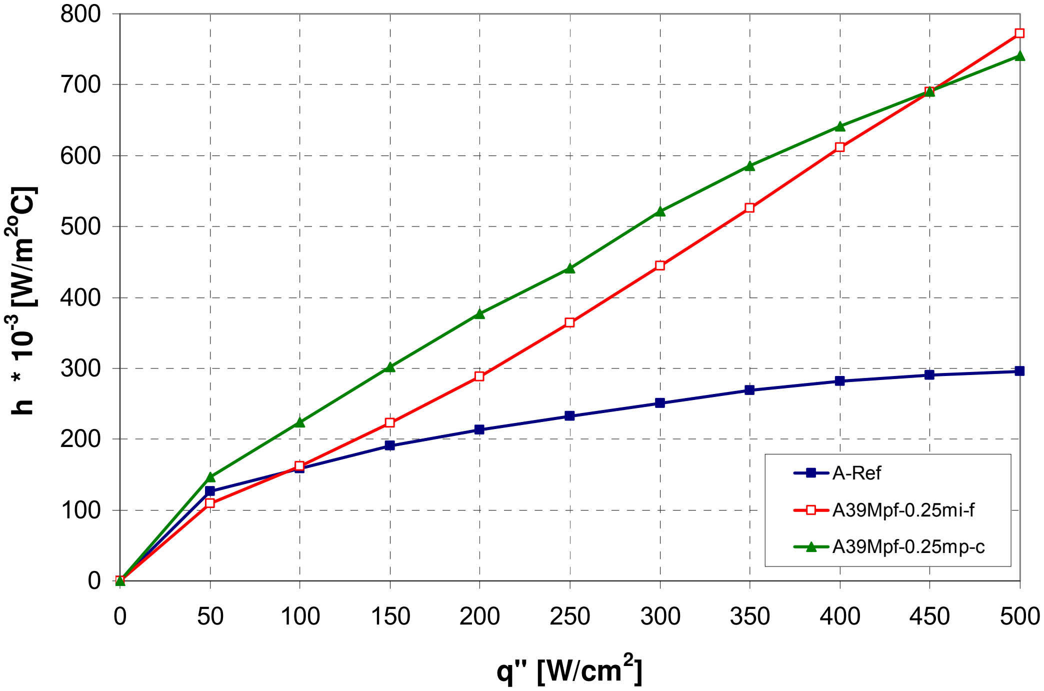

Figure 4-39: Performance Comparison of All Multi-scale Structured Surfaces Based on Heat Transfer Coefficient at Heat Fluxes of Up to 500 W/cm$^2$

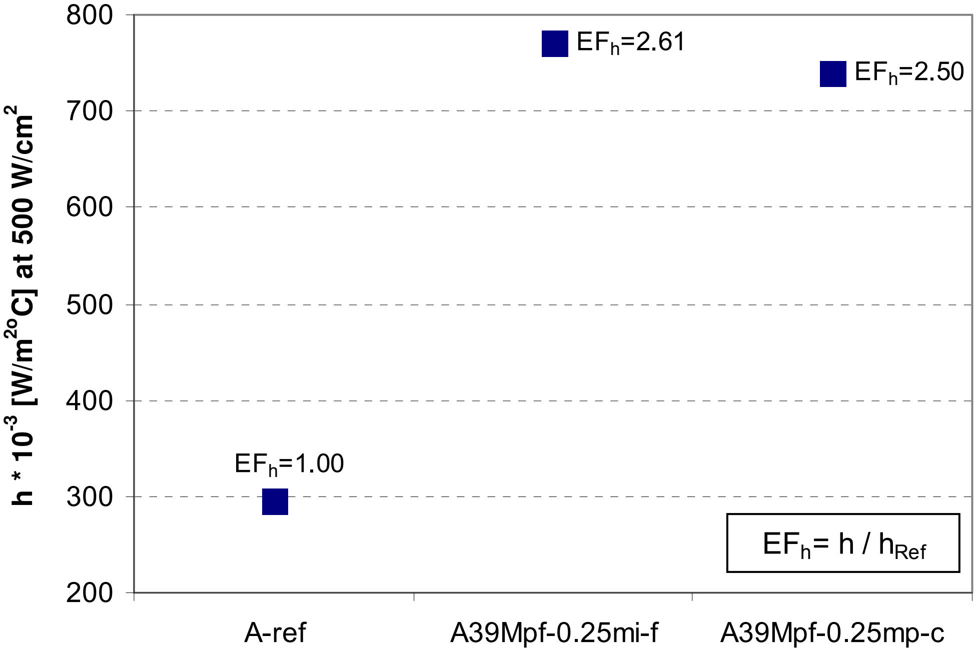

Figure 4-40: Performance Comparison of All Multi-scale Structured Surfaces Based on Heat Transfer Coefficient at Heat Flux of 500 W/cm$^2$

### 4.5.2 Heat Transfer Enhancement Mechanisms with Multi-scale Structured Surfaces

Performance enhancement level of multi-scale structured surfaces ($EF_h$=2.61 at 500 W/cm$^2$) exceeded those from both micro- and macrostructured surfaces individually ($EF_h$=1.81 and 1.44 at 500 W/cm$^2$). Actually, results quantitatively indicate that the enhancement level in terms of heat transfer coefficient is additive. Therefore it can be concluded that the previously outlined enhancement mechanisms for micro- and macrostructured surfaces work simultaneously, allowing the multi-scale structured surfaces to take advantage of all.

# CHAPTER 5: INVESTIGATION OF ENHANCED SURFACES FOR CRITICAL HEAT FLUX

This chapter reports and discusses the second part of the current study, on experimental investigation of selected enhanced surfaces for their heat removal limit, or critical heat flux (CHF), in two sections. First section determines the CHF values of each surface at the initially optimized spray conditions. The following section evaluates the effect of higher flow rates on CHF and spray cooling efficiency.

## 5.1 CHF Tests with Selected Enhanced Surfaces

CHF tests were conducted using type ***C*** heaters with selected enhanced surfaces featuring micro, macro, and multi-scale structures. Spray conditions, optimized for heat fluxes of up to 500 W/cm$^2$, were maintained by applying the previous nominal liquid and vapor flow rates, and the heat removal limit of each surface is determined.

### 5.1.1 Results with Selected Enhanced Surfaces

Heaters with the surface ***s*** were tested first, to obtain reference data for the CHF study. Results from two heaters, in Figure 5-1, appear very consistent over almost the entire testing range. Eventually one of the heaters reached CHF at 760 W/cm$^2$, while the other one attained a higher CHF at 780 W/cm$^2$.

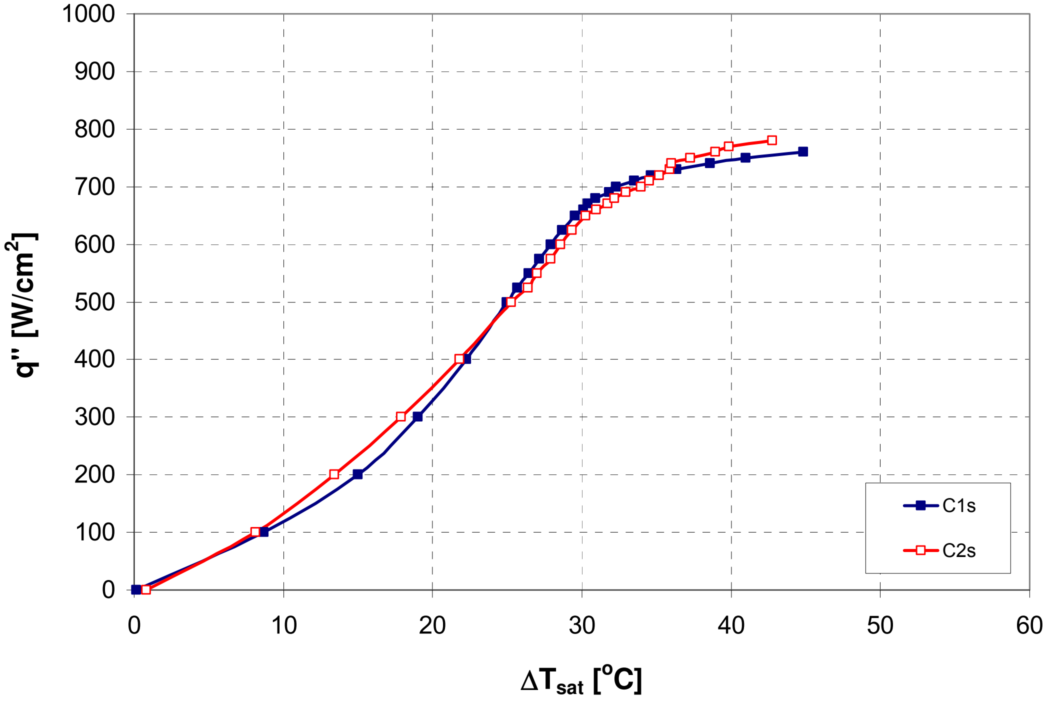

Figure 5-1: CHF Performance of the Surface *s* from Two Different Heaters

A reference cooling curve was then established by averaging data from the two tested heaters. Figure 5-2 includes these average data along with the marked lines that demonstrate the three distinct heat transfer regimes of spray cooling, as explained earlier. In the first part of the study, heat flux was limited to 500 W/cm$^2$, and thus cooling curves reflected the regions I and II only, corresponding to single phase forced convection and two phase boiling/evaporation regimes. In CHF tests, region III, characterized by a rolling over, lower slope curve also exists that represents the two phase-to-CHF transition.

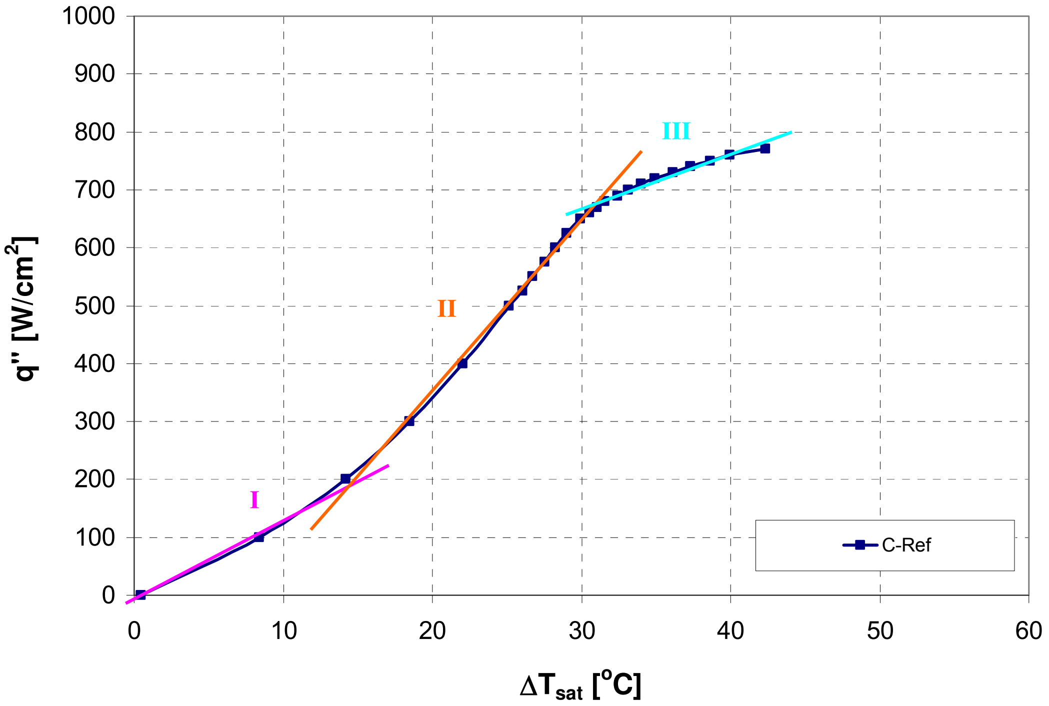

Figure 5-2: Reference Cooling Curve for Type ***C*** Heaters Representing Average CHF Performance of the Surface ***s*** from Two Different Heaters

Two types of microstructured surfaces, ***mi-c*** and ***mp-c***, both featuring coarse size roughness, were tested next. Figure 5-3 includes data from these two heaters and compares them to the surface ***s***. The surface ***mi-c*** reached CHF at 780 W/cm$^2$, and the surface ***mp-c*** reached CHF at a much higher level at 910 W/cm$^2$. Two surfaces also exhibited different cooling curves. The surface ***mp-c*** entered two-phase regime early on, and had higher heat transfer coefficients up to 500 W/cm$^2$. At higher heat fluxes however, the surface ***mi-c*** performed better and reached CHF sooner. The surface ***mp-c*** transitioned to region III much slower resulting in a higher CHF and surface superheat.

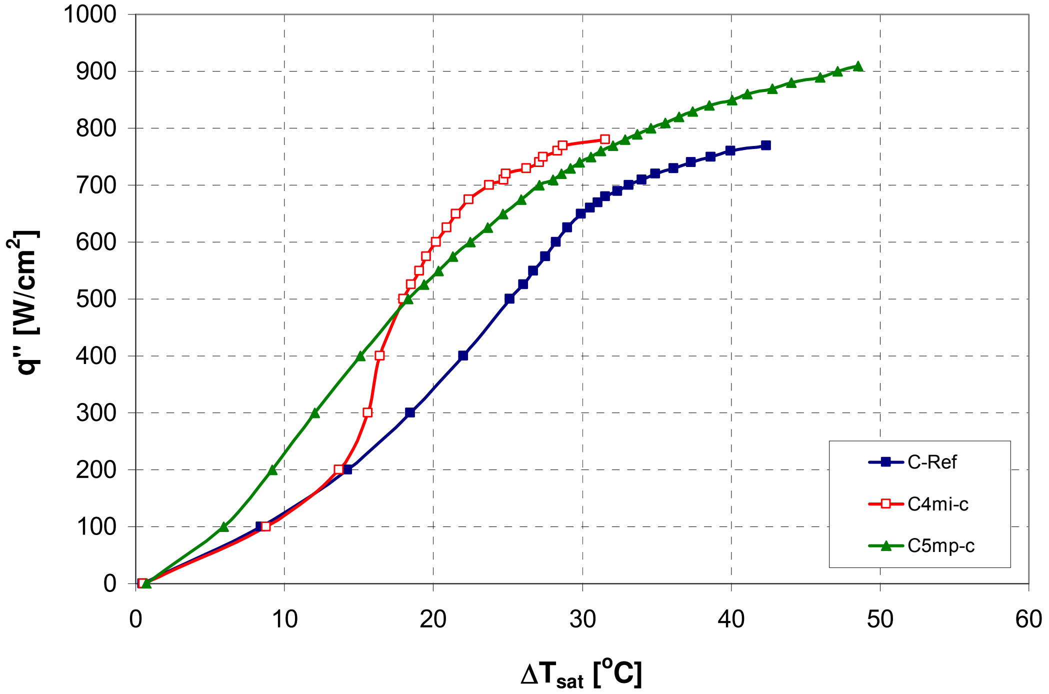

Figure 5-3: CHF Performance of the Surfaces ***mi-c*** and ***mp-c***

To investigate the CHF performance of macrostructured surfaces, a surface with 0.50 mm high pyramids, ***Mpf-0.50***, was selected. Data in Figure 5-4 indicate that this surface reached CHF at 850 W/cm$^2$, and compared to the surface ***s***, had a superior performance throughout the testing range.

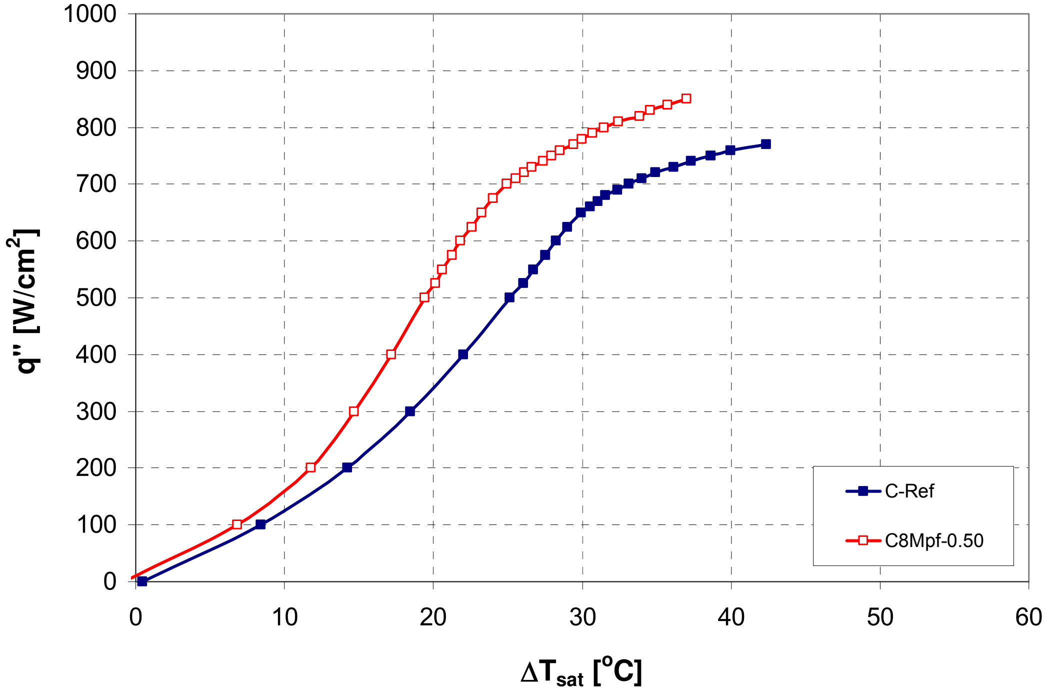

Figure 5-4: CHF Performance of the Surface ***Mpf-0.50***

Following the micro- and macrostructured surfaces, two other heaters with multi-scale structured surfaces were tested to evaluate the effect of combined structures on CHF. Of these, the surface ***Mpf-0.50mi-c***, performed better than the surface ***mi-c***, and reached CHF at 820 W/cm$^2$ as shown in Figure 5-5. The other surface, ***Mpf-0.50mp-c***, performed same as the previously tested surface ***mp-c***, and provided a CHF of 910 W/cm$^2$. As far as the overall heat transfer performance is concerned, the surface ***mp-c*** was better than the surface ***mi-c*** up to 500 W/cm$^2$, where two curves crossed over, and at higher heat fluxes the surface ***mi-c*** offered higher heat transfer coefficients. The contribution of 0.50 mm high pyramids to the performance of microstructures was not significant as evidenced by ≈1.5 $^o$C lower superheat at 500 W/cm$^2$.

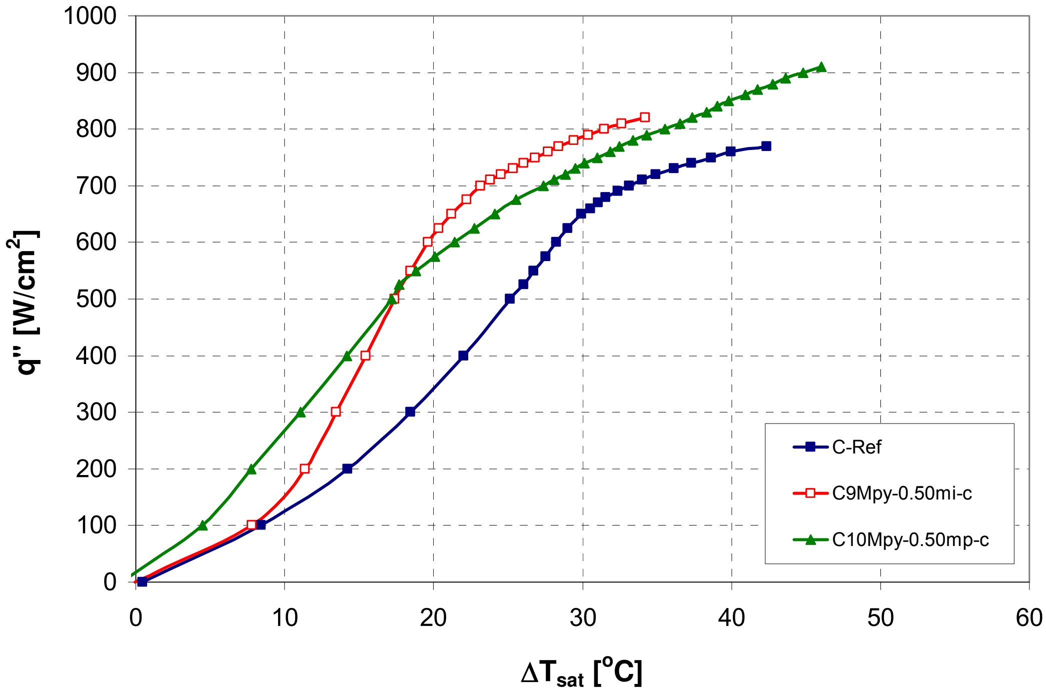

Figure 5-5: CHF Performance of the Surfaces ***Mpf-0.50mi-c*** and ***Mpf-0.50mp-c***

Finally, it would be useful to compare all the CHF results obtained from six heaters. Figure 5-6 summarizes results side by side, and identifies the enhancement factor $EF_{CHF}$, as

$$EF_{CHF} = \frac{CHF}{CHF_{ref}} \tag{9}$$

to express each heater's CHF enhancement over the reference surface. As can be noticed, while the surface ***mi-c*** offers a minimal 1% improvement, the surface ***mp-c*** provides 18% increase in CHF over the surface ***s***. The surface ***Mpf-0.50*** alone offer 10% enhancement. When the surface ***Mpf-0.50*** is combined with the surfaces ***mi-c*** and ***mp-c***, they result in 6% and 18% improvement, respectively. These results therefore suggest that CHF enhancement due to the multi-scale structures is not additive.

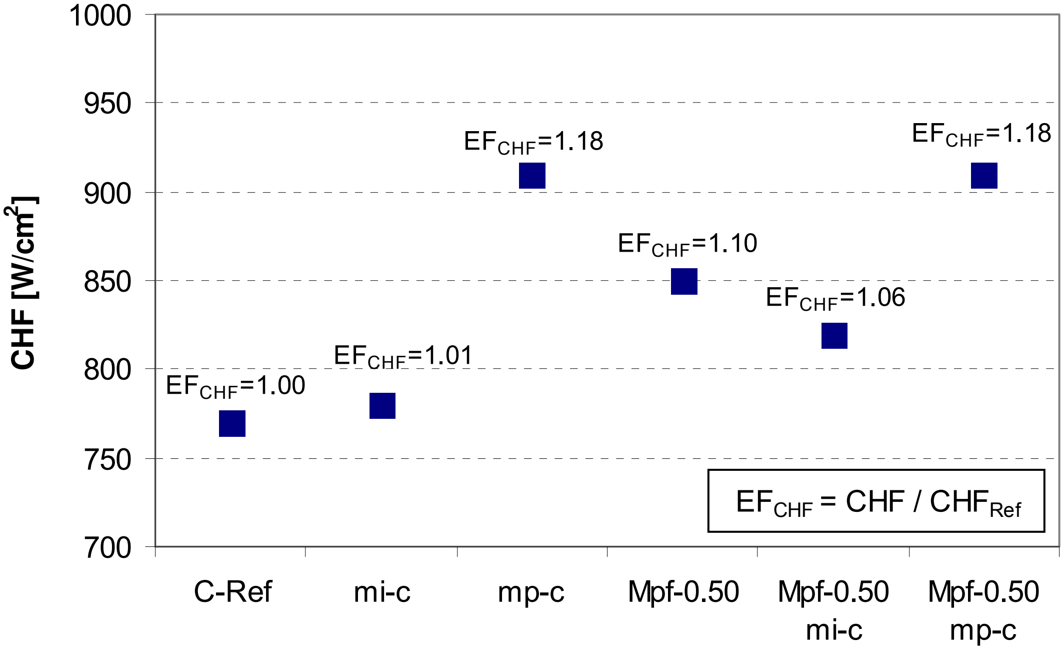

Figure 5-6: Performance Comparison of Selected Enhanced Surfaces Based on CHF

Efficiency is another important performance parameter. Spray cooling efficiency in general can be defined as the ratio of the actual heat removed to the total heat capacity of the liquid used, including the required heat to bring the liquid from sub-cooled to saturation condition (sensible heat), and then to complete vaporization (latent heat). This efficiency definition $\eta$ can be expressed as

$$\eta = \frac{q''}{\dot{V}\rho_l(c_p\Delta T_{sub} + h_{fg})} \tag{10}$$

where, $\dot{V}$ is volumetric flow rate, $\rho_l$ is liquid density, $c_p$ is specific heat, $\Delta T_{sub} = T_{sat} - T_l$ is subcooling, and $h_{fg}$ is latent heat of vaporization. Since saturated spray conditions were maintained throughout this study, total heat capacity of the used liquid is equivalent to its latent heat of vaporization.

Spray cooling efficiencies of all surfaces at their respective CHF values are summarized in Figure 5-7, and can be seen to range from 63.4%, for the surface ***s***, to 74.9% for the surfaces ***mp-c*** and ***Mpf-0.50mp-c***.

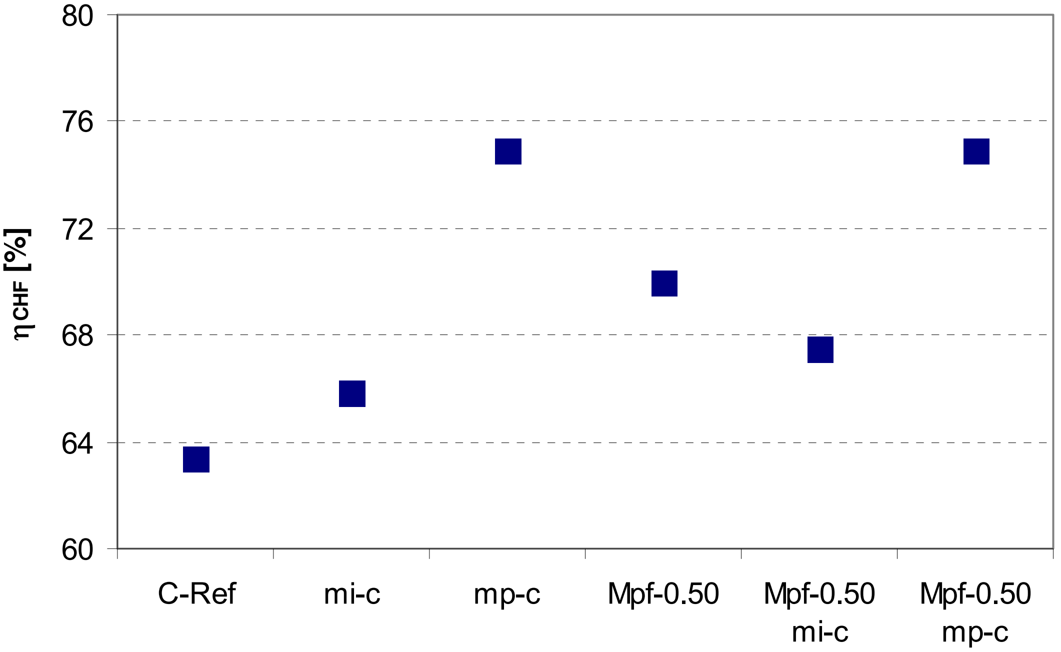

Figure 5-7: Spray Cooling Efficiency of Selected Enhanced Surfaces at Their CHF Values

### 5.1.2 CHF Enhancement Mechanisms with Selected Enhanced Surfaces

The CHF data showed that selected micro- and macrostructured surfaces provided quite different levels of improvement over the surface ***s***, in the range of 1% to 18%. Combining these structures in the multi-scale structured surfaces did not help further.

CHF enhancement mechanism here might be explained considering how different surfaces affect fluid distribution on the spray surface. In general, rough, porous or textured surfaces would retain more liquid compared to a smooth surface for a given spray nozzle and flow rate. They also provide an efficient means to spread the liquid film via capillary force within the micro scale structures, as also observed and reported by several experimental studies [13, 15, 18]. This unique advantage delays the occurrence of dry patches at high heat fluxes and leads to higher CHF.

In the current study, based on both qualitative visual observations, and quantitative surface roughness analysis results, the surface ***mp-c*** possesses the highest roughness, overall structure height, and actual surface area with plenty re-entrant cavities. Therefore the surface ***mp-c*** is expected to hold more liquid, and spread it very efficiently in order to keep the surface wet longer and achieving higher CHF values. The surface ***mi-c*** on the other hand, exhibits lower roughness and open cavities, that can still hold more liquid than a smooth surface, but cannot resist liquid film break up as efficiently as the surface ***mp-c*** at high fluxes leading to very slight CHF improvement over smooth surface. The surface ***Mpf-0.50*** naturally forms grooves between adjacent pyramids that can help manage the liquid distribution in the preferred way. However, as experimental data implied, its enhancement level is between that of the two other microstructured surfaces.

This mechanism also explains why the surface ***mp-c*** performs better than the surface ***mi-c*** up to a certain heat flux, but the trend reverses afterwards during CHF tests. Although surface nucleation is very effective at the low to medium heat fluxes (<500 W/cm$^2$), evaporation might gradually become more pronounced at higher heat fluxes. Hence, the surface ***mi-c*** with thinner liquid film starts to offer higher heat transfer coefficients beyond 500 W/cm$^2$. Eventually this thin film breaks up resulting in much less effective dry patches, and heater soon approaches to CHF. The surface ***mp-c*** with thicker liquid film, would have a lower evaporation rate and consequently lower heat transfer coefficients, but also extends the transition to CHF.

## 5.2 Effect of Flow Rate on CHF

First part of CHF study determined the CHF limits of selected enhanced surfaces using nominal flow rates of 1.6 mL/cm$^2$-s liquid, and 13.8 mL/cm$^2$-s vapor. For spray cooling, it has been established that increasing the liquid flow rate would help to increase CHF for a given nozzle. However, the increase in CHF is not proportional, and is only effective up to a certain level, beyond which CHF remains relatively same [1, 32]. This can be attributed to the counterbalance of various spray cooling heat transfer mechanisms driven by the advantage of higher droplet velocity and the disadvantage of higher film thickness. Other studies [33, 34[34], defined three independent spray parameters of the mean droplet velocity (V), the mean spray droplet flux (N), and the Sauter-mean droplet diameter ($d_{32}$), and determined their effects on the CHF utilizing extensive experimental data. It was found that CHF varies with $V^{1/4}$ and $N^{1/6}$, and is relatively independent of $d_{32}$. Although these spray parameters are not specifically measured in the current work, it can still be assumed that higher flow rates would increase V, N and $d_{32}$ simultaneously.

Use of higher flow rates for improved CHF performance also brings system level implications, such as higher pumping power, affects cooling efficiency, and might require further optimization. When CHF is the main design consideration, however, higher flow rates would be helpful. This section therefore investigates the CHF limits of the selected surfaces at higher flow rates listed in Table 5-1.

Table 5-1: Flow Rates Used in CHF Tests

| Condition | Liquid Flow Rate ($mL/cm^2$-s) | Vapor Flow Rate ($mL/cm^2$-s) |
|---|---|---|
| Nominal / Low | 1.6 | 13.8 |
| Medium | 1.8 | 15.7 |
| High | 2.1 | 17.7 |

Figure 5-8 presents all the data from CHF tests at low, medium, and high flow rate conditions, in four separate plots for easier comparison between reference, and micro-, macro-, and multi-scale structured surfaces. The surface ***s*** was tested at all three flow rate conditions, and CHF values at medium and high flow rates were the same at 930 W/$cm^2$. Data thus suggested that increasing flow rate beyond the medium level has no considerable effect on CHF.

Once this trend was established, other heaters were decided to test only at high flow rates in addition to nominal/low flow rates. All heaters with enhanced surfaces, however, consistently failed during high flow rate CHF tests at heat fluxes starting at 960 W/$cm^2$. These data points are marked as “heater limit” in the plots, to distinguish them from CHF condition. Considering the elevated temperatures at these heat flux levels, thick film resistors most likely cracked due to the stresses induced by thermal expansion mismatch. As a result, true CHF value for these conditions could not be experimentally obtained. The surfaces ***Mpf-0.50mp-c*** and ***mp-c*** attained the highest heat flux, but not CHF, of 1090 W/$cm^2$ before the heater damage occurred.

As far as the overall heat transfer performance, besides CHF, is concerned, higher flow rates only helped the surface ***s*** with higher heat transfer coefficients. For other surfaces high flow rate generally resulted in slightly higher superheats at heat fluxes of up to 700 W/cm$^2$. Above this heat flux, higher flow rate extended the region II, and delayed transition to region III.

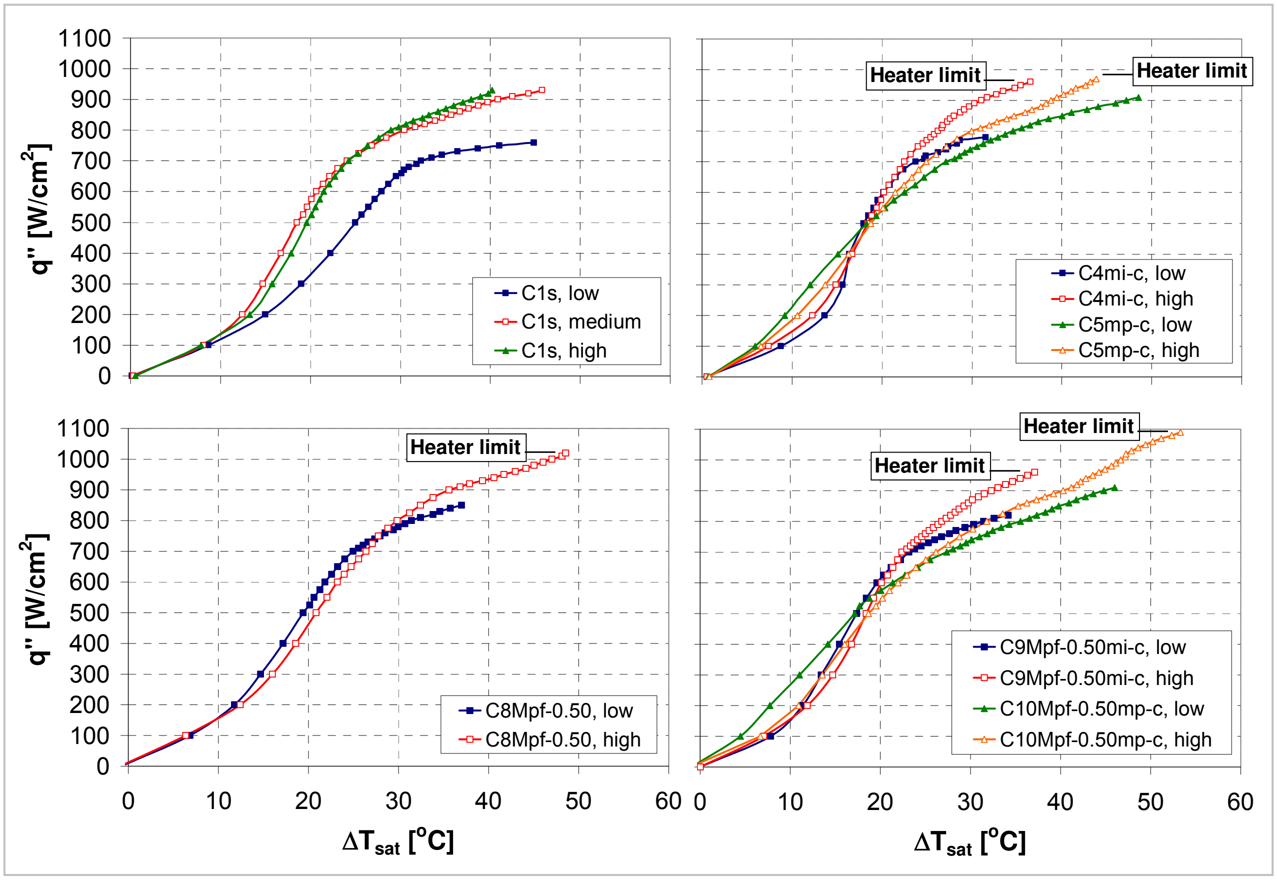

Figure 5-8: Results from CHF Tests at Various Flow Rate Conditions for Reference, and Micro-, Macro-, and Multi-scale Structured Surfaces

In an effort to further confirm the effect of flow rate on CHF, some additional tests were conducted with the surface ***s*** at medium and high flow rates. Figure 5-9 includes two CHF data at each considered flow rate. As shown, CHF values varies between 760-780 W/cm$^2$ for low, 890-930 W/cm$^2$ for medium, and 920-930 W/cm$^2$ for the high flow rates, and suggest that CHF values are not necessarily very repeatable, and can vary over a narrow heat flux range. Based on this set of data, a curve was fitted to represent the effect of flow rate on the CHF for the considered conditions. The trend once more implies that increasing flow rate beyond a certain level (the medium flow rate in this case) has a minimal effect on CHF, and is consistent with observations made by earlier studies.

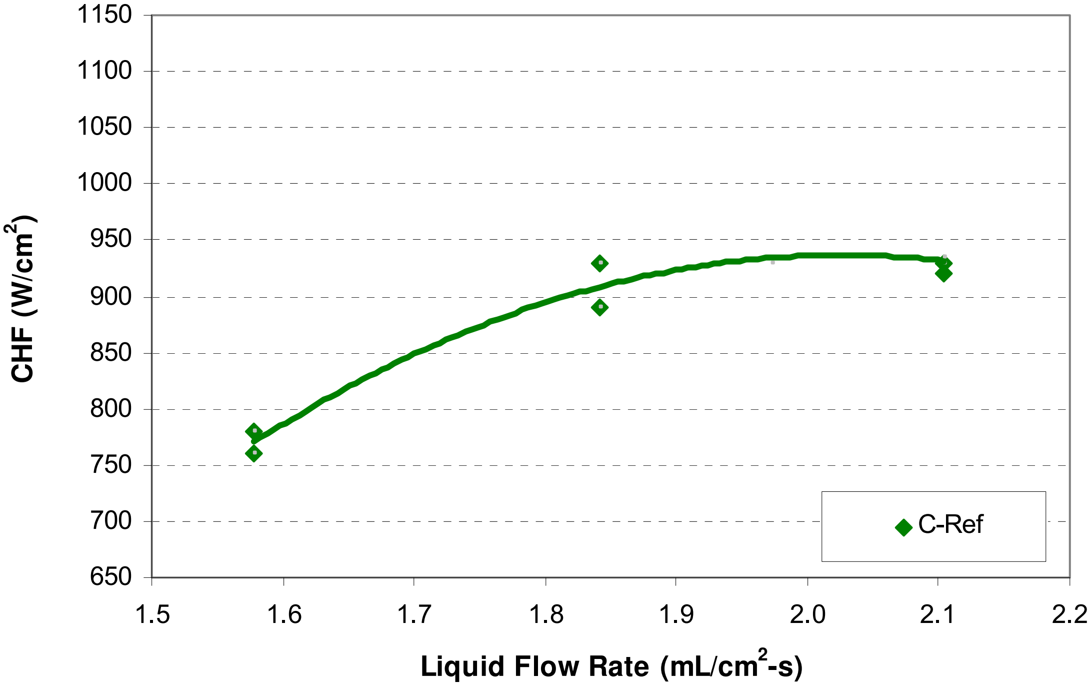

Figure 5-9: Effect of Liquid Flow Rate on CHF for the Surface ***s***

Figure 5-10 then incorporates CHF data, or highest recorded heat fluxes at heater limit otherwise, from all other tests. The curve fit for the surface ***s*** was also included here, and offset for other surfaces based on their low flow rate CHF values, assuming the same trend applies to all. When data are closely examined, this approach actually seems reasonable since heat fluxes at heater limit, for the surfaces ***Mpf-0.50*** and ***Mpf-0.50mp-c*** at high flow rate, match or exceed the estimated CHF values.

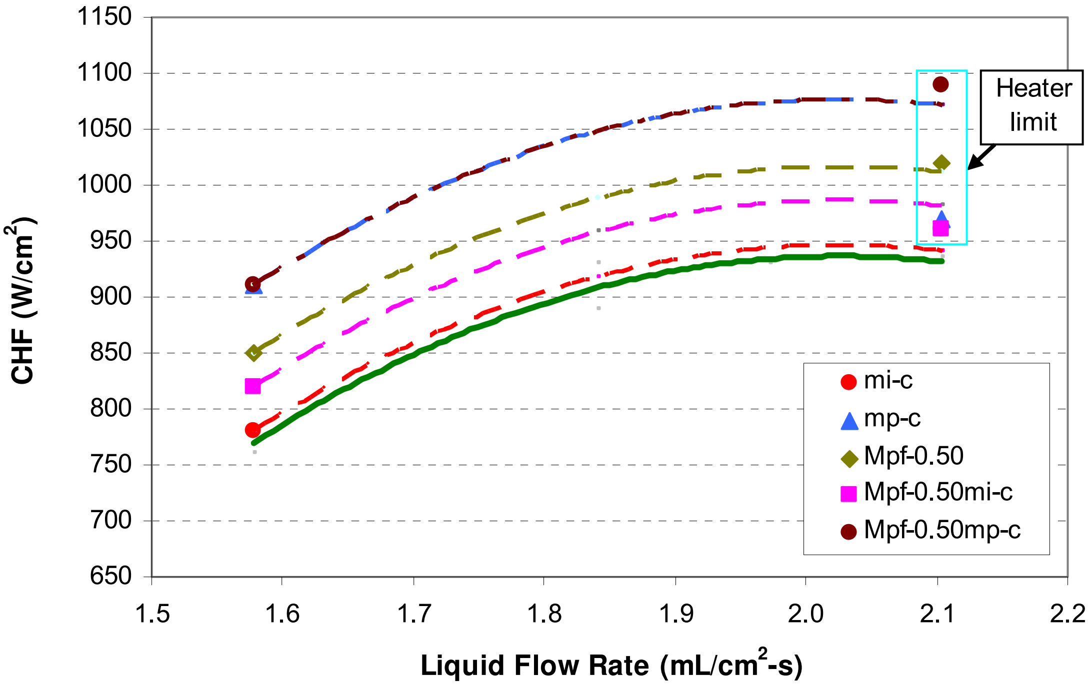

Figure 5-10: Estimated Effect of Liquid Flow Rate on CHF for All Selected Enhanced Surfaces

As mentioned before, when attempting to achieve higher CHF with higher flow rates, another performance aspect to consider is the spray cooling efficiency. Figure 5-11 illustrates efficiency as a function of liquid flow rate. Data from reference surface were again used to determine the overall trend, which indicates that when flow rate is increased from low to medium, efficiency slightly goes up (≈1%), but with further flow rate increase efficiency starts to decrease since CHF remains nearly the same.

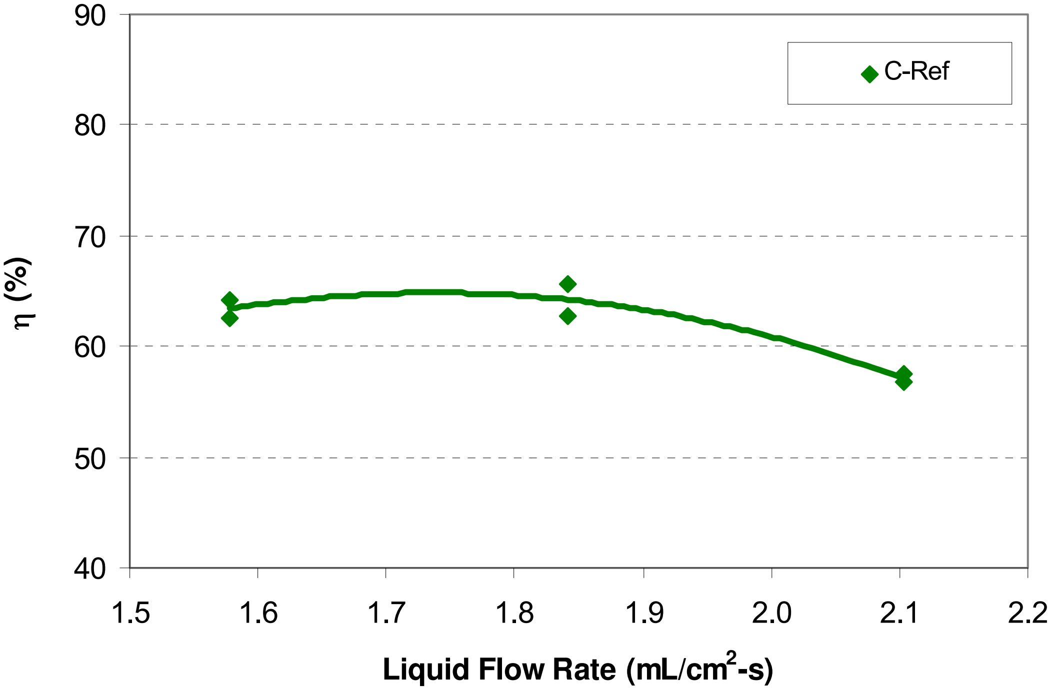

Figure 5-11: Effect of Liquid Flow Rate on Spray Cooling Efficiency for the Surface ***s***

Efficiencies from the other CHF tests are appended to Figure 5-12. Data here show that the highest efficiency reached during this study was 74.9% for both the surfaces ***mp*** and ***Mpf-0.50mp-c***.

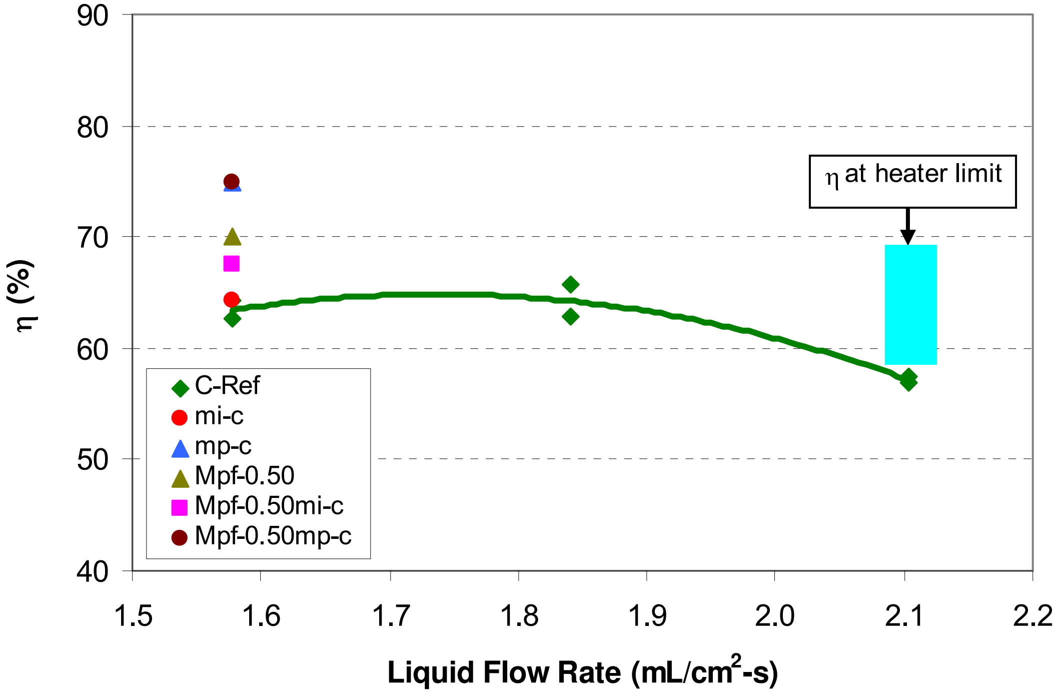

Figure 5-12: Effect of Liquid Flow Rate on Spray Cooling Efficiency for All Selected Enhanced Surfaces

# CHAPTER 6: CONCLUSIONS

This last chapter, summarizes concluding remarks, highlights important contributions, and outlines some recommendations that can be considered for future related research.

## 6.1 Concluding Remarks

The present experimental work focused on high heat flux spray cooling with ammonia, and aimed to 1) investigate the effect of surface enhancement on spray cooling performance, and 2) contribute to the current understanding of spray cooling heat transfer mechanisms. Surface modification techniques were utilized to produce micro scale indentations and protrusions, macro (mm) scale pyramidal, triangular, rectangular, and square pin fins. Another group, multi-scale structured surfaces, had combination of macro and micro scale structures.

In the first stage of the study, enhanced surfaces were investigated for the highest heat transfer coefficient at heat fluxes of up to 500 $W/cm^2$ that can comfortably accommodate most of the applications requiring high heat flux removal. Structural parameters of size and geometry were varied in an effort to find optimum surfaces. Based on the results of this stage, it was found that:

- Microstructured surfaces offered a substantial performance enhancement with heat transfer coefficients of up to 534,000 $W/m^{2o}C$ at 500 $W/cm^2$, corresponding to 81% increase over the reference smooth surface.
- The surfaces ***mi*** and ***mp*** performed nearly the same as they approach 500 $W/cm^2$ heat flux. Varying roughness levels had modest effect on both types of surfaces. For the

surface ***mi***, lower roughness levels provided better heat transfer at low heat fluxes (<400 W/cm$^2$). For the surface ***mp***, the opposite trend was observed, and higher roughness levels provided better heat transfer at low heat fluxes (<300 W/cm$^2$).

- Macrostructured surfaces also offered a performance enhancement with heat transfer coefficients of up to 426,000 W/m$^{2o}$C at 500 W/cm$^2$, corresponding to 44% increase over the reference smooth surface.
- Among the macrostructured surfaces, the surface ***Mpf*** appeared to be slightly superior. When structure size was varied, the surface ***Mpf-0.25*** with the shortest (0.25 mm) fins performed the best.
- Multi-scale structured surfaces achieved the highest performance enhancement with heat transfer coefficients of up to 772,000 W/cm$^{2o}$C at 500 W/cm$^2$, corresponding to 161% increase over the reference smooth surface.
- The surfaces ***Mpf-0.25mi*** and ***Mpf-0.25mp*** had very close performances at 500 W/cm$^2$, but the surface ***Mpf-0.25mp*** entered the two phase regime earlier, performing better at low to medium heat fluxes (<450 W/cm$^2$).
- This performance enhancement can be attributed to the increase in surface area and stronger contribution of other phase-change mechanisms beyond the free surface evaporation and secondary nucleation mechanisms of spray cooling. Both microstructured surfaces provide a spectrum of cavity sizes and thus have the potential to generate additional surface nucleation sites and increase three-phase contact line length density. Superior performance of the surface ***mp*** at low to medium heat fluxes is believed

to be due to its complex structure that offers more surface area and reentrant cavities compared to the surface ***mi***.

- Initial testing with selected microstructured surfaces also experienced hysteresis effect with lower surface superheats in the cooling-down mode at a given heat flux. Hysteresis effect was more pronounced for the surface ***mp*** indicating its dependence on surface roughness level. Two sets of experiments were performed with the surface ***mp*** in order to address whether initially observed hysteresis changes with varying heat flux conditions, and whether hysteresis relates to thermal history of the heater. Data suggested that once the three-phase contact line is established on the surface at a certain heat flux, microstructures retain vapor effectively in the cavities and help maintain contact line length so that heater can provide a consistent cooling curve and hysteresis effect at varying heat fluxes (as low as 25 W/cm$^2$ for the present study). At 0 W/cm$^2$, the heater surface loses the contact line length and restores to its initial state. Data also indicated that as heat flux and surface temperature of the heater increase, contact line length on the surface also increases proportionally. Since microstructures help sustain established contact line length, the heater surface experiences a larger hysteresis or lower superheat as it returns from a higher heat flux condition showing a direct relation between hysteresis and thermal history of the heater.

In the second stage of the study, selected enhanced surfaces were investigated for the CHF. Based on the results of this stage, it was found that:

- The surfaces ***Mpf-0.25mp-c*** and ***mp-c*** had the highest CHF value of 910 W/cm$^2$, corresponding to 18% increase over the reference smooth surface.

- When the effect of liquid flow rate was investigated, most of the heaters had resistor failures at heat fluxes >950 W/cm$^2$ before they reach to CHF. However, the effect of flow rate was still captured, and it was estimated that the surface ***Mpf-0.25mp-c*** can reach to CHF value of ≈1100 W/cm$^2$.
- Enhanced surfaces are capable of retaining more liquid compared to a smooth surface, and efficiently spread the liquid film via capillary force within the structures. This unique advantage delays the occurrence of dry patches at high heat fluxes, and leads to higher CHF.

Overall, the present study, through extensive experimental data, emphasized the importance of boiling through surface nucleation as a heat transfer mechanism that can greatly enhance spray cooling performance.

## 6.2 Recommendations for Future Work

In light of the obtained experience and the conclusions from the current study, some additional topics, that warrant further investigation with potential to provide performance benefits, can be suggested for future research in this area.

- Investigation of nanostructured surfaces would allow evaluating surface enhancements in a broader span, beyond macro and micro scales. Especially the nano scale structures designed to improve wetting characteristics might help increase heat transfer coefficient and CHF. Combination of macro, micro, and nano scale surface features would take advantage of the several heat transfer mechanisms simultaneously.

- Investigation of the effect of surface material on the heat transfer performance would be another topic of interest. Although a previous work on the effect of surface material reported only modest changes in heat transfer, the three types of heaters in this study had noticeably different performances.

# LIST OF REFERENCES

[1] Chow, L.C., Sehmbey, M.S., and Pais, M.R., 1997, "High Heat Flux Spray Cooling," Annual Review of Heat Transfer, **8**, pp. 291-318.

[2] Kim, J., 2007, "Spray Cooling Heat Transfer: The State of the Art," International Journal of Heat and Fluid Flow, **28**, pp. 753-767.

[3] Yang, J., Chow, L.C., and Pais, M.R., 1993, "Nucleate Boiling Heat Transfer in Spray Cooling," *Proceedings of the 29th ASME/AIChE National Heat Transfer Conference,* Atlanta, GA.

[4] Pautsch, A.G., and Shedd, T.A., 2006, "Adiabatic and Diabatic Measurements of the Liquid Film Thickness during Spray Cooling with FC-72," International Journal of Heat and Mass Transfer, **49**, pp. 2610-2618.

[5] Pais, M.R., Tilton, D., Chow, L.C., and Mahefkey, E.T., 1989, "High Heat Flux, Low Superheat Evaporative Spray Cooling," *Proceedings of the 27th AIAA Aerospace Sciences Meeting*, Reno, NV.

[6] Yang, J., Chow, L.C., Pais, and M.R., 1996, "Nucleate boiling heat transfer in spray cooling," ASME Journal of Heat Transfer, **118**, pp. 668–671.

[7] Rini, D.P., Chen, R.H., Chow, and L.C., 2002, "Bubble Behavior and Nucleate Boiling Heat Transfer in Saturated FC-72 Spray Cooling," ASME Journal of Heat Transfer, **124**, pp. 63–72.

[8] Horacek, B., Kiger, K., and Kim, J., 2005, "Single Nozzle Spray Cooling Heat Transfer Mechanisms," International Journal of Heat and Mass Transfer, **48**, pp. 1425-1438.

[9] Tilton, D.E., 1989, "Spray Cooling," Ph.D. Dissertation, University of Kentucky, Lexington, KY.

[10] Yang, J., 1993, "Spray Cooling with an Air Atomizing Nozzle," Ph.D. Dissertation, University of Kentucky, Lexington, KY.

[11] Sehmbey, M.S., Chow, L.C., Hahn, O.J., and Pais, M.R., 1995, "Effect of Spray Characteristics on Spray Cooling with Liquid Nitrogen," Journal of Thermophysics and Heat Transfer, **9**, pp. 757-765.

[12] Glassman, B.S., 2005, "Spray Cooling for Land, Sea, Air and Space Based Applications, a Fluid Management System for Multiple Nozzle Spray Cooling, and a Guide to High Heat Flux Heater Design," M.S. Thesis, University of Central Florida, Orlando, FL.

[13] Pais, M.R., Chow, L.C., and Mahefkey, E.T., 1992, "Surface Roughness and Its Effects on the Heat Transfer Mechanism in Spray Cooling," ASME Journal of Heat Transfer, **114**, pp. 211–219.

[14] Sehmbey, M.S., Pais, M.R., and Chow, L.C., 1992, "Effect of Surface Material Properties and Surface Characteristics in Evaporative Spray Cooling," Journal of Thermophysics and Heat Transfer, **6**, pp. 505-511.

[15] Kim, J.H., You, S.M., and Choi, U.S., 2004, "Evaporative Spray Cooling of Plain and Microporous Coated Surfaces," International Journal of Heat and Mass Transfer, **47**, pp. 3307–3315.

[16] Stodke, C., and Stephan, P., 2005, "Spray Cooling Heat Transfer on Microstructured Surfaces," *Proceedings of the 6th World Conference on Experimental Heat Transfer, Fluid Mechanics, and Thermodynamics*, Matsushima, Miyagi, Japan.

[17] Amon, C., Yao, S.C., Wu, C.F., and Hsieh, C.C., 2005, "Microelectromechanical System-Based Evaporative Thermal Management of High Heat Flux Electronics," ASME Journal of Heat Transfer, **127**, pp. 66–75.

[18] Hsieh, C.C., and Yao, S.C., 2006, "Evaporative Heat Transfer Characteristics of a Water Spray on Micro-Structured Silicon Surfaces," International Journal of Heat and Mass Transfer, **49**, pp. 962–974.

[19] Silk, E., Kim, J., and Kiger, K.T., 2006, "Enhanced Surface Spray Cooling with Embedded and Compound Extended Surface Structures," *Proceedings of the ITHERM 2006*, San Diego, CA.

[20] Coursey, J., Kim, J., and Kiger, K.T., 2006, "Spray cooling of high aspect ratio open microchannels" *Proceedings of the ITHERM 2006*, San Diego, CA.

[21] Carey, V.P., 2008, *Liquid-Vapor Phase-Change Phenomena Second Edition*, Taylor and Francis, New York.

[22] http://products3.3m.com/catalog/us/en001/oil_gas/specialty_materials.

[23] Olympus Confocal Scanning Laser Microscope LEXT OLS3100/OLS3000 User's Manual, Ver. 6.0

[24] Bhushan, B., 2002, *Introduction to Tribology*, John Wiley & Sons, New York.

[25] Driggers, R. G., 2003, *Encyclopedia of Optical Engineering*, Volume 2, CRC Press, Florida.

[26] Avdelidis, N.P., and Moropoulou, A., 2003, "Emissivity Considerations in Building Thermography," Energy and Buildings, **35**, pp. 663–667.

[27] Bergles, A.E., and Chyu, M.C., 1982, “Characteristics of Nucleate Pool Boiling from Porous Metallic Coatings,” Journal of Heat Transfer, **104**, pp. 279–285.

[28] Marto, P.J., and Lepere, V.J., 1982, “Pool Boiling Heat Transfer from Enhanced Surfaces to Dielectric Fluids,” Journal of Heat Transfer, **104**, pp. 292–299.

[29] Shi, M., Ma, J., and Wang, B., 1993, “Analysis on Hysteresis in Nucleate Pool Boiling Heat Transfer,” International Journal of Heat and Mass Transfer, **36** (18), pp. 4461-4466.

[30] Hwang, G.-S., and Kaviany, M., 2006, “Critical Heat Flux in Thin, Uniform Porous Coatings,” International Journal of Heat and Mass Transfer, **49**, pp. 844-849.

[31] Hsu, Y.Y., 1962, “On the Size Range of Active Nucleation Cavities on a Heating Surface,” Journal of Heat Transfer, **84**, pp. 207–213.

[32] Yang, J., M.S., Pais, M.R., and Chow, L.C., 1993, “Critical Heat Flux Limits in Secondary Gas Atomized Liquid Spray Cooling,” Experimental Heat Transfer, **6**, pp. 55-67.

[33] Chen, R.-H., Chow, L.C., and Navedo, J. E., 2002, “Effects of Spray Characteristics on Critical in Subcooled Water Spray Cooling,” International Journal of Heat and Mass Transfer, **45**, pp. 4033-4043.

[34] Chen, R.-H., Chow, L.C., and Navedo, J. E., 2004, “Optimal Spray Characteristics in Water Spray Cooling,” International Journal of Heat and Mass Transfer, **47**, pp. 5095-5099.